

Nanoparticle-enhanced Imaging Based Plasmonic Biosensor

Présentée le 23 octobre 2020

à la Faculté des sciences et techniques de l'ingénieur
Laboratoire de systèmes bionanophotoniques
Programme doctoral en microsystèmes et microélectronique

pour l'obtention du grade de Docteur ès Sciences

par

Alexander BELUSHKIN

Acceptée sur proposition du jury

Dr S. Carrara, président du jury
Prof. H. Altug, directrice de thèse
Dr R. Ferrini, rapporteur
Prof. J.-S. Yeo, rapporteur
Prof. D. Psaltis, rapporteur

Keeping an open mind is a virtue ...
but not so open your brains fall out.

— Carl Sagan

To my family, friends, and mentors, and those who inspired this journey

Abstract

Efficient medical care fundamentally relies on the ability to provide a timely and accurate diagnosis. Thanks to advances in biomedical research, specific molecules called diagnostic molecular biomarkers have been discovered in the human body that help indicate diseases in highly specific ways. The small size and low concentration of many of these molecules pose a serious challenge to detecting them from the rich content of human blood and other liquid biopsies. Medical laboratories use large and complex tools to enable sensitive and robust quantification of such biomarkers. However, these approaches are time-consuming, require expensive equipment and delay the doctors' decision-making. Therefore, compact, cost-effective and rapid technologies that enable testing of biological fluids to identify low-abundance biomarkers directly at the patient's bedside are critically needed to assist the modern healthcare.

This doctoral thesis presents a novel biosensor that enables highly sensitive, accurate and rapid detection of disease biomarkers in a low-cost and portable device directly from patient blood serum. The first major and original contribution is on the introduction of an innovative sensing principle that uses sub-wavelength gold nanoparticles and large area periodic gold nanohole arrays. The nanohole arrays consist of millions of nanoporations in a thin gold metal film on a glass substrate and enable a plasmonic phenomenon called extraordinary optical transmission. The interactions between nanoparticles and nanoholes are imaged in a spectrometer-free set-up and enable the detection of individual molecule binding in complex samples. Unlike conventional

plasmonic sensing approaches that rely on spectral shifts of plasmonic resonances, our method exploits intensity modulations caused by individual nanoparticles on nanohole arrays. Therefore, the technology overcomes classical plasmonic detection limits imposed by refractive index sensitivity. The work shows that the biosensor achieves highly sensitive detection, meeting clinically relevant concentrations, and can provide a powerful platform for biomarkers testing.

The second major and original contribution includes the integration of the novel plasmonic sensor technology into a portable point-of-care (POC) device. It is deployed in a hospital and validated with a wide range of patient samples with inflammatory conditions. The device enables ultra-sensitive detection of two sepsis-related biomarkers, procalcitonin, and C-reactive protein. The tests with biobank patient samples revealed that the novel POC device provides diagnostic performance equivalent to gold standard laboratory immunoassays. Moreover, identification of biomarker levels can be performed in under 15 minutes on-site, providing critical advantage compared to laboratory testing.

The results of this thesis build upon a broad interdisciplinary knowledge ranging from engineering (including plasmonics, imaging, nanofabrication, and device integration) to chemistry, biology, and medical diagnostics. The plasmonic sensing principle introduced in this work offers a promising strategy for the development of many new biosensing applications, while the developed point-of-care biosensor has the potential to provide a rapid and accurate tool to assist the diagnosis and management of diseases in various settings, improving the quality of medical care for more people.

Keywords:

biosensors, nanoplasmonics, gold nanoparticles, plasmonic nanohole arrays, plasmonic imaging, digital molecule detection, point-of-care diagnostics, sepsis

Résumé

L'efficacité des soins médicaux repose fondamentalement sur la disponibilité de diagnostics à la fois rapides et précis. Grâce aux progrès de la recherche biomédicale, certaines molécules ont été découvertes dans le corps humain qui permettent de révéler des maladies de manière très spécifique. Ces molécules, appelées biomarqueurs de diagnostic moléculaire, sont souvent de petite taille ainsi que présentent en très faible concentration dans le sang humain ou autres échantillons de liquides biologiques au contenu abondant, ce qui rend leur détection problématique. Les laboratoires médicaux utilisent des instruments volumineux et complexes afin de permettre une quantification sensible et robuste de ces biomarqueurs. Néanmoins, ces approches nécessitent un équipement coûteux et prennent un temps important, retardant ainsi de façon significative la prise de décision des médecins. Par conséquent, des technologies plus compactes, économiques et rapides permettant de tester des échantillons de liquides biologiques pour identifier des biomarqueurs de faible abondance, directement au chevet du patient, sont devenues une nécessité absolue pour améliorer les soins de santé modernes.

Cette thèse de doctorat présente un nouveau biocapteur qui permet une détection hautement sensible, précise et rapide de biomarqueurs grâce à un appareil portable et peu coûteux directement à partir du sérum sanguin du patient. La première contribution majeure et originale porte sur l'introduction d'un principe de détection innovateur qui utilise des nanoparticules d'or sub-longueur d'onde ainsi que des grandes surfaces de

réseaux de nano-trous d'or. Les réseaux de nano-trous se composent de millions de nano-perforations dans un mince film d'or sur un substrat en verre qui permettent un phénomène plasmonique appelé transmission extraordinaire optique. Les interactions entre les nanoparticules et les nano-trous sont imagées dans une configuration qui ne requiert pas de spectromètre et rendent possible la détection de molécules individuelles, capturées dans des échantillons complexes. Contrairement aux approches de détection plasmonique conventionnelles qui reposent sur les décalages spectraux des résonances plasmoniques, notre méthode exploite les modulations d'intensité causées par des nanoparticules individuelles sur des réseaux de nano-trous. Par conséquent, cette technologie dépasse les limites classiques de détection plasmonique imposées par la sensibilité à l'indice de réfraction. Le travail présenté dans cette thèse montre que ce biocapteur permet une détection hautement sensible, répondant aux concentrations d'intérêt clinique, et peut fournir une plateforme performante pour les tests de biomarqueurs.

La deuxième contribution majeure et originale de cette thèse comprend l'intégration de la nouvelle technologie de capteur plasmonique en un dispositif portable «point-of-care (POC)». Il est utilisé dans un hôpital et validé avec une gamme importante d'échantillons de patients atteints de maladies inflammatoires. Le dispositif permet la détection ultrasensible de deux biomarqueurs liés à la septicémie : la procalcitonine et la protéine C réactive. Les tests avec des échantillons de patients issus de biobanques ont révélé que le nouveau dispositif POC offre des performances de diagnostic équivalentes aux tests immunologiques de laboratoire standard. De plus, l'identification des niveaux de biomarqueurs peut être effectuée en moins de 15 minutes sur place, offrant un atout d'ordre critique par rapport aux tests de laboratoire.

Les résultats de cette thèse s'appuient sur une vaste connaissance interdisciplinaire allant de l'ingénierie (comprenant la plasmonique, l'imagerie, la nanofabrication et l'intégration de dispositifs) à la chimie, la biologie et le diagnostic médical. Le principe de détection plasmonique introduit dans cette thèse offre une stratégie prometteuse pour

le développement de nombreuses nouvelles applications de biodétection. De plus le biocapteur POC développé a le potentiel de fournir un outil rapide et précis pour aider au diagnostic et à la gestion des maladies dans divers contextes, améliorant ainsi la qualité des soins médicaux pour un plus grand nombre de personnes.

Mots-clés:

biocapteurs, nanoplasmonique, nanoparticules d'or, réseaux de nano-trous plasmoniques, imagerie plasmonique, détection numérique de molécules, diagnostic point-of-care, septicémie

Table of Contents

Chapter 1	Introduction	1
	Structure of this thesis.....	3
Chapter 2	Disease biomarkers and point-of-care testing in diagnostics.....	5
2.1.	Biomarkers as disease indicators	5
2.1.1.	Protein biomarkers.....	6
2.1.2.	DNA and RNA biomarkers	10
2.1.3.	Small molecule metabolite biomarkers	12
2.2.	Laboratory techniques for biomarkers detection	12
2.2.1.	ELISA.....	14
2.2.2.	CLIA.....	15
2.2.3.	ITA.....	16
2.3.	Point-of-care biosensors.....	18
2.3.2.	Electrochemical POC biosensors.....	19
2.3.3.	Optical POC biosensors.....	21
Chapter 3	Plasmonics for optical biosensors.....	27
3.1.	Surface Plasmon Resonance	28
3.2.	Localized surface plasmon resonance.....	32
3.3.	Plasmonic nanohole arrays	34
3.3.1.	Single aperture.....	34
3.3.2.	Periodic nanohole arrays	36
3.3.3.	Optical properties and design of nanohole arrays	38
3.4.	Nanohole array biosensors.....	46
Chapter 4	Nanoparticle enhanced plasmonic biosensor for digital biomarker detection in a microarray	51
4.1.	Abstract.....	51
	Keywords	53
4.2.	Introduction.....	53
4.3.	Results and Discussion	56
4.3.1.	Principle of detection.....	56

4.3.2.	Plasmonic imaging of Au NPs on Au-NHAs	61
4.3.3.	SEM validation of plasmonic imaging	64
4.3.4.	Sandwich assay protein detection.....	65
4.4.	Conclusions.....	69
4.5.	Materials and Methods.....	70
4.5.1.	Gold nanohole array fabrication	70
4.5.2.	Numerical simulations.....	71
4.5.3.	Optical set-up.....	71
4.5.4.	Chemicals and biologicals	71
4.5.5.	Au-NHA functionalization	72
4.5.6.	Biotin-BSA sandwich assay	73
4.5.7.	Au nanoparticle conjugation to anti-CRP antibodies	73
4.5.8.	CRP sandwich assay	73
	Acknowledgements.....	74
4.6.	Supplementary Figures	75
Chapter 5 Rapid and Digital Detection of Inflammatory Biomarkers Enabled by a Novel Portable Nanoplasmonic Imager.....		85
5.1.	Abstract.....	86
	Keywords	87
5.2.	Introduction.....	88
5.3.	Results and Discussion	91
5.3.1.	Detection mechanism	91
5.3.2.	Plasmonic microarray sensors	92
5.3.3.	Portable optical reader	94
5.3.4.	Bioassay.....	95
5.3.5.	Clinical tests of the DENIS system	98
5.3.6.	Rapid biomarker detection.....	105
5.3.7.	Discussion.....	107
5.4.	Conclusion	109
5.5.	Experimental Methods	109

5.5.1.	Au-NHA sensor fabrication:.....	109
5.5.2.	Chemicals and Biologicals:	110
5.5.3.	Au-NHA functionalization:	111
5.5.4.	Au-NP functionalization:.....	112
5.5.5.	Biobank samples:.....	112
5.5.6.	Serum bioassays:	113
5.5.7.	Calibration measurements:	114
5.5.8.	Optical reader:	115
5.5.9.	Image processing:	115
	Acknowledgments.....	116
	Author Contributions	117
5.6.	Supporting Information.....	118
Chapter 6	Conclusions and outlook	125
6.1.	Main achievements	125
6.1.1.	Nanoparticle enhanced plasmonic biosensor.....	126
6.1.2.	Rapid and digital detection of inflammatory biomarkers.....	127
6.1.3.	Scientific output.....	128
6.2.	Outlook	129
6.2.1.	Increased measurement sensitivity and reduced time-to-result with active microfluidic flow.....	130
6.2.2.	Increased measurement sensitivity and reduced time-to-result with electrohydrodynamic steering	132
6.2.3.	Technology transfer and development	133
	References.....	135

Chapter 1

Introduction

The current healthcare system is in need of transformation. The costs of medical care are rising, as it is becoming evident that the paradigm of one-fits-all treatment approaches is becoming obsolete. The pharmaceutical companies struggle to come up with new blockbuster drugs and the efficiency of commercial drug research and development has been falling. At the same time as new drugs are becoming increasingly more difficult to deliver, advances in biomedical research are uncovering vast amounts of data on biomolecular clues of diseases. Analysis of this information provides a deeper understanding of the heterogeneity in underlying conditions, enabling more specific diagnosis and identification of finer patient sub-populations. Upon the administration of a particular drug or therapy, different patients presenting similar symptoms and conditions can exhibit remarkably different responses. For the treatments to be most effective, they will need to be personalized for different individuals.

The term “personalized medicine”, defined by the US Council of Advisors on Science and Technology, introduced the concept of tailored medical treatment to the patient’s characteristics by providing “the right drug, for the right patient, at the right time.” Treatment approaches driven by data will be key to provide patient-focused therapies that are most efficient for particular individual conditions. Such approaches will rely on the availability and analysis of patients’ diagnostic information on-site where and when it is needed. Therefore, accessible diagnostic testing will be essential in the emergence of personalized medicine.

The current medical diagnostics relies on laboratory-based tools that are bulky, expensive and require long time and trained medical staff to operate. In traditional laboratory testing, when a doctor decides that the patient needs to take a diagnostic test, their sample first needs to be taken and transported to a centralized laboratory. After the sample processing and data analysis, the results can be returned to the physician. In this way, the ultimate patient diagnosis and treatment prescription can only take place at the second medical appointment. Such approach costs time, money, and leads to poor treatment outcomes due to delayed treatment. This ultimately makes laboratory-based testing unsuitable for personalized medicine. Moreover, multiple widespread medical conditions such as acute inflammation, sepsis, cardiac attack, and stroke progress so rapidly that every hour in treatment delay drastically increases mortality rates. The management of such rapidly progressing conditions is fundamentally incompatible with time-consuming laboratory tests, and urgently needs novel tools to enable rapid diagnosis directly at the patient's bedside.

In contrast to laboratory analysis, point of care testing (POC) transfers diagnostic tools from the medical laboratory directly to patients and physicians. In recent years, plasmonic biosensors have emerged as prominent candidates for the development of POC devices thanks to excellent detection performance and advances in scalable and cost-effective nanofabrication technologies. However, the sensitivity of plasmonic sensors has been achieved at the cost of complex and expensive optical readout schemes. So far, studies that address miniaturization potential of plasmonic biosensors by integrating them in compact optical set-ups have significantly sacrificed detection performance, ultimately failing to meet clinically relevant sensitivity levels from complex biological samples. This thesis presents a novel plasmonic biosensor technology that can overcome the above limitations by combining ultra-sensitive and specific plasmonic sensing technology with a compact and robust optical reader. A nanoplasmonic sensing technique based on gold nanohole arrays and gold nanoparticles was developed and numerically characterized. Based on the newly introduced

technique, a rapid and portable test for sepsis biomarkers detection was implemented. The point-of-care plasmonic device was deployed in a hospital for validation with patient samples and showed performance equivalent to gold-standard laboratory assays.

Structure of this thesis

The structure of this thesis is summarized below.

- Chapter 2 introduces the concept and different types of biomarkers, and biodetection in current diagnostics. Conventional laboratory methods are described, and a brief overview of existing point-of-care tools is given.
- Chapter 3 introduces the detection principles behind plasmonic biosensors, with a specific focus on the performance and design of gold nanohole arrays.
- Chapter 4 presents the first major result of this thesis which is on the development and engineering of the nanoparticle enhanced gold nanohole array biosensor for biomarkers detection in complex media. The mechanism of nanoparticle interaction with nanohole arrays is analyzed numerically and characterized experimentally. We demonstrate highly sensitive and specific proteins detection in a fully imaging setting without a spectrometer requirement.
- Chapter 5 presents the second major result of this thesis. The plasmonic technology developed in chapter 4 is used to introduce a novel point-of-care device to assist sepsis diagnosis in clinical settings. Bioassay is developed to measure two sepsis biomarkers from patient blood serum, and a portable reader is designed and built. The point-of-care test is deployed in a hospital, and its performance is benchmarked to gold-standard laboratory immunoassays.
- Chapter 6 summarizes the results and briefly discusses outlook and future developments of this work.

Chapter 2

Disease biomarkers and point-of-care testing in diagnostics

Correct and timely treatment of diseases is fundamental to improve the quality of medical care and increase the patient's well-being. Diagnostic testing is key to correctly identify and properly treat a disease or infectious process on time and to monitor the patient condition and response to a treatment or therapy. Currently around 70% of all medical decisions are made relying on data from diagnostic testing [1].

In this chapter, the basics of biomarkers, their types and significance are briefly described. The background of biomarkers detection in current diagnostics is discussed. Classical laboratory methods used in current practices for biomarkers detection are introduced, and a brief overview of existing point-of-care tools is given.

2.1. Biomarkers as disease indicators

Biomarkers are key elements that help diagnosis and monitoring of patients during their treatment. According to the US Food and Drug Administration (FDA), “a biomarker is a defined characteristic that is measured as an indicator of normal biological processes, pathogenic processes, or responses to an exposure or intervention, including therapeutic interventions” [2]. Any measurable biological indicator can be a biomarker. Even simple physiological parameters such as body temperature and blood pressure, can serve as biomarkers that help diagnose diseases like cold and flu or hypertension. However, such generic parameters have limited specificity and provide little insight into the

underlying biological processes within the body. Other types of biomarkers are histological or radiographic tests. Histological biomarkers are biomolecular alterations in tissues, fluids, or cells that can be assessed to indicate abnormal biological processes due to diseases, or infections, or response to therapeutic treatment [2], [3]. Radiographic biomarkers are image features on X-rays of patient's organs that provide insights about the condition of patient's organs [4], [5]. Radiographic biomarkers are frequently used to diagnose such diseases as lung cancer and arthritis. With the advances in biomedical research, new classes of biomarkers have been discovered, called molecular biomarkers that allow to assess the patients' medical condition with more precision and specificity [6]. Molecular biomarkers can be proteins, nucleic acids (DNA or RNA), or small molecule metabolites, and can be present in the blood, urine, saliva, sweat, or cerebrospinal fluid. Diagnostic tests that measure levels of these molecules help to clarify and support the clinical decisions by doctors. Over the recent years, diagnostic processes have become more strongly driven by the need to pre-select patients based on their clinical status. Particularly, next-generation healthcare is developing towards personalized treatments, which rely on rapid access to detailed information about patient health status. For example, the management of rapidly progressing diseases, such as inflammation and sepsis, is critically dependent on quick diagnosis, because early treatment is key to improve survival. On the other hand, the treatment of complex chronic conditions, such as cancer, requires frequent blood tests, screening a large variety of biomarkers to tailor the most appropriate therapy and control disease progression. The levels of molecular biomarkers provide doctors with actionable information, enabling evidence-based selection of the most appropriate treatments and drugs.

2.1.1. Protein biomarkers

Protein biomarkers are protein molecules found in the rich content of blood serum that are associated with certain diseases. Proteins are a large class of macromolecule that

consist of chains of amino acid residues connected by peptide bonds. Each protein may be composed of one or multiple amino acid chains. Humans, as well as all other eukaryotic organisms, have 21 proteinogenic amino acids, of which proteins are built [7].

Table 2.1 Conventions of common amino acids found in proteins

Amino acid	Abbreviation/ symbol	Amino acid	Abbreviation/ symbol	Amino acid	Abbreviation/ symbol
Nonpolar, aliphatic R groups		Aromatic R groups		Negatively charged R groups	
Glycine	Gly, G	Phenylalanine	Phe, F	Aspartate	Asp, D
Alanine	Ala, A	Tyrosine	Tyr, Y	Glutamate	Glu, E
Proline	Pro, P	Tryptophan	Trp, W	Polar, uncharged R groups	
Valine	Val, V	Positively charged R groups		Serine	Ser, S
Leucine	Leu, L	Lysine	Lys, K	Threonine	Thr, T
Isoleucine	Ile, I	Histidine	His, H	Cysteine	Cys, C
Methionine	Met, M	Arginine	Arg, R	Asparagine	Asn, N
				Glutamine	Gln, Q

However, the number of different protein molecules is estimated to be over 20'000 [8], [9]. This diversity of proteins can be explained not only due to combinations of amino acid sequences, but also thanks to four distinct levels of structural arrangements of protein chains (Figure 2.1).

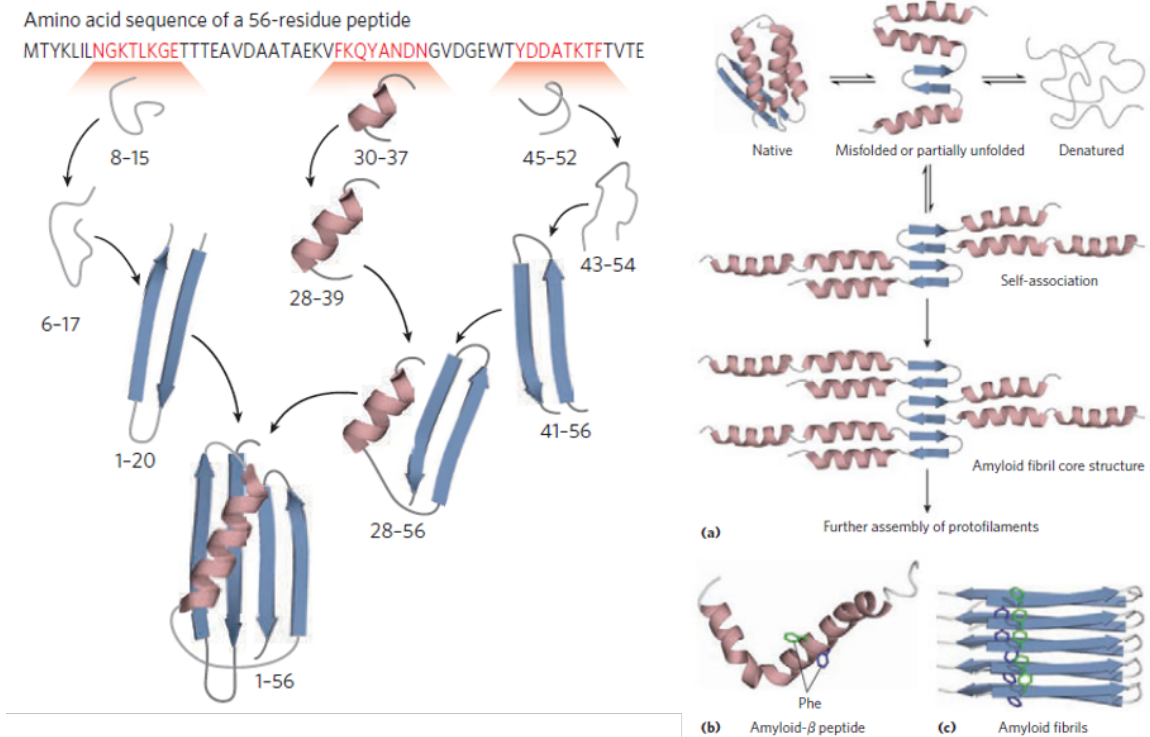


Figure 2.1 Four different levels of protein structure. Image adapted from [7].

The primary structure of proteins is their amino acid sequence; the secondary structure is the interactions between the amino acids that can form alpha-helices, beta-sheets, or unstructured loops; the tertiary structure is the arrangement of secondary structure elements in 3-dimensional space; finally, quaternary structure is the arrangement of protein units into a molecular complex.

Significant scientific effort has been made to identify protein biomarkers of clinical utility that can help predict and provide disease prognosis [10]–[14]. A number of protein biomarkers based on liquid biopsy have been approved by FDA for clinical use, such as prostate-specific antigen (PSA) for prostate cancer, CA125 (also known as mucin 16) for ovarian cancer, CA19-9 for pancreatic cancer [15], [16], procalcitonin (PCT) for sepsis [17], troponin for cardiac attack [18], and lipoprotein-associated

phospholipase A2 in stroke [19], [20]. Some representative protein biomarkers are summarized in Table 2.2.

Table 2.2 Representative protein biomarkers, their corresponding cut-off concentrations and associated diseases

Biomarker	Molecular mass	Healthy cut-off levels	Associated disease
Alfa-fetoprotein [21]	68 kDa	< 10 ng/ml	Gastrointestinal cancer
Carcinoembryonic antigen CEA [22]	150-200 kDa	<0.5 ng/ml	Liver cancer
CA-125 [23]	49 - 1500 kD	<46 U/ml	Ovarian cancer
HER2 [24, p. 2]	50-100 kDa	<10-50 ng/ml	Breast cancer
Prostate specific antigen PSA [6]	28 kDa	<2 ng/ml	Prostatic cancer
Thyroglobulin [25]	300 kDa	<30ng/ml	Thyroid cancer
Lipocalin-2 [26]	24 kDa	20-200 ng/ml	Liver cancer
Des-gamma-carboxy prothrombin [27]	70 kDa	<7.5 ng/ml	Liver cancer
Serum amyloid A [28]	13 kDa	34 ng/ml	Breast cancer
Glypican-3 [29]	65 kDa	100 ng/ml	Liver cancer
Beta-2 microglobulin [30, p. 2]	13 kDa	< 2 µg/ml	Colorectal cancer
Chromogranin A [31]	48-60 kDa	< 93 ng/ml	Pancreatic cancer
PTX3 [32]	41 kDa	< 2 ng/ml	Sepsis
Procalcitonin [17]	13 kDa	< 100 pg/ml	Sepsis and SIRS
C-reactive protein [33]	25 kDa	< 1 µg/ml	Inflammation and Sepsis

Cardiac Troponin I and Cardiac Troponin T	1-20 pg/ml	Acute myocardial infarction
--	------------	--------------------------------

2.1.2. DNA and RNA biomarkers

Nucleic acids such as DNA and RNA are the most fundamental molecules of life that encode genetic information of all living organisms. In eukaryotic cells, DNA is contained within the cell nucleus and mitochondria (and plastids DNA in plants). Although there are only 4 ribonucleic acids, Adenine, Cytosine, Guanine, and Thymine (or Uracil in RNA), human DNA encodes between 20'000 and 100'000 genes [34], [35]. The nuclear genome consists of 24 linear DNA molecules, called chromosomes, that are arranged in a tightly packed structure [36]. In fact, if stretched each human cell's DNA would be between 2 and 3 meters in length.

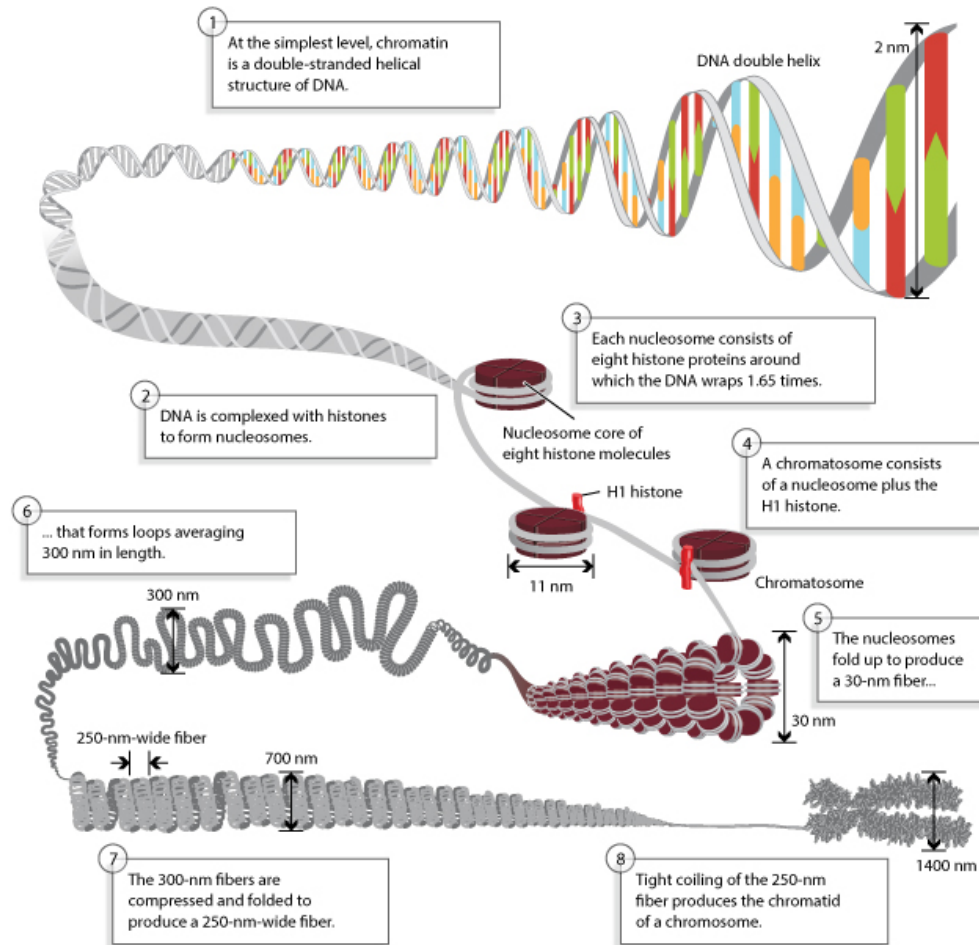


Figure 2.2 DNA arrangement in human chromosomes. Image reproduced from [37].

Normally, only very small numbers of cell-free circulating DNA (cfDNA) can be found in the blood. However, in the occurrence of cancers excessive amounts of DNA may get released into the bloodstream, and therefore can serve as markers of tumor presence [38], [39]. Moreover, by analyzing the sequence and properties of cfDNA, researchers were able to identify alterations such as mutations, methylation, changes in DNA integrity, and viral DNA that can provide important clues about the underlying disease [40]. For example, methylated septin 9 (SEPT9) DNA biomarker has received FDA approval for clinical screening of colorectal cancer [41].

2.1.3. Small molecule metabolite biomarkers

Metabolites are intermediate or end products of metabolism in the human body. The term metabolite is typically used to indicate only small molecules [42]. When diseases cause pathological conditions, this leads to alterations in the metabolic processes of many organs and tissues. Because metabolites are products of human metabolism, these alterations can be detected as changes of small molecule metabolite levels in the blood. The development of metabolomics has shed light on the role of these alterations and enabled large-scale systematic analyses of wide metabolite ranges in multiple samples. Researchers and doctors can use the measurements of metabolites changes for quantitative and dynamic tracking of organism response to external pathological agents, disease progression, or therapy effects [43]–[46]. Some of the metabolic biomarkers are serum lactate levels in sepsis [47], panels of amino acids in cancer [48], [49], derivatives of estrogen hormone in osteoporosis [50], and nitric oxide in heart failure [51].

2.2. Laboratory techniques for biomarkers detection

Technologies that enable testing of biological fluids and tissues to identify low-abundance biomarkers are a critical tool in the instrumentation of modern healthcare. These tests can help not only to mark the onset of many pathologies, but track patient progression during treatment. In fact, many early-stage biomarkers provide the only effective way to detect the onset of certain diseases to allow proper intervention and care [52]. Therefore, the development of technologies for sensitive, rapid and affordable testing enabling early diagnosis is critical to reduce mortality and healthcare cost.

In general, the detection and quantification of biomarkers can be performed using a variety of analytical assays that exploit different underlying biochemical mechanisms. The detection of DNA and RNA is classically carried out with polymerase chain reaction (PCR), quantitative PCR (Q-PCR), or a variation of one of these techniques.

PCR-based tools have been widely established in the scientific and engineering community, because they provide some of the highest levels of sensitivity and specificity close to single-molecule detection [53]. The detection of small-molecule metabolites is generally more challenging, as the differentiation between small molecules in complex samples often requires large laboratory tools like mass-spectrometry that can be difficult to scale down. Although the testing for some small molecule metabolites such as glucose can be efficiently achieved in a cost-effective sensitive way thanks to exploitation of natural enzymatic reactions, such enzymes are not readily available for the wide spectrum of metabolites.

Over the past decades of research in the biomedical field scientists identified some of the most significant biomarker signatures of clinical utility among blood-circulating proteins. This could be addressed to the vast diversity of proteins in blood serum that carries massive amounts of potentially diagnostic information. Moreover, the rise of affinity proteomics has enabled accurate approaches to decipher this information. Protein detection and analysis can be done using various analytical biochemistry assays based on different mechanisms. Among the simplest methods of protein quantification are protein-dye binding approaches. For example, Lowry protein assay [54], protein-copper chelation chemistry (biuret/BCA), and Coomassie/Bradford assay [55] are widely applied for total protein quantification in a sample. However, more complex bioanalytical applications require methods that distinguish between specific protein species. For this reason, techniques based on immunochemistry are used to enable selective and sensitive detection of different protein molecules.

The quantification of protein biomarkers is an integral part not only in the medical practice, but also in research laboratories. Techniques based on immunoassays have become a standard applied in analytical proteomics, such as enzyme-linked immunosorbent assay, or ELISA. Over the years, immunoassay technology has undergone important and radical changes thanks to continuous scientific development.

These advanced have been fueled by increased demand for sensitive and massively parallelized analysis of modern laboratory diagnostics.

2.2.1. ELISA

ELISA has become a gold-standard laboratory assay to quantify soluble proteins of interest in research and diagnostic laboratories. ELISA is a spectrophotometric technique that relies on signal transduction through measurements of light absorption by solute analyte in the sample at specific wavelengths. ELISA was first introduced by Engvall and Perlmann when they demonstrated its remarkable sensitivity and wide dynamic range in the lab on rabbit antibody quantification and in-field applications involving parasitic diseases [56]. The immunoassay is typically employed in a solid-phase setting (Figure 2.3), where the analytes are first adsorbed on an inert microtiter plate in a non-covalent way [57]. Alternatively, a layer of capture antibodies can be first immobilized on the plate in sandwiched ELISA [57]. At the next step, primary detection antibodies specific against the antigen are applied. Antibodies labeled with enzymes, such as alkaline phosphatase, are subsequently applied over the primary antibodies bound on the targets. Finally, by adding substrates for the enzymes that are now immobilized in the surface, a detectable signal is generated, which is commonly a color change of the liquid solution. The concentration of the target analytes is determined by measuring the absorbance of the colored solution and mapping it to a known value of calibration standard. Using such colorimetric signal amplification mechanism of enzymatic catalysis, the concentration of target molecules can be precisely quantified with sensitivity levels of few picograms per milliliter.

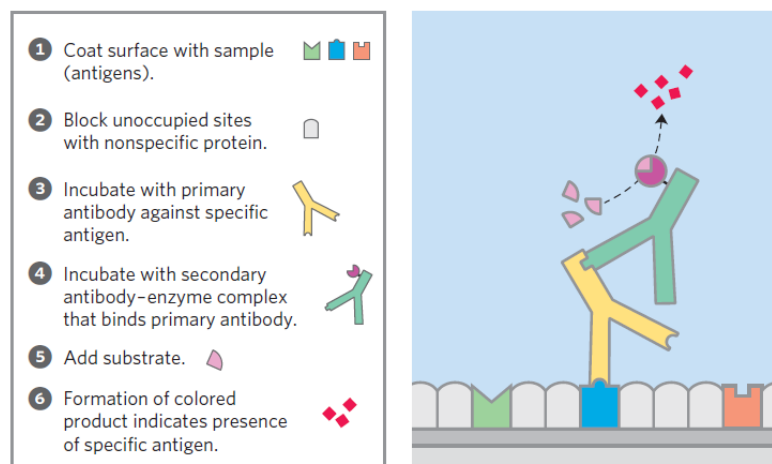


Figure 2.3 General principle of ELISA. Image reproduced from [7].

2.2.2. CLIA

Chemiluminescent immunoassay, or CLIA, is an immunoassay principle where the label is a luminescent molecule [58]. The label serves as the true “indicator” of the analytic reaction. Luminescence is the emission of light by molecules in the visible or near-infrared spectrum ($\lambda = 300\text{--}800\text{ nm}$). The light is generated in luminescent molecules when an electron transitions from an excited state to the ground state (Figure 2.4).

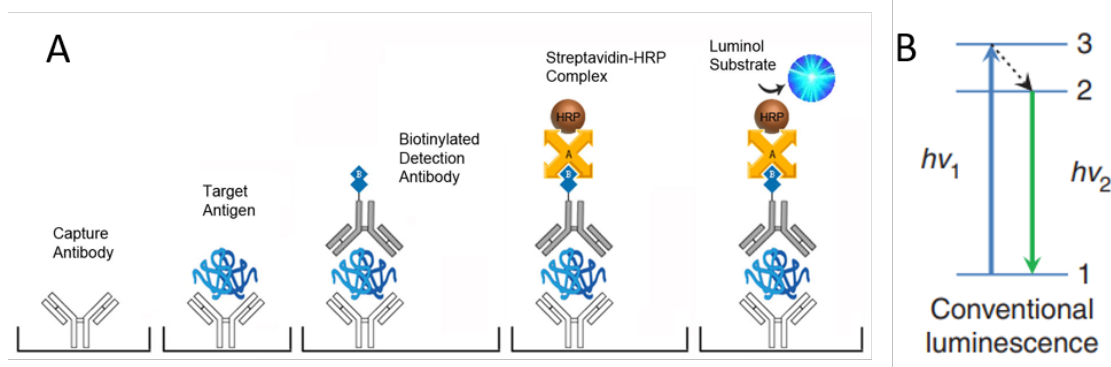


Figure 2.4 Schematic illustration of indirect CLIA employing horse radish peroxidase enzyme (HRP) (A, image reproduced from [59]) and luminescence process (B, image reproduced from [60]).

As a result, the potential energy of the electron gets released in the form of light. Unlike absorbance, which is a relative measure, luminescence can be measured in absolute values. CLIA can be direct, when luminophore marker molecules are used, or indirect - using enzyme markers for signal amplification similar to ELISA. CLIA offers a very wide dynamic range (greater than that of ELISA), and highly sensitive and specific quantification. Moreover, CLIA assays have been developed to provide high degrees of automation. Currently, CLIA technology is one of the most advanced in the clinical laboratory, offering reduced turnaround times, and the ability to run large numbers of multi-analyte test panels.

2.2.3. ITA

Immunoturbidimetric assays (ITA) are based on the measurements of micro-sized particle aggregation in solutions through light scattering [61]. In a classical case, latex particles are coated with antibodies specific to the analyte of interest. When added to the sample in the presence of the analyte, the particles form immune complexes through antibodies binding. The resulting aggregation of particles leads to an increase in the light scattering of the sample, which is proportional to the analyte concentration. The

measurements of light scattered at a specific wavelength are performed to quantify sample turbidity. The analyte concentration is then determined by benchmarking turbidity values against calibration dilutions of the analyte of known concentration.

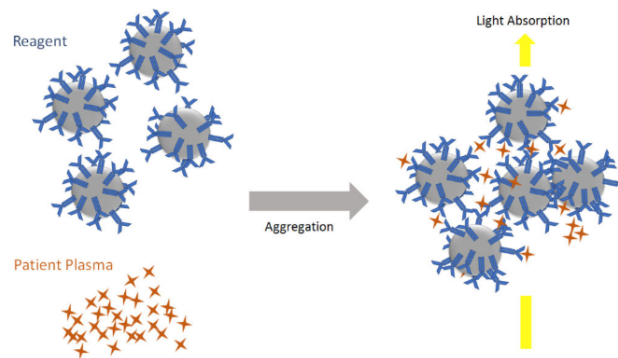


Figure 2.5 Schematic illustration of immunoturbidimetric assay principle. Image reproduced from [62].

Although ITA dynamic range is relatively narrow, a set of assays with varying particle concentrations can be obtained to cover different linear ranges. ITA assays are generally less sensitive than ELISA and CLIA and are used for quantification of proteins that are present in blood in higher concentrations in the range of micrograms per milliliter.

Overall, laboratory-based techniques are time consuming and require large well-equipped laboratories to perform the analysis. They delay the doctors' decision-making, and in practice require multiple hospital appointments for the patients, resulting in lengthy and complex data exchange between diagnostic laboratories and physicians. This costs a lot of time, money and ultimately patient well-being. Therefore, there is an urgent need for cost-efficient biosensor platforms, which can screen biomarkers in a rapid and cost-effective way directly where and when it's needed.

2.3. Point-of-care biosensors

In traditional clinical practice medical diagnostic tests have been dependent on large, complex tools and sophisticated technologies, which only trained professionals in clinical laboratories were able to operate. Point of care testing (POCT) transfers diagnostic tools from a medical laboratory directly to patients and physicians. Multiple efforts in recent scientific and engineering research have been focused on expanding point-of-care diagnostic toolbox. These devices can be miniaturized to be portable and designed to enable the deployment at the point of need and operation by semi-trained users. Point-of-care devices hold significant potential for providing affordable health monitoring in real-time and remote settings. The central components of point-of-care devices are biosensors, which deliver the analytical performance of an assay. According to the International Union of Pure and Applied Chemistry (IUPAC), a biosensor is a chemical sensor composed of a chemical recognition system (receptor) and a physicochemical transducer, in which the recognition system is based on a biochemical mechanism [63]. There are three fundamental components of a biosensor: the biorecognition element, the signal transduction mechanism, and the signal recording and processing element. The biological recognition system typically contains enzymes, antibodies or nucleic acids that specifically interact with the target analyte and ensure the selectivity of the assay. The transducer element detects the interaction, which is then converted into a digital signal.

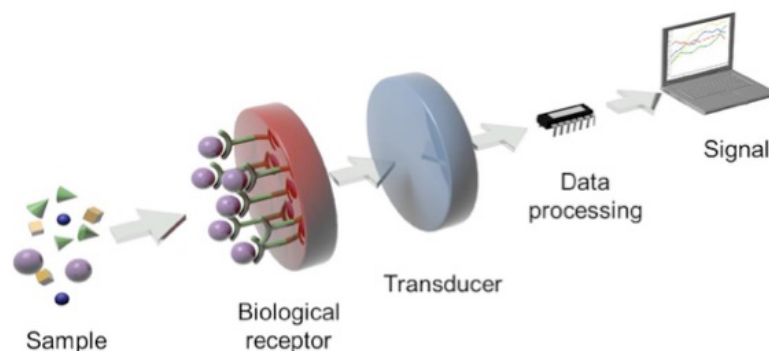


Figure 2.6 Schematic of a biosensor. Three main elements are bioreceptor layer, physicochemical transducer element, and signal readout.

A range of biosensor technologies have been explored and successfully applied for point-of-care applications necessary to advance the field of personalized health care. Particularly, recent developments in nanotechnology have provided improved tools with exceptional sensitivities and specificities to assist the assessment of the disease onset and progression. Generally, biosensors can be broadly categorized into three main classes, based on the signal transduction method: electrochemical, mechanical, and optical biosensors. Most point-of-care technologies that have found commercialized applications are based on electrochemical and optical biosensors.

2.3.2. Electrochemical POC biosensors

The electrochemical read-out principle is based on the transduction of biochemical binding events into an electrical signal. Depending on the electrical signal transduction mode, five electrochemical biosensing principles can be distinguished: amperometric/voltammetric biosensors, impedance biosensors, potentiometric biosensors, field-effect transistor (FET) biosensors, and conductometric biosensors [63], [64]. In fact, electrochemical biosensors may be some of the most prominent and widespread POC sensors [65]. They are exceptionally useful for delivering biosensing information in a fast, simple, and low-cost way in POC analyzer settings [66], [67]. A

well-known electrochemical sensor is the glucose strip test [68]. It is based on screen-printed amperometric enzyme electrodes, and enables affordable testing of blood glucose, immediately providing patients with actionable information. The glucose in a sample drop of blood is oxidized by the immobilized enzyme, and this reaction is read out as changes of redox current on the electrodes (Figure 2.7). This user-friendly technology has revolutionized the field of diabetes management through self-testing since its launch in the 1970s. Currently, glucose strips dominate the 5 billion dollars per year diabetes monitoring market [69].

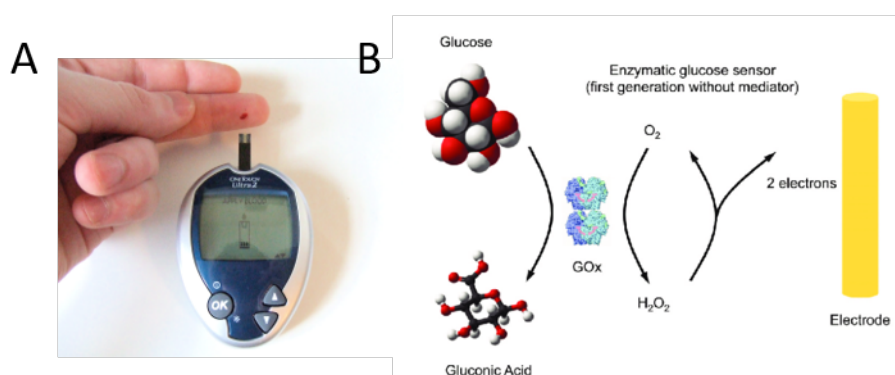


Figure 2.7 A. POC glucose test strip test. B. Principle behind electrochemical glucose sensor. Image reproduced from [70].

Among other promising electrochemical sensors are amperometric and potentiometric biosensors, such as i-STAT hand-held device, used for POC measurements of a range of electrolytes and metabolites in emergency settings [71]. However, the widespread use of many electrochemical biosensors is limited due to the nature of the detection mechanism, which is non-specifically sensitive to any alteration of the electrochemical properties in the test sample. Changes in temperature, ionic strength or pH values can lead to signal fluctuations, which limits the applicability of the assays [72].

2.3.3. Optical POC biosensors

Optical biosensors enable the detection of target analyte binding events by transducing the signal as changes in intensity, spectrum, or phase of transmitted or reflected light. These transduction principles can exploit a range of optical phenomena, from simple light scattering (turbidimetric) or color change (colorimetric) of the optical sample to fluorescence (fluorimetric), luminescence, photonic and plasmonic effects, that enable highly sensitive detection of biomolecules, ultimately down to single-molecule resolution.

Lateral flow assays

Among the rapidly growing number of strategies for qualitative and quantitative analysis using optical biosensors, lateral flow assay (LFA) based POC devices have achieved outstanding popularity thanks to the simplicity of use, long-term storage stability under various ambient conditions, rapid time-to-result and very low per-test costs [73], [74]. LFAs are frequently based on nitrocellulose paper strip, to which a sample is applied (Figure 2.8). Moreover, the tests are divided into test and control lines, allowing for quality assurance of each device. The assay detection reagents such as antibodies labeled with nanoparticles or fluorophores are pre-immobilized at different parts of the strip. When a sample is added, they become active and bind to the target biomolecules, producing color change or fluorescent signal at specific strip areas. The signal detection can be performed visually or using an optical reader.

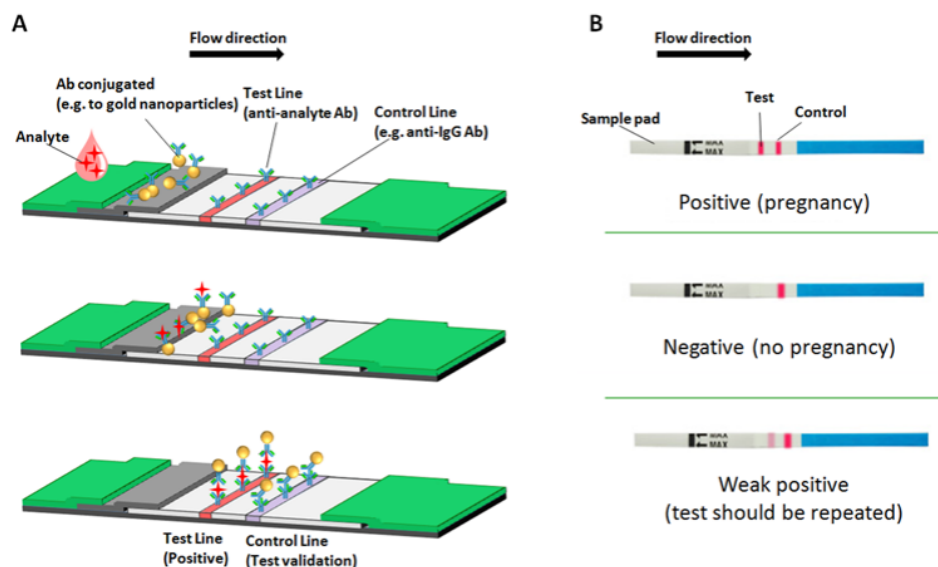


Figure 2.8 Schematic illustration of lateral flow assay operation principle (A) and image of pregnancy test lateral flow assay (B). Image reproduced from [74].

The use of simple paper strips allows immediate filtration of the sample to remove cells and large particles that can contaminate the test and obscure read-out. LFAs enable straightforward testing of whole blood, urine or saliva without sample preparation, achieving sensitivity levels from hundreds of pg/ml to 1 ng/ml and wide dynamic range [75]. Biosensors based on LFAs have found applications in a number of diagnostic and screening areas, among which are at-home pregnancy testing [76], diabetes testing [77], and POC detection of sexually transmitted diseases such as HIV [78], [79] and syphilis [80]. Despite their popularity, most LFAs provide limited sensitivity and only a qualitative assessment of the acquired optical data, where the reading of the test line is interpreted either as “not visible” or “visible”. Some LFAs have been developed in conjunction with detectors that can estimate the analyte content based on the line intensity and give a semi-quantitative output of the measurements [76]. Moreover, efforts to enhance the performance of LFAs with nanotechnology have been made. For example, a fluorescent LFA was reported by Liang et al. for the multiplexed screening of cancer cells [81]. The device used graphene oxide and quantum dots to enhance its

analytical performance and employed aptamers as molecular recognition elements. Aptamers are specifically designed small DNA fragments that can recognize biomolecules with high affinity and are more stable in long-term storage compared to antibodies. However, despite the technological advances to improve the performance of LFAs, this biosensing approach provides only qualitative or semi-quantitative information and does not meet the sensitivity requirements of many bioanalytical applications. Therefore, LFAs found limited utility among highly demanding biosensing application that require high sensitivity and precise analyte quantification.

Centrifugal microfluidic disk

Another type of point-of-care devices is based on centrifugal microfluidic technologies, which handle liquid samples by spinning a microfluidic disk. The sample is passed through a system of microfluidic channels and passive valves, by applying precisely controlled centrifugal forces with a spinning mechanism, similar to a CD drive. These compact devices enable complex liquid handling operations such as mixing of the sample with pre-loaded reagents, timing control of biochemical reactions, and separation of cells from whole blood (Figure 2.9) [82], [83]. The optical read-out is typically performed using fluorescence or absorbance measurement.

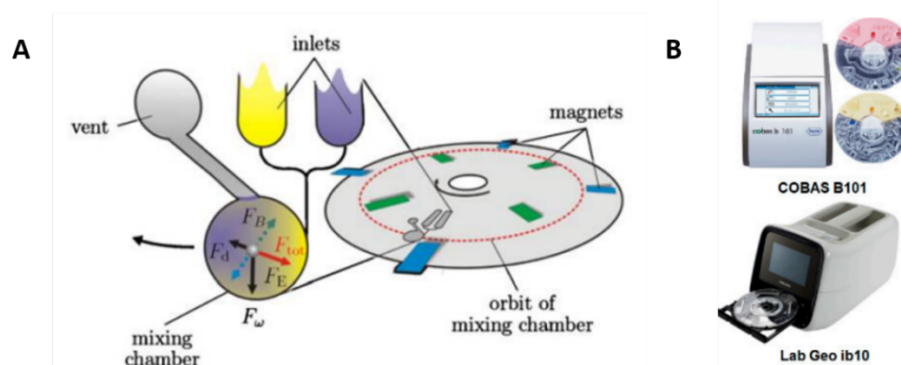


Figure 2.9 A. Illustration of spinning microfluidic disk principle. Image reproduced from [83]. B. Images of two commercial POC diagnostic devices based on spinning microfluidic disk. Image reproduced from [84].

However, although centrifugal microfluidic technologies can improve the sensitivity and enable quantitative analysis with fluorescent read-out schemes, the micro- and nano-sized channels are prone to clogging. Moreover, these devices involve mechanically moving parts that can compromise measurements robustness over time.

Nanophotonic biosensors

Recent efforts in scientific and engineering research have been focused on the advancements of novel optical biosensing technologies to overcome the limitations of existing point-of-care tools. In particular, photonic and plasmonic devices have been promising candidates for the development of next-generation highly-sensitive point-of-care biosensors [85], [86]. These devices use highly localized field enhancement generated by light at nanostructured surfaces to detect minute analyte concentrations. Highly efficient field enhancement has been achieved with photonic waveguides [87], photonic crystals [88], [89], and metal nanostructures [90]. The local change of optical properties upon the binding of biomolecules on the sensor alters the evanescent electromagnetic resonances, which can be measured in the far-field spectrum. Some of the example biosensors have been developed based on photonic waveguides [91],

whispering gallery mode resonators [92], metallic metasurfaces [93], nanoparticles [94], [95], nanostructure-nanoparticle hybrid arrays [96], or recently demonstrated dielectric metasurfaces [97].

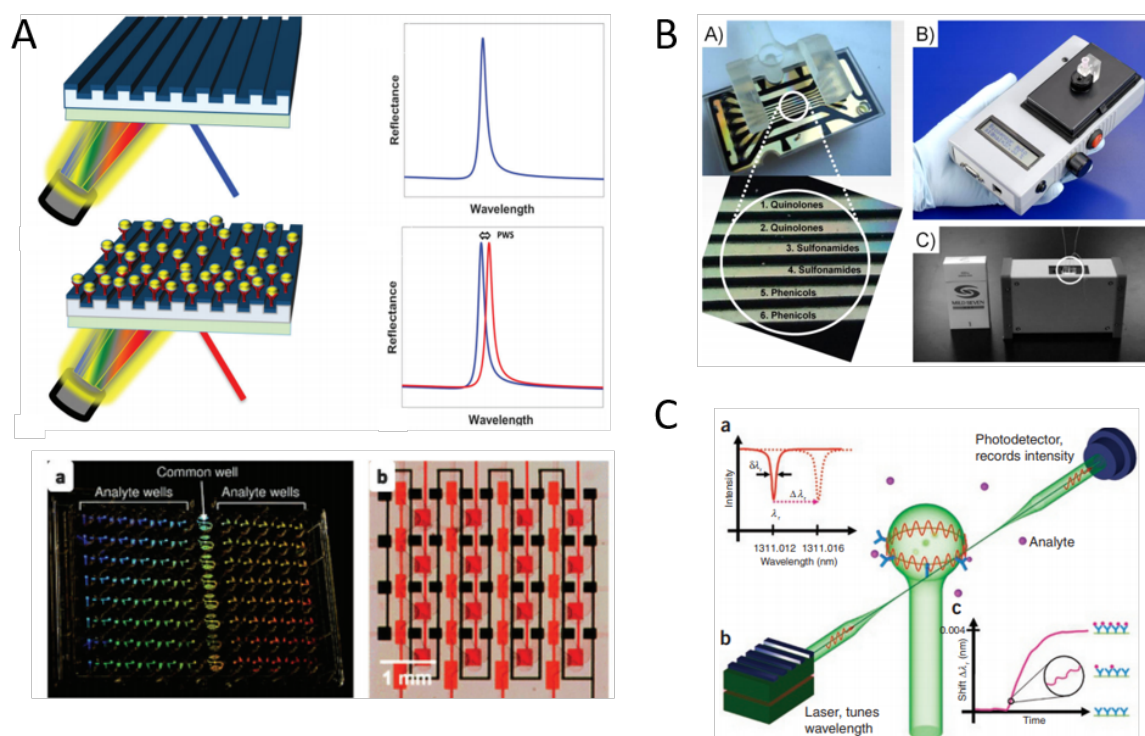


Figure 2.10 A. Schematic of mechanism of photonic crystal based biosensing and an integrated photonic crystal biosensor in a microwell plate configuration. Image adapted from [98]. B. Point-of-care surface plasmon resonance based biosensing platforms. Image reproduced from [86]. C. Illustration of whispering gallery mode biosensing principle. Image reproduced from [92].

Chapter 3

Plasmonics for optical biosensors

The field of plasmonics focuses on the study and engineering of the interactions between metals and electromagnetic radiation, such as light. These interactions give rise to surface plasmons (SPs), which are collective oscillation modes of the conduction electrons in the metal surface at the interface with a dielectric. The electromagnetic field resulting from SP oscillations decays exponentially away from the metal surface and is sensitive to refractive index changes at the immediate interface of the metal. This chapter will introduce plasmonics and the prominent toolbox, which it provides for the development of multiple biosensing techniques and applications based on the refractometric sensing principle.

Depending on the geometry of the underlying metal surface, SPs can be described in two main modes, the Surface Plasmon Polaritons (SPPs) propagating along planar metal films, and Localized Surface Plasmons (LSPs) that are localized oscillations in metallic nanostructures, as schematically illustrated in Figure 3.1.

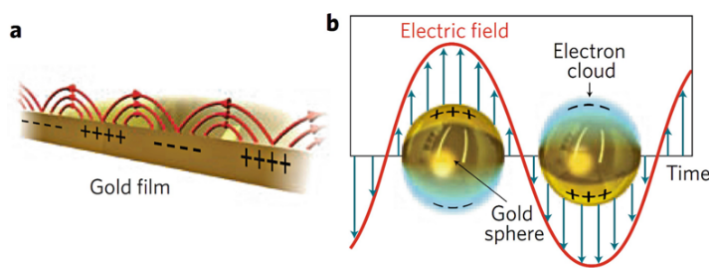


Figure 3.1 Surface Plasmon Polaritons (SPPs) propagating along planar metal films (a), and Localized Surface Plasmons (LSPs, b). Image reproduced from [99].

3.1. Surface Plasmon Resonance

First observed in experiments by Wood in 1902 [100], the phenomenon of surface plasmon resonance (SPR) has since received a thorough theoretical study. The first theoretical treatment of Wood's observations was done by Rayleigh in 1907 [101], however, it has been until the 1960's that a full physical interpretation was done by Kretschmann [102] and Otto [103].

Surface plasmon resonance is associated with electromagnetic excitations, called surface plasmon polaritons, propagating at the interface between a conducting metal and a dielectric. These non-radiative electromagnetic surface waves form when an incident electromagnetic field, such as light, couples to the oscillations of the metal's electron plasma. The waves propagate parallel to the metal-dielectric interface and exponentially decay as the distance from surface increases (Figure 3.2).

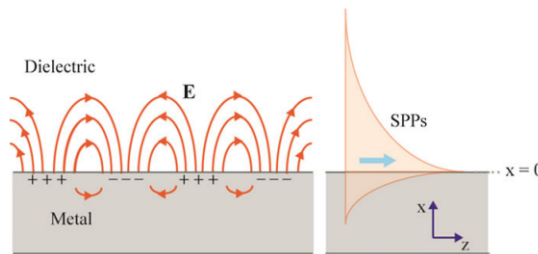


Figure 3.2 Geometry of surface plasmon polaritons. Image reproduced from [104].

The depth of the field propagation into the dielectric, or the decay length, is dependent on the dielectric properties of the metal and the dielectric medium. The typical decay length of an SPP is between 100 and 500 nm [105]. Only the changes in refractive index within the decay length from the metal surface affect the plasmon propagation, and therefore can be detected.

Using the general dispersion relation of SPPs arising from the Helmholtz equation, the wavevector along the interface k_{SP} can be expressed as:

$$k_{SP}(\omega) = \frac{\omega}{c} \sqrt{\frac{\varepsilon_d \varepsilon_m}{\varepsilon_d + \varepsilon_m}} \quad \text{Equation 3.1}$$

where ε_d and ε_m are the complex frequency-dependent dielectric constants of the two mediums (i.e. dielectric and metal), c is the speed of light, and ω is the angular frequency of light. Here, the permittivity of the noble metals can be expressed by Drude model, approximating metal by an electron gas at large frequencies where damping is negligible [106]:

$$\varepsilon_m(\omega) = 1 - \frac{\omega_p^2}{\omega^2} \quad \text{Equation 3.2}$$

Here ω_p is the plasma frequency of the metal is expressed through the number density of electrons N and physical constants:

$$\omega_p = \sqrt{\frac{Ne^2}{m_e \varepsilon_0}} \quad \text{Equation 3.3}$$

Here e is the electric charge, and m_e is the effective mass of the electron, ε_0 is the permittivity of free space.

From the derivation of Equation 3.1 it can be found that SPPs are supported only when $Re(\varepsilon_m(\omega)) < 0$ and $|\varepsilon_m(\omega)| > \varepsilon_d$. Moreover, in Equation 3.2 it can be observed that $\varepsilon_m < 0$ when $\omega > \omega_p$, where materials retain their metallic properties. In this way, SPPs are supported in metal surfaces at limited wavelength range, typically between 100 nm and 1 mm.

Surface plasmon resonance arises when an incident light hits a metal surface at a certain angle of incidence. Part of the energy of incident photons couples to the electrons in the metal surface layer. However, the wave vector k_{SP} is typically greater than the wave vector of the incident light, preventing effective coupling. For this reason, a variety of techniques has been developed to overcome the mismatch.

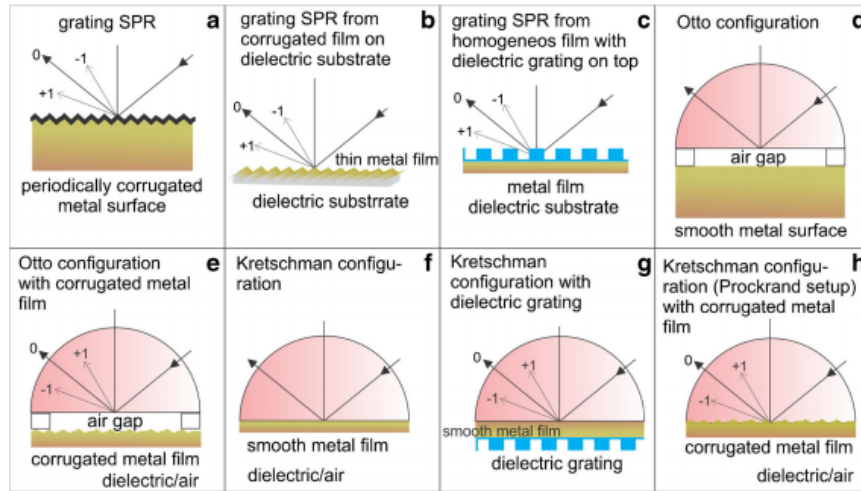


Figure 3.3 Common SPR excitation configurations. Image reproduced from [107].

One of the most common ways to perform the coupling of incident light is Kretschmann geometry of the attenuated total reflection (ATR, Figure 3.4 A) [108]. The polarized light falls at an angle through a high-refractive index glass prism and is reflected from the backside of a thin metal film, typically gold. The defined angle at which resonant coupling occurs is called SPR angle and is dependent on the refractive index of the medium near the metal surface. At that angle part of the energy of the incident light is carried to surface plasmons, therefore the reflected light loses intensity. When the refractive index of the sensing medium changes, plasmons cannot be formed as effectively, and intensity of reflected light changes. In this way, detection can be performed by measuring the changes of the reflected light using a photodetector (Figure 3.4 B). Moreover, quantitative detection can be performed by monitoring the relative

changes in reflected light intensity or by tracking the shift of resonant angle (Figure 3.4 D), where the sensitivity of the sensor can be expressed as the resonant wavelength shift induced by the variation of refractive index of the medium (refractive index unit, RIU), or $\Delta\lambda/\Delta n$.

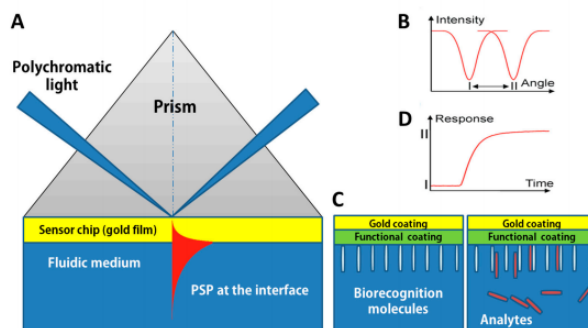


Figure 3.4 (A) Kretschmann geometry of the ATR method. (B) Reflected light before and after change of refractive index. (C) Analytes captured on the metal surface with biorecognition molecules. (D) Real-time detection of molecular interactions measuring SPR angle. Image reproduced from [108].

This makes SPR a powerful tool for biosensing applications. The binding of biomolecules such as proteins and DNA on the surface causes changes in the local refractive index. By functionalizing the metal surface with biorecognition molecules, SPR allows the detection of captured biomolecules in solutions without the use of additional molecular labels (Figure 3.4 C). Moreover, by real-time monitoring SPR signal, biomolecular interactions and binding kinetics between different molecules can be experimentally measured (Figure 3.4 D).

3.2. Localized surface plasmon resonance

Localized surface plasmon resonance (LSPR) is associated with a strong UV-visible absorption by noble metal nanoparticles, that is not present in the spectrum of the bulk metals. In fact, such nano-scale effects have been observed and exploited since medieval times in stained glass to generate beautiful variations of colours (Figure 3.5).



Figure 3.5 The rose window at the Notre Dame Cathedral, Paris, France. Image reproduced from [109].

In contrast to SPPs, the geometrical boundaries in metallic nanoparticles result in localized oscillation of the surface charges [110]. Excited plasmons are highly confined on the nanoparticle surface and rapidly decay into the surrounding medium. The effective refractive index interfaced by the nanostructures can be altered by two different processes. One of them is the refractive index change of the bulk medium (Δn), such as the changes of dielectric medium (e.g. air $n_{\text{air}} = 1$ vs water $n_{\text{water}} = 1.33$). Another is the binding of biomolecules on the nanostructure surface forming a thin monolayer (Δt), typically a few nm thick with a refractive index different from the bulk medium. Accordingly, two different metrics can be defined to express the sensitivity, the bulk and the surface sensitivity [111]:

$$S_{bulk} = \frac{\Delta\lambda}{\Delta n_{bulk}}; \quad S_{surf} = \frac{\Delta\lambda}{\Delta t_{monolayer}} \quad \text{Equation 3.4}$$

The enhanced field confinement of LSPR structures enables higher surface detection sensitivity, compared with SPPs, ultimately achieving the detection of single biomolecules in some cases [112]. Effectively, the nanoparticles act as nanoantennas, converting electromagnetic radiation from the far-field to the near-field and vice-versa. The resonance in the nanoparticles is a function of particle polarizability, and can be tuned by changing the size, shape, and composition of the nanoparticle. For the simplest case of a nanosphere with radius r , the dipolar polarizability α can be expressed as [113]:

$$\alpha_{sph} = 4\pi r^3 \frac{\epsilon_m(\omega) - \epsilon_d}{\epsilon_m(\omega) + 2\epsilon_d} \quad \text{Equation 3.5}$$

Given fixed nanoparticle parameters, the resonant frequency of nanoparticles is dependent on the local refractive index of the medium at the nanoparticle surface. In this way, similar to SPPs, LSPR structures have been used in biosensing applications to detect refractive index changes associated with the binding of biomolecules to nanoparticle surface (Figure 3.6) [114]. When illuminated with incident light, the nanoparticles absorb the light at resonant wavelengths. These resonances are dependent on the refractive index and can be detected in the transmission or reflection spectrum. Nanoparticles suspended in a medium exhibit a tendency to aggregate, which hinders many bioapplications. To avoid the aggregation problem, metallic nanostructures have been assembled on surfaces to enable more robust surface-based LSPR sensing. Metallic nanostructures can be functionalized with biorecognition elements, similar to SPR, to enable detection of biomolecules such as proteins and DNA.

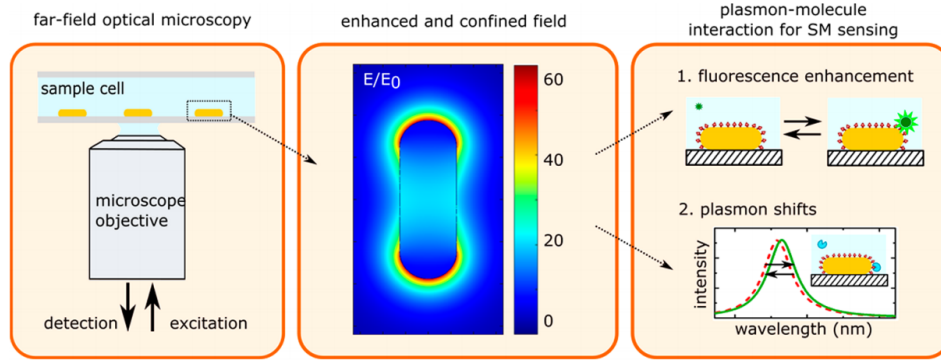


Figure 3.6 Gold nanoparticles assembled on glass surface and functionalized with capture antibodies. Image reproduced from [112].

3.3. Plasmonic nanohole arrays

Nanoplasmonic structures can be designed to combine plasmonic resonances in both SPR and LSPR modes. One of the main such designs that has recently emerged is plasmonic nanohole arrays (NHAs). NHAs are arrays of millions of sub-wavelength nano-perforations in thin metal films, such as gold. These nanostructures were first reported by Ebbesen in 1998 and have received a lot of attention from the scientific community since then [115]. NHAs support propagation of SPPs along the planar metal-dielectric interface, while the nanoholes confine localized plasmon modes. These combined interactions of SPPs and LSPs enable so-called extraordinary optical transmission (EOT) – light transmission that is much larger than predicted by classical diffraction theory.

3.3.1. Single aperture

A single pinhole in a screen is one of the simplest optical elements. Following classical diffraction theory, when light scatters through an aperture of similar linear dimensions

to the wavelength of the incident wave, it diffracts at the edges. The aperture effectively acts as a point source of spherical waves. A theoretical description of the transmission efficiency of diffracted light in the idealized situation of a circular hole (of radius $r < \lambda$) in an infinitely thin perfectly conducting flat metal film was given by Bethe [116]:

$$\eta_B = 64 \left(\frac{2\pi}{\lambda} r \right)^4 / 27\pi^2 \quad \text{Equation 3.6}$$

However, a real aperture has depth and therefore acts as a waveguide. The lateral size of the waveguide defines the cutoff wavelength (λ_c)—wavelength at which light can no longer pass through an aperture. In fact, as the wavelength of incident light increases, the transmission efficiency is attenuated exponentially.

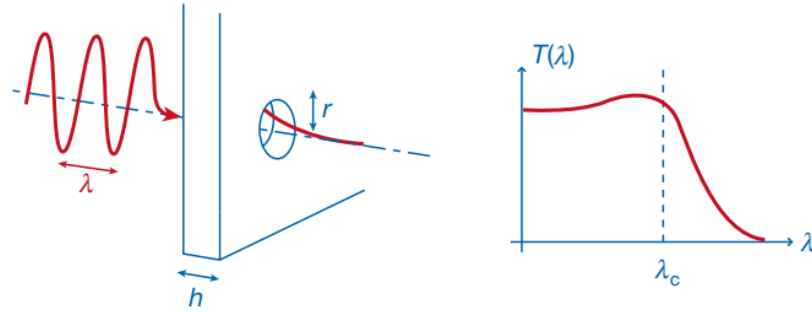


Figure 3.7 Behavior of light transmitted through a waveguide in a metal film changes from propagative to evanescent regime as wavelength increases. Image reproduced from [117].

At the same time, a nanohole in metal film can be imagined as an inversion of a nanoparticle suspended in a dielectric medium. An incident light can induce a dipole electric field on the edges of nanohole just like on the surface of a metallic nanoparticle - but in a reversed orientation. In this way, the polarizability of metallic nanohole can be expressed by switching the permittivity parameters in Equation 3.5:

$$\alpha_{\text{nanohole}} = 4\pi r^3 \frac{\epsilon_d - \epsilon_m(\omega)}{\epsilon_d + 2\epsilon_m(\omega)} \quad \text{Equation 3.7}$$

3.3.2. Periodic nanohole arrays

Advances in modern nanofabrication techniques enable to shape the optical properties of surfaces by sculpturing them with myriads of tailored nanostructures at the scale of the wavelength. One of such structures is periodic arrays of nanoholes in metal films. Nanohole arrays have found wide applications largely thanks to the tunability of their spectral properties and scalability of fabrication. The periodic nanohole structures provide the necessary momentum conservation for the coupling of light into SPs [117]. As was mentioned earlier in section 3.3, nanohole arrays support both SPP and LSP modes. These modes interplay to give rise to the EOT phenomenon. Effectively, the light transmission through NHAs can be described in three main steps, as schematically depicted in Figure 3.8. First, the light couples to SPs on the incident surface. Next, the SPs are transmitted through the holes to the second surface. Finally, re-emission from the second surface results in the EOT. As illustrated in Figure 3.8, multiple scattering and reflection effects happen at the same time.

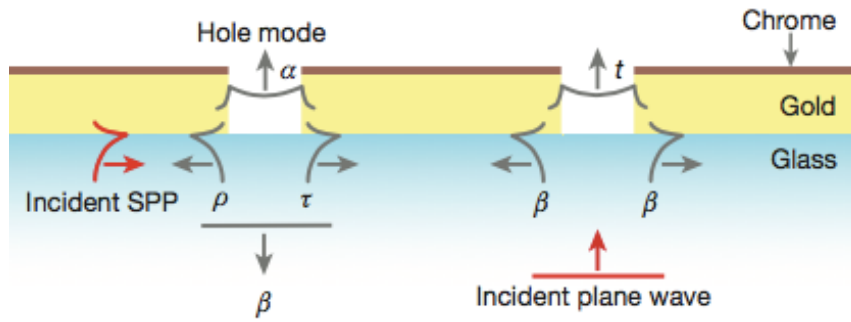


Figure 3.8 Depiction of the EOT. At the right hole: an incident freespace plane wave can scatter into a surface plasmon (β) or couple into the hole (t). At the left hole: an incident surface plasmon can be transmitted (τ), reflected (ρ), coupled onto the hole (α) or coupled to free space (β). Image reprinted from [118].

NHAs effectively act as two-dimensional grating, where the hole-bound LSP modes can decay into SPPs along the metal surface, and the diffraction of incident light provides additional momentum components [119]. This enables SPs excitation in NHAs in normal incidence configuration without the requirement for additional coupling mechanisms, such as in the case of SPR. Moreover, the highly confined LSP modes enable high refraction index sensitivity of NHA sensors. Bulk refractive index sensitivities as high as 400 nm/RIU and 615 nm/RIU were demonstrated in independent studies [120], [121], which are similar or better than other grating-based SPR devices.

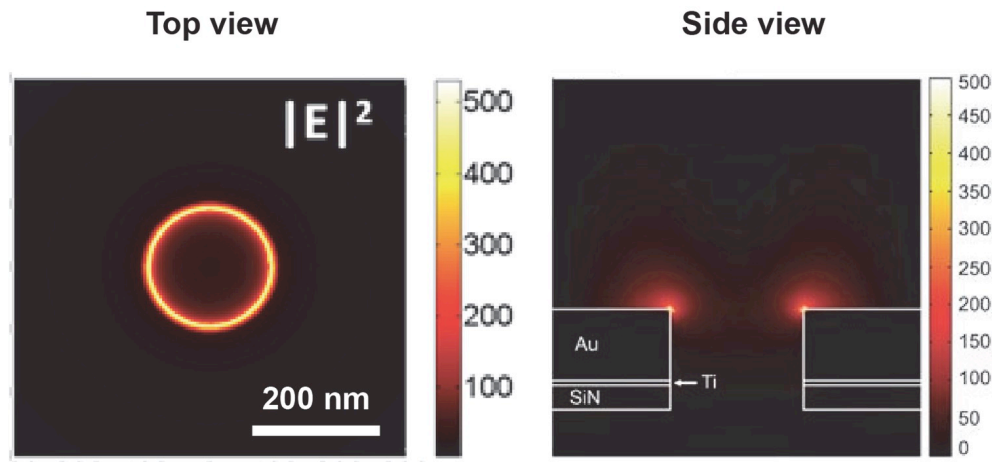


Figure 3.9 Finite-difference time-domain (FDTD) simulation of electromagnetic field around a gold nanohole in a nanohole array. The holes have a diameter of 200 nm and a period of 600 nm; $|E|^2$ represents the field intensity. Image adapted from [122].

Moreover, while most studies and applications of plasmonic nanostructures have so far focused on the exploration of spectral shifts and the corresponding intensity changes, recently the phase response of gold NHAs has been used as well. Yesilkoy et. al. have implemented Au-NHAs in a phase-sensitive platform that allows biosensing over large fields of view [120].

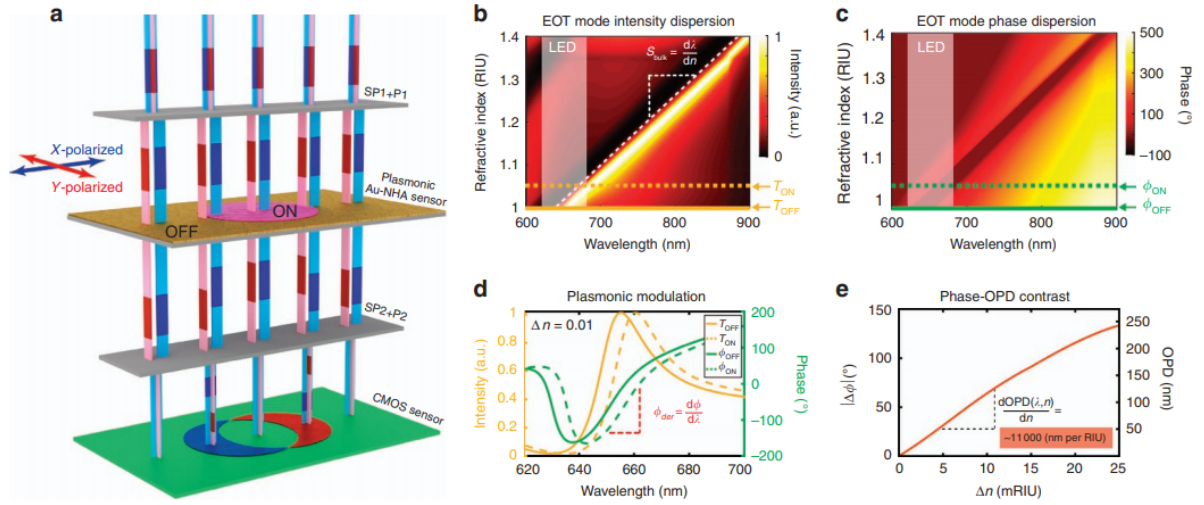


Figure 3.10 Detection principle using phase-sensitive Au-NHA sensor. Image reprinted from [120].

By exploiting plasmonic phase enhancement of NHAs, the platform enabled high-throughput label-free biosensing by detecting phase changes induced upon binding of biomolecules. The enhancement mechanism relies on the temporal phase retardation of light induced by the plasmonic surface at the resonant mode and improves sensitivity over one order of magnitude compared to a plasmonic-free plain glass substrate. The detection of phase response is performed using a lens-free differential interference contrast microscope (LIM) imager, which enables a large field-of-view microarray sensing.

3.3.3. Optical properties and design of nanohole arrays

Extraordinary optical transmission

The phenomenon of enhanced light transmission through nanohole arrays was first observed by Ebbesen in 1998 [115]. Ebbesen found that arrays of cylindrical nanoholes in metallic films exhibit unusual zero-order transmission spectra at wavelengths that are greater than the nanohole dimension and array period, forming sharp transmission

peaks. In fact, the peaks were positioned at wavelengths up to ten times larger than the hole diameter. This phenomenon was named extraordinary optical transmission (EOT).

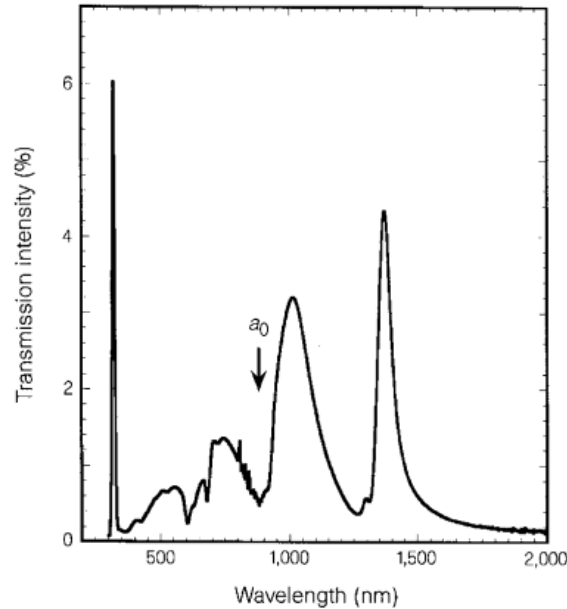


Figure 3.11 Transmission spectrum of a square NHA with 900 nm period, 150 nm holes in a 200nm thick Ag film. Image reproduced from [115].

While this study did not provide a rigorous theoretical framework to describe the principles behind EOT, several important observations were made that gave clues to understanding the phenomenon. First, the periodicity of the holes in the array determined the position of resonant transmission peaks. The width of the peaks was strongly dependent on the aspect ratio of hole depth divided by the diameter. Moreover, the spectra changed significantly depending on the type of lattice geometry, for example array in a square configuration exhibited wider peaks compared to hexagonal [123]. In comparison to NHAs in metal films, NHAs in dielectrics such as Ge lacked the enhanced transmission, suggesting the importance of the metallic film. In addition, the zero-order transmission spectra linearly changed even with the smallest changes in the

illumination angle. This behavior gave the first clue that EOT is related to light coupling to SPs in the NHA gratings.

Later, the characteristic spectral position of EOT resonances was theoretically described as a function of nanoholes periodicity (p), dielectric constants of the metal (ϵ_m) and the dielectric (ϵ_d), and the grating orders i and j :

$$\lambda_{res} = \frac{p}{\sqrt{i^2 + j^2}} \sqrt{\frac{\epsilon_d \epsilon_m}{\epsilon_d + \epsilon_m}} \quad \text{Equation 3.8}$$

One can observe from Equation 3.8 that given a fixed nanohole material and geometry, the position of resonant wavelength λ_{res} of each specific mode is dependent on the dielectric constant of the interfacing medium. Specifically, when biomolecules bind to or unbind from on the NHA surface, this causes a change in local refractive index (and therefore change in the dielectric constant ϵ_d). This causes the position of resonance wavelength to shift, which can be detected in the far-field transmission spectrum.

Nanohole array geometry and film thickness

Nanohole arrays can be fabricated in different metal film of different thickness. A systematic study of the effects of the metal properties and layer geometry on the EOT was given by Hajiaboli et al. [124] and is briefly reviewed below.

Hole diameter

Following the model described by Equation 3.8, the spectral position of EOT peak does not change because the period array is constant. This can be observed in Figure 3.12. Here there are two peaks, the first at shorter wavelengths and the second at longer wavelengths. Interestingly, the position and intensity of the second peak are affected by the nanohole diameter. Larger holes result in red shift and strongly increased intensity of the second peak. This suggests that the first peak of the transmission spectrum mainly

results from SPPs at the surface while the second peak results from LSP modes excited at the nanoholes rims [124]. In this way, the first and the second peaks are associated with scattering orders (1, 1) and (1, 0), respectively.

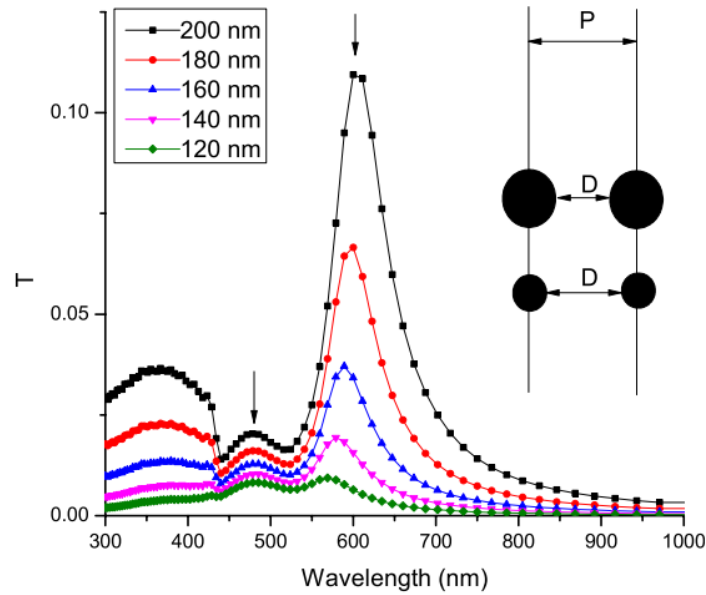


Figure 3.12 Simulated transmission spectrum through NHAs in a gold film. Film thickness is 425 nm, array periodicity is 1000 nm. Image reproduced from [124].

Increased hole diameter results in increased filling factor of the holes. In turn, this gives rise to a stronger in-coupling of the lower energy photon to the film in the form of LSPs. The enhanced in-coupling suggests an enhanced out-coupling of the electromagnetic field, which in turn can be observed as intensified and red-shifted second peak of transmission spectrum (Figure 3.12). It should be noted, that the diameters of nanoholes should remain within the subwavelength range in order to avoid direct light propagation that obscures EOT effects. At the same time, light transmission rapidly decreases as the hole diameter gets smaller, becoming insufficient with hole diameters smaller than 200 nm [125].

Film thickness

We shall consider optically thick metal films, that is films through which the incident light cannot pass without being absorbed on average, e.g. Au films over 100 nm thick. As the metal film thickness decreases, the intensity of the second peak was observed to increase. This is likely explained by a stronger coupling of light to the LSP modes at the front and back sides of the nanoholes. Meanwhile, the behavior of surface propagating SPP modes is a function of lateral dimensions of the array, and therefore they should remain similar for different thicknesses. As can be observed in Figure 3.13, the position of the first peak experiences only a negligible shift. This is an indication that the SPPs are manifested in the first peak at the shorter wavelength spectrum. Interestingly, while the second peak should not experience a shift with changing film thickness, that is not the case. This phenomenon can be attributed to the contribution of LSPs and shows how the coupling of LSPs excited at the rims of the nanoholes affects the overall spectrum.

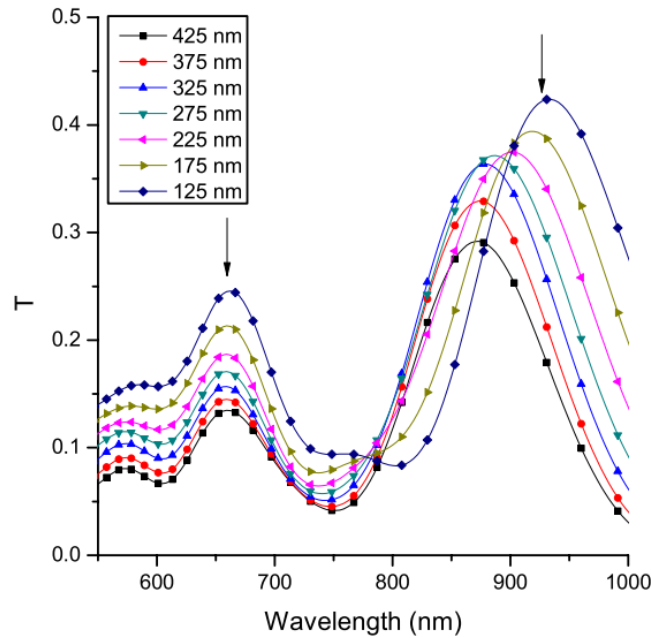


Figure 3.13 Transmission spectrum through NHA with 200 nm diameter and 1400 nm array period as a function of metal film thickness. Image reproduced from [124].

In the visible and near-infrared range metal films, including gold and silver, become optically semi-transparent at thicknesses below 100 nm. In the case of such thin films, the interactions become more complex and the bright EOT mode becomes obscured with transmitted light [126]. However, the SPPs and LSPs support the sub-resonant modes, resulting in extinction dips in the transmission spectrum (Figure 3.14). The dip, or the dark mode, is similarly sensitive to the refractive index changes and can be used for sensing applications.

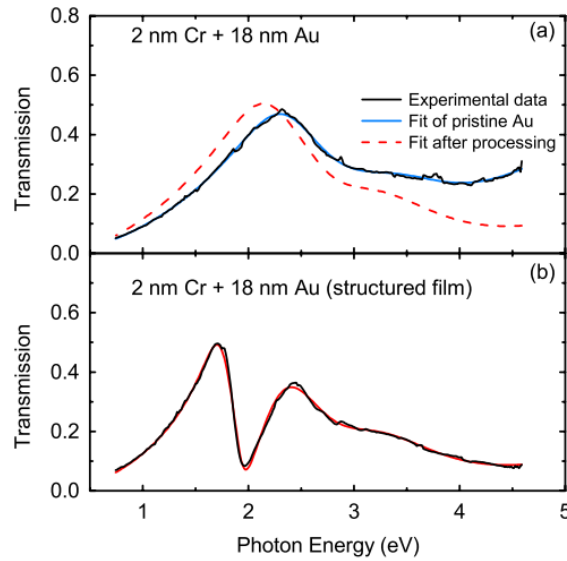


Figure 3.14 Transmission spectra of (a) plain gold film and (b) hole array at normal incidence. Period = 300 nm; hole diameter $d = 200$ nm. The transmission was fitted by using Au dielectric constants and an additional Lorentz oscillator. Image reproduced from [127].

Array periodicity

The lateral dimension of nanohole arrays is one of the main characteristics defining the spectral peak position. As can be observed from Equation 3.7, the wavelength of the resonant peak is linearly dependent on the period. The larger the period, the longer are the wavelengths at which the resonant modes occur. This can be attributed to the SPP

modes in nanohole array structures. SPPs propagate laterally along the metal-dielectric interface and therefore are a function of lateral dimensions of the array. Meanwhile, the LSPR modes remain unaffected with changing array period, as long as the shape and size of the holes remain the same. Therefore, the falling slope of the second peak remains unchanged. The decrease in the intensity of the second peak can be attributed to the lower filling factor, as the periodicity of the structures becomes longer.

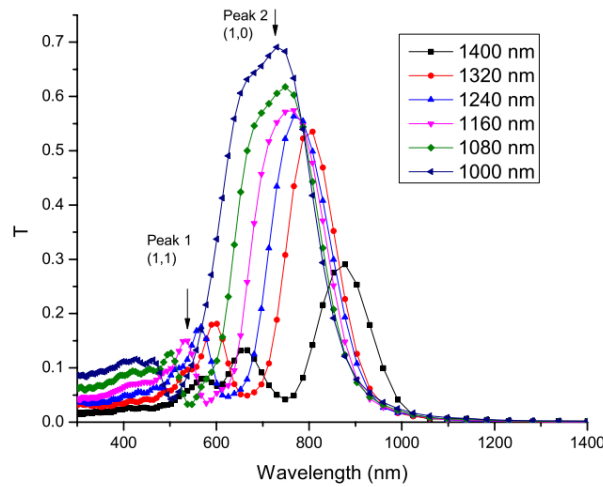


Figure 3.15 Transmission spectra of gold nanohole arrays (hole radius = 200nm, film thickness = 425 nm) as a function of different array periodicities. Image reproduced from [124].

Film material

Gold and silver are the most widespread metals used in the nanohole array fabrication thanks to relatively low losses at visible and NIR ranges and high conductivity. Compared to gold, silver is known as a metal with lower absorption in the visible range. This reduced absorption in silver films leads to longer propagation lengths of the SPPs and a stronger coupling of the resonant modes. NHAs made of silver can also produce EOT peaks that are narrower (higher quality factor) [128], and therefore theoretically should be more favorable for sensing applications. However, there are two important

factors that have widely established gold as the metal of choice in the development of NHA applications. First, silver is prone to corrosion upon contact with air. This is in contrast to gold that is highly inert and stable under atmospheric conditions. When silver is exposed to air, it reacts with oxygen and sulfur, which leads to the formation of silver oxide and silver sulfide film over the thin plasmonic surface. This corrosion effect affects the plasmonic properties of silver films and deteriorates the spectral shape of transmission peaks. This not only makes the silver nanostructures hard to store over time but also makes spectral properties of nanostructures less predictable. Secondly, the use of metallic nanostructures for biosensing applications requires an effective surface chemistry toolbox in order to functionalize biomolecules on the sensor surface. The functionalization of gold is a better established and more efficient process compared to silver. Gold functionalization through thiol compounds is a highly effective process that enables the immobilization of a wide variety of biomolecules. These factors have made gold nanohole arrays particularly suitable for biosensors development.

Adhesion layer between gold film and substrate

Fabrication of metallic nanostructures from gold has been established as the method of choice for plasmonic biosensors including plasmonic nanohole arrays not only because of excellent optical transmission resonant performance, but also suitable chemical properties. As discussed above in section 3.3.3, the plasmonic metal film has to be sufficiently thin to allow EOT. This imposes limits on the thickness of metal films typically in the range of 100 nm – 200 nm. Such thin films of metal, however, are not mechanically robust enough to support themselves as free-standing membranes. To provide mechanical stability, the fabrication of nanohole arrays requires gold deposition on a substrate, such as silicon or silicon oxide. However, the affinity of gold to these common materials is relatively low. When deposited directly, gold film tends to delaminate from substrate during the fabrication and especially experiments. To avoid delamination, an intermediate adhesion layer is added between the gold and the substrate to stabilize the adhesion. Some of the commonly used adhesion materials are

chromium (Cr) and titanium (Ti). These metals possess higher affinity to both gold and silicon or silicon oxide and enable stable formation of thin gold films. Moreover, Cr and Ti are non-plasmonic metals, and therefore do not support propagation of plasmonic modes on the backside of nanohole arrays between gold and substrate, unlike dielectric adhesion layers [120]. This suppression of irrelevant surface modes induced by the gold-substrate interface helps isolate and monitor only the (1, 0) EOT peak of gold-dielectric interface through a wide spectral range. It should be taken into account that Cr and Ti have high optical absorption. For this reason, the thickness of adhesion layers is kept at ~ 10 nm to maintain EOT peak amplitude, while suppressing irrelevant gold-substrate modes.

3.4. Nanohole array biosensors

Gold nanohole arrays are promising for the development of biosensors, including lab-on-a-chip and point-of-care devices, due to their potential for ultra-sensitive multiplexed detection. In particular, gold nanohole arrays combine some of the best attributes of SPP and LSP sensors. The confined nanohole LSP modes offer high refractive index sensitivity, while fabrication from planar gold films enables robust large-scale manufacturing. At the same time, NHAs operate in normal incidence illumination, which enables a compact detection footprint. Traditionally, plasmonic nanohole arrays have been used for biosensing experiments in refractive-index (RI)-based sensing schemes.

The performance of such sensing schemes can be characterized by the sensitivity to bulk refractive index changes and the refractive index resolution. The refractive index sensitivity is defined as the ratio between the EOT spectral shift per unit of refractive index change. It can be experimentally measured by changing the refractive index of the dielectric medium over sensor areas and tracking the shifts in the spectral position of

the EOT peak. In this case, the bulk refractive index sensitivity is defined as the ratio of $\Delta\lambda/\Delta RI$, denoting the spectral shift of the EOT peak per unit change in the refractive index of the surrounding medium. Importantly, when developing bioapplications refractive index sensitivity is not the only factor that defines the performance of a plasmonic biosensor. First, the electromagnetic field confinement at the sensor surface is critical to understanding biomolecular sensitivity [129], [130]. The dimensions mismatch between the biomolecule size and the decay length of plasmons affects the sensor sensitivity. In gold nanohole arrays the decay length of plasmons into the medium is typically ~ 100 nm [131]. Biomolecules have sizes ranging between few nanometers and few tens of nanometers, expressed as a molecule's hydrodynamic radius. Therefore, in contrast to the uniform refractive index change induced by a dielectric medium, the binding of biomolecules on the sensor only changes the refractive index at the scale of biomolecule size in the z-direction away from the sensor. In this way, the effective refractive index encountered and sensed by the plasmons is averaged over their decay length.

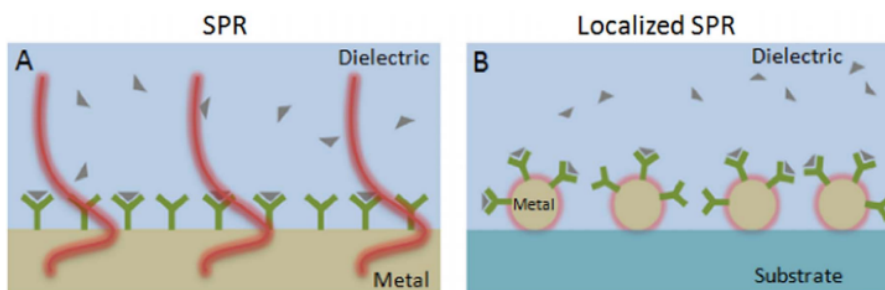


Figure 3.16 Schematic illustration depicting different depths of plasmon decay lengths in plasmonic biosensors (not to scale). Image reproduced from [132].

Long decay lengths (> 200 nm) will result in averaging of refractive index over large penetration depths and reduce sensitivity. Meanwhile, short plasmon decay lengths (< 20 - 30 nm) will not allow sufficient space for surface functionalization with biorecognition elements, and the binding of analytes above the decay length away from

the sensor surface would not be effectively detected. It is critical that the plasmonic sensor supports plasmons with decay length at the scale of the thickness of the biofunctionalization layer on the sensor surface. Second, the effective detection of biomolecules is determined by the functionalization of the sensor [129], [133]. The chemical and biological molecules immobilized on the surface ensure efficient capture of the analytes, and prevent non-specific binding of other molecules that can be present in the sample [134]. The sensitivity and specificity of the sensor are greatly affected by the functionalization and need to be optimized for every specific biosensing application. Third, the sensitive and robust biodetection using plasmonic sensors relies on the performance of instrumentation used for sensor read-out and analyte introduction. The sensitivity and noise of imaging spectrometer or the camera are critical to detect small spectral changes associated with the binding of small analytes in low concentrations. The microfluidic components used to introduce the sample are another factor determining the performance of a biosensor [135]. The use of a narrow microfluidic channel to introduce the analyte sample can be used to improve sensitivity by beating the diffusion-limited regime of analyte flux to the sensor. However, such microfluidic set-ups use fine microfluidic chips that can be prone to clogging. Moreover, active microfluidic flows require sample injection under high pressure using pumps, that can be bulky, expensive, and unreliable. The use of Au-NHAs have been studied in a number of biosensing applications that range from the detection of proteins [136], [137] to self-assembled monolayers [138], exosomes [139], viruses [140], [141], bacteria [142], and cell secretion [143]. Moreover, a number of studies explored the potential of Au-NHAs for miniaturized biosensors by eliminating the spectrometer from the detection schemes and exploiting intensity shifts or phase changes associated with analyte binding [120], [144]–[147].

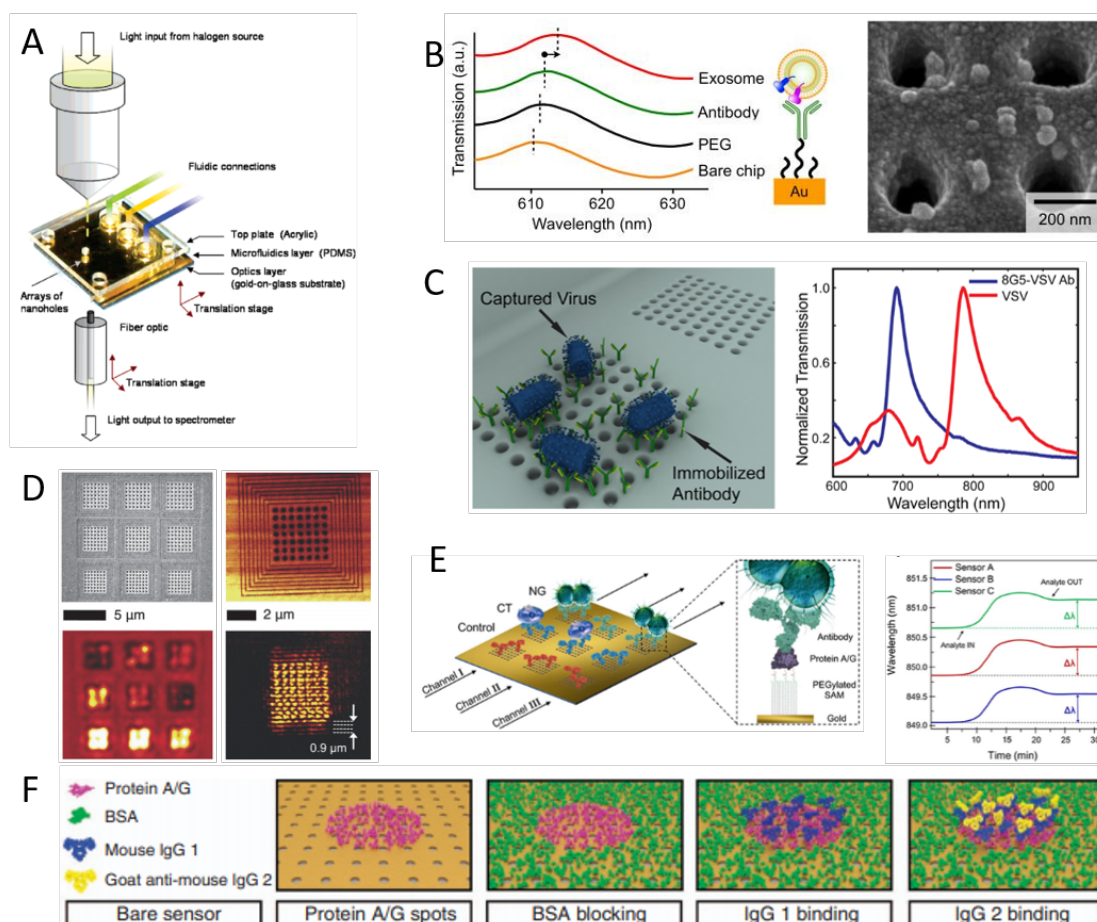


Figure 3.17 Sensing applications of Au-NHAs. A) On-chip detection using nanohole arrays in spectral transmission mode optical configuration. Image reproduced from [148]. B) Detection of exosomes using Au-NHAs. Image reproduced from [139]. C) Virus detection on Au-NHAs. Image adapted from [140]. D) Imaging based detection using gold nanohole arrays. Image adapted from [144]. E) Multiplexed detection of bacteria using Au-NHAs. Image reproduced from [142]. F) Detection of proteins. Image reproduced from [120].

Chapter 4

Nanoparticle enhanced plasmonic biosensor for digital biomarker detection in a microarray

A. Belushkin, F. Yesilkoy and H. Altug

Institute of BioEngineering, École Polytechnique Fédérale de Lausanne, CH-1015
Lausanne, Switzerland

Post-print version of the article published in ACS Nano (volume 12, issue 5, p4453-4461): <https://pubs.acs.org/doi/abs/10.1021/acsnano.8b00519>

Copyright American Chemical Society. Reproduced with permission.

My contribution: Idea conceptualization and study design, conducting numerical simulations, performing experiments, results analysis, and manuscript drafting.

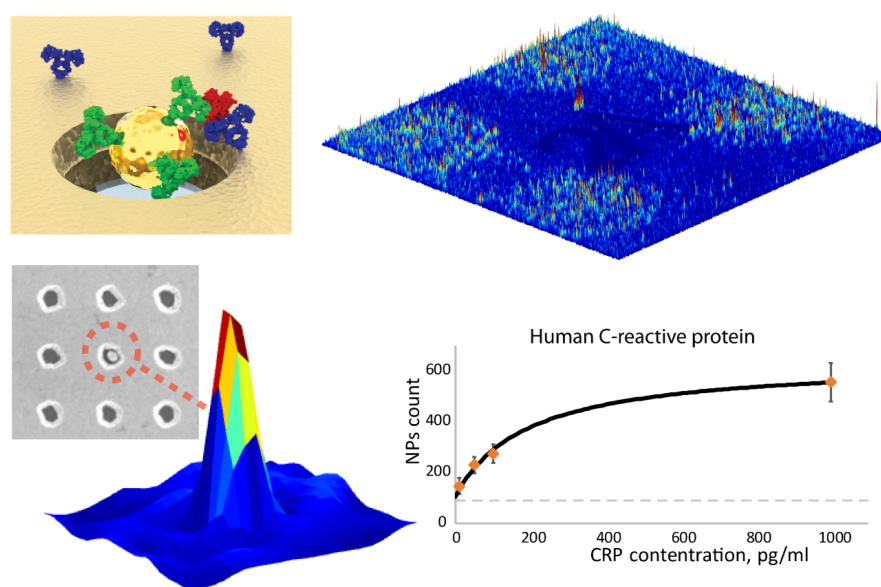
A patent application was filed based on this work:

<https://patentscope.wipo.int/search/en/detail.jsf?docId=WO2019186416>

4.1. Abstract

Nanophotonic devices provide a prominent toolbox for biosensing applications in the fields from biological and pharmaceutical research to medical diagnostics and global health due to their capacity for highly sensitive and multiplexed biodetection from small sample volumes in a compact footprint. In particular, nanoplasmonic devices have become a paradigm for biomolecular detection enabled by enhanced light-matter interactions, however, their requisite detection sensitivity usually comes at the cost of optical complexity of the readers. Here, we present a novel plasmonic biosensor that

allows visualization of single sub-wavelength gold nanoparticles (NPs) on large-area gold nanohole arrays (Au-NHAs) on a simple bright-field imager. The new sensor generates image heatmaps, which reveal the locations of single NPs as high-contrast spikes, thus enabling the detection of individual nanoparticle-labeled molecules. In contrast to conventional plasmonic biosensors, which monitor spatially averaged signals from spectral resonance shifts, our technique exploits the digital quantification and localization of distinctive local extraordinary optical transmission quenching on Au-NHAs caused by individual NPs, associated to single molecule binding. We implemented the proposed method in a sandwich immunoassay for the detection of biotinylated bovine serum albumin (bBSA) and human C-reactive protein (CRP), a clinical biomarker of acute inflammatory diseases. Our method can detect 10 pg/ml of bBSA and 27 pg/ml CRP in 2 hours, which is at least four orders of magnitude lower than the clinically relevant concentrations. Our sensitive and rapid detection approach paired with the robust large-area plasmonic sensor chips, which are fabricated using scalable and low-cost manufacturing, provides a powerful platform for multiplexed biomarker detection in various settings.



Scheme 4.1 Abstract

Keywords:

biosensors, gold nanoparticles, plasmonic nanohole arrays, plasmonic imaging, digital molecule detection, sepsis biomarker detection.

4.2. Introduction

Nanophotonics is offering new opportunities to realize high performance biosensors for the fields ranging from biological and pharmaceutical research to medical diagnostics and global healthcare [149]–[153]. For instance, the management of acute diseases such as inflammation and infections [154] or chronic conditions such as cancer [155] could benefit profoundly from rapid, sensitive and cost-effective on-site diagnostic tools. Conventional laboratory techniques, such as enzyme-linked immunosorbent assay (ELISA) [156] and fluorescent labelling [157], [158] can achieve relevant sensitivity levels of molecular detection, however they require complex optical read-out, multiple incubation-washing steps and fluorescent tags that can be expensive, unstable and difficult to produce.

Nanophotonic resonators can efficiently funnel light into nano-scale volumes compatible with biomolecule dimensions, thereby strongly enhance light-matter interactions and transduce molecular surface binding events into far-field optical signals [159]. The high sensitivity of nanophotonic biosensors combined with the scalability of detection schemes, low-cost operation and capability for multiplexed measurements make them prominent for various biosensing applications. Among the recent ones, optical nanobiosensors based on whispering gallery mode [160], [161] and hyperbolic metamaterials [93] were shown to provide some of the highest sensitivities down to single-molecule detection [162]. However, these techniques require complex and bulky

read-out set-ups, intricate fabrication procedures and have limited scalability hindering their use as cost-effective and multiplexed biosensors.

On the other hand, nanoplasmonic resonators, made of noble metals, couple the photon energy to the collective oscillations of the metal's free electrons, also known as surface plasmons, which interact with the biomolecules at the metal surface [163]. A number of nanoplasmonic devices have been engineered to efficiently probe the local refractive index variations upon the biomolecular surface binding events yielding high refractometric sensitivities [93], [164]–[167]. So far, both the propagating (SPR) [168] and localized surface plasmons (LSPR) [169], [170] have been widely explored for biosensing applications. Particularly, the Au nanohole arrays (Au-NHA) have been prominent plasmonic systems because they can be operated in a robust collinear optical configuration allowing integration in low-cost, easy-to-use, and portable platforms [145]–[147], [171]. The periodic Au-NHAs exhibit a sharp extraordinary optical transmission (EOT) resonance associated with a dip and a peak in the far-field spectrum due to the interplay of coherently interfering resonant interactions and grating effects (Figure 4.1E i.) [172]. Previously, Au-NHAs were explored for numerous biosensing applications ranging from the detection of proteins [173], [174] to exosomes [139], viruses [140], [141] bacteria [142], and cell secretion [143], mainly based on spectral data monitoring. In an attempt to miniaturize the Au-NHA based biosensors, intensity imaging in transmission was used to detect the shifts of the EOT peak without the need of a spectrometer [145]–[147]. Intensity imaging enables 2D large-area detection and can be performed using a narrowband illumination source, such as an LED, tuned to the EOT peak to monitor variations in the transmittance due to the spectral shift of the resonance (see Figure 4.1E ii). Although the approach can be realized with a 2D image sensor array, such as charge-coupled device (CCD) or complementary metal-oxide-semiconductor (CMOS), on a portable optical reader, its previous implementation [146] using Au-NHAs could only achieve detection of 4 $\mu\text{g/ml}$ protein, significantly above the relevant clinical concentrations of most biomarkers. In these conventional

spectroscopic and imaging read-out schemes, the signal transduction relies on the spectral shifts in plasmonic transmission resonances due to refractive index changes induced by the formation of an analyte monolayer with a certain layer density and thickness. Consequently, the sensitivity levels of such approaches are inherently limited by the concentration and the size of the analyte molecules, as well as non-specific interactions from complex samples.

Here, we present a novel nanoparticle enhanced imaging-based plasmonic biosensing technique using Au-NHAs that enables highly sensitive protein detection with single analyte resolution. By digital quantification and localization of individual Au-NPs (100 nm diameter) under bright-field imaging on large area plasmonic imaging surface, the technique enables the detection of single nanoparticle-labeled proteins. We implement the technique in a one-step sandwich immunoassay. After being captured by the first (capture) antibody immobilized on plasmonic Au-NHAs, the protein biomarker is recognized by a second (detection) antibody conjugated to Au-NPs in solution (Figure 4.1A). Upon binding to the analyte, Au-NPs locally disturb the near-fields of the Au-NHAs (Figure 4.1E iii.), leading to a strong local transmission suppression in the far-field. These distortions in the transmission from the small vicinity of the NPs are detected under narrow-band illumination at the EOT peak in the visible range (Figure 4.1B-C), creating plasmonic intensity heatmaps that allow visualization of individual nanoparticle-labeled analytes as high contrast spots. We first applied this novel biosensing approach in a proof-of-principle detection of biotinylated bovine serum albumin (bBSA, 67 kDA) and then human C-reactive protein (CRP, 100 kDA), a well-established biomarker used for clinical diagnosis and management of acute inflammatory diseases [175]–[178]. We show that our approach enables the detection of bBSA down to 10 pg/ml and CRP down to 27 pg/ml limit-of-detection (LOD). This result is at least four orders of magnitude below CRP levels determining patients at high risk of inflammatory diseases [179], [180] and is well comparable to the established fluorescence amplification techniques, such as ELISA [181]. At the same time, our

technique avoids lengthy signal amplification steps and the plasmonic chips and NPs are stable over time, unlike fluorescence labels that experiences photobleaching. In addition, the plasmonic signals are highly confined at the sensor interface and are unaffected by the bulk background, which enables the method to be used in real-time measurements. Importantly, the Au-NHA sensors are fabricated using low-cost wafer-scale deep-UV lithography (DUVL) producing exceedingly robust and uniform large-area chips on solid transparent substrates (Figure 4.1D) [182]. In combination with a simple bright-field imaging set-up in a microarray format, our biosensing technology can be scaled to perform clinically relevant biomarker detection in a highly multiplexed manner.

4.3. Results and Discussion

4.3.1. Principle of detection

The extraordinary optical transmission in Au-NHAs occurs through the hybridization of propagating surface plasmon polaritons (SPP) and localized surface plasmons (LSP) coupled to the nanoholes [172]. The propagating SPPs are excited by normally incident light through momentum matching by the periodic nanohole grid, due to a phenomenon known as Wood's anomaly [183]. This subradiant propagating mode is strongly damped through the radiation channels created by the strong field localizations at the nanoholes, leading to sharp Fano-shaped transmission peaks at the resonant wavelengths in the far-field spectrum (Figure 4.1E i.). The transmission peak position is highly sensitive to the refractive index changes at the gold-medium interface and

therefore can be used for the detection of molecular binding at the NHA surface [184].

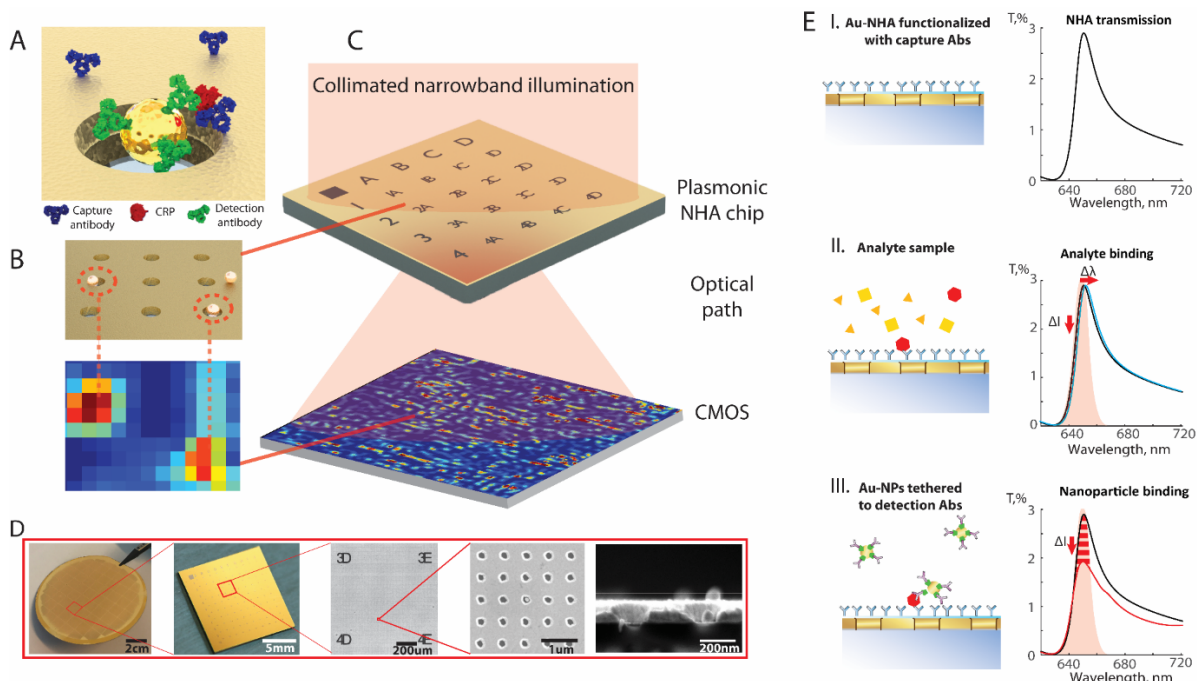


Figure 4.1. Nanoparticle enhanced plasmonic imager for digital biomarker detection. (A) Antigen (red) is recognized by capture antibodies (blue) immobilized on the Au-NHA and then by detection antibodies (green) tethered to Au-NPs. (B) Strong local suppression in the transmission by Au-NPs creates intensity dips (i.e. red spots) at the corresponding locations of the captured image. (C) Bright-field imaging set-up under narrow-band illumination at the Au-NHA EOT resonance to detect distortions in transmission from plasmonic NHA chip. For accurate image processing, the biosensor chip is patterned with microarray labels. The CMOS camera displays transmission signal as an image heatmap enabling digital detection of biomolecules. (D) Left to Right: Au-NHA wafer with 50 sensor chips robustly fabricated using scalable low-cost techniques. Au-NHAs uniformly cover the entire plasmonic sensor surface. SEM of a post-patterned chip with microarray marks. SEM of Au-NHAs ($D = 200$ nm, $P = 600$ nm) with a single Au-NP bound in a hole. Side-view SEM of two neighboring nanoholes with a NP inside one of the nanoholes. (E) I. Simulated transmission spectrum of Au-NHAs exhibiting EOT peak at 650 nm in air. II. Biomolecule binding causes minuscule

spectral shifts in peak position. III. Binding of Au-NPs to the Au-NHA surface results in strong local suppression of the EOT peak.

Contrary to the conventional detection approaches based on spectral peak shift monitoring [139]–[143], [145]–[147], [173], [174], our transduction relies on the far-field intensity-imaging of the local EOT distortion induced by the binding of functionalized nanoparticles. To numerically investigate the local effects created by the Au-NP and the associated changes in the far-field spectrum of the Au-NHAs, we used a commercially available finite-element frequency domain solver (CST microwave studio 2016, Materials and Methods Section). A unit-cell, composed of 3×3 Au nanohole array (diameter=200 nm period=600 nm) with periodic boundary conditions, is excited from top with normally incident TM mode (Figure 2A). The size of the simulated 3×3 unit cell was chosen to match to the diffraction-limited spot (1.8 μm) resolved in our experimental imaging set-up.

When the 100 nm diameter gold nanoparticle binds to the inner walls or the vicinity of the nanohole rim, the localized dipolar resonance is disturbed. This local distortion in the resonant interactions leads to alterations in the radiation pathways and creates suppression of the EOT peak in the far-field (Figure 4.2B). We explored the effect of the NP position on the resonance modes and found that when a NP binds to the top surface of Au-NHA, its impact on the transmission depends on how close the NP is to the nanohole rim, where the hot-spots of localized hole modes reside. Figure 4.2B shows that as the NP gets closer to the nanohole, the peak suppression increases, which correlates with the distortion of the localized enhanced fields presented in Figure 4.2C. When a NP is on the gold surface far from the nanohole, we observed that its effect on the NHA transmission is insignificant. This could be due to the spatially limited interaction of the propagating plasmon modes with the small NP volume. Whereas, a NP inside a nanohole produces a drastic distortion on the localized modes, suppressing the transmission significantly. Since the Au-NHAs have a symmetric geometry, their resonances are polarization independent and can be excited with unpolarised light. A

NP trapped inside the nanohole can distort the dipolar modes in all lateral directions (see Figure S4.1) for excitation polarization effect), resulting in a stronger suppression than the surface bound NPs close to the nanohole rim.

We also investigated the effects of NP size on the numerically computed far-field transmission spectra when Au-NPs of various diameters are entrapped inside a nanohole. Figure 2D shows that the suppression of the transmission peak increases with the NP diameter and saturates at 100 nm. Moreover, it is essential that experimentally the NPs can easily fit inside the nanoholes, both of which can have minor size variations. This defined our choice in the experimental measurements of Au-NPs with 100 nm average size ($\pm 10\%$ dispersity).

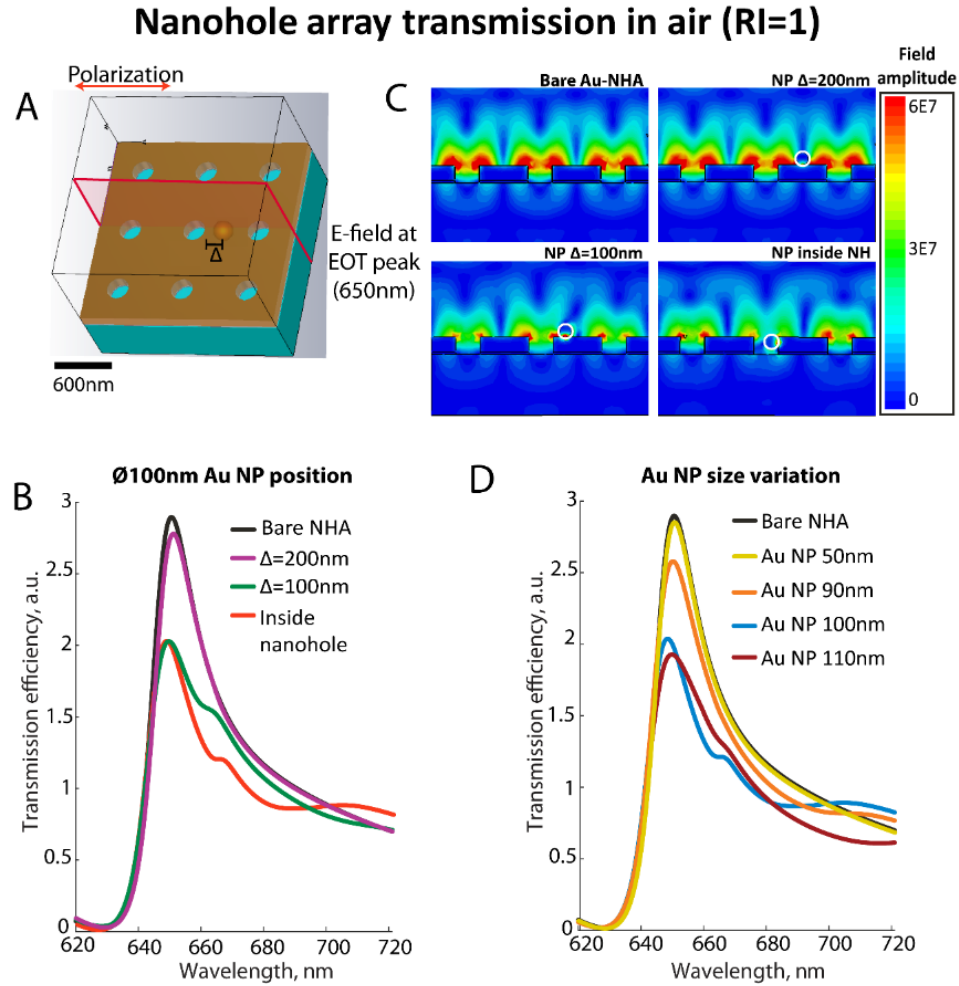


Figure 4.2. Simulated transmission spectra and electric near-field maps of the Au-NHAs distorted by Au-NPs. (A) Unit cell of 3x3 nanohole array (D = 200 nm, P = 600 nm) used in the FEFD simulations excited from top with TM mode and using periodic boundary conditions. (B) Au-NP position dependent EOT transmission spectra of Au-NHAs. The peak suppression increases when Au-NP is bound inside the NH or close to the NH rim and is minimally affected when placed far from the NH. (C) Cross-sections of Au-NHA E-field maps at the EOT resonance (650 nm). When Au-NPs are inside or close to the NH the LSP modes are disturbed strongly, locally suppressing the

transmission. (D) The transmission suppression increases with the NP diameter, saturating at 100 nm.

We also numerically investigated the effect of a dielectric SiO₂ NP with 110 nm diameter and did not observe any amplitude change in the transmission peak of the Au-NHA, whether placed inside or outside of the nanohole (Figure S4.2). These are expected outcomes as the local fields can penetrate through the dielectric media without being distorted, yet a minuscule shift in the resonance wavelength is caused by the change in the effective refractive index of the top medium.

The strong local transmission quenching induced by the gold nanoparticle is critical for our distinctive detection mechanism. Numerical calculations indicate that individual particles can produce sufficiently strong spikes on the captured intensity contrast images from the plasmonic surface to be detected in simple bright-field scheme.

4.3.2. Plasmonic imaging of Au NPs on Au-NHAs

For experimental demonstrations we used uniformly patterned Au-NHA (diameter = 200 nm, period = 600 nm) sensor chips of area 1 cm². The plasmonic nanostructures uniformly covering entire 4-inch quartz wafers were fabricated using a robust high-throughput DUVL lithography [182] (Figure 4.1D), yielding multiple low-cost sensor chips (50 chips/wafer), which is crucial for biosensing applications.

We post-patterned Au-NHA wafers defining 10 x 10 microarray regions on each chip by patterning labels using photolithography and metal (Ti) lift-off techniques (Figure 4.1D). The size of each labelled microarray region is 800 μm x 800 μm and each microarray region can be functionalized with 2 x 2 bioreceptor sensing spots (150 μm diameter spot), providing a flexible platform for multiplexed measurements.

Our experiments are performed on an inverted microscope with a narrow-band illumination, centred at 650 nm with 10 nm full width at half maximum (FWHM), where

the images are recorded at 1 s exposure on a 1608 x 1608 pixels grayscale CMOS camera. The optical path is configured to reach 30x total magnification using a 0.3 numerical aperture (NA) objective lens and a 0.13 NA condenser. This optical arrangement enables the capture of images covering a 385 x 385 μm^2 area, with a Rayleigh diffraction-limited spot size of

$$R = 1.22 \frac{\lambda_{\text{illumination}}}{NA_{\text{condenser}} + NA_{\text{objective}}} \sim 1.8 \mu\text{m}, \quad \text{Equation 4.1}$$

Note that this diffraction-limited area corresponds to a 3 x 3 nanohole unit cell, which is considered in the numerical analysis above. A detailed description of the optical set-up can be found in Materials and Methods.

To accurately extract the positions of NPs from the imaging data, we acquire the images of bare Au-NHA chips patterned with non-transparent Ti alignment marks prior to the bioassay (Figure 4.3A). This is important because the transmission of bare Au-NHAs exhibits minor spatial intensity variations, independent of the imaging set-up. This could be attributed to several reasons, such as minor differences in the metal film crystal structure or the nanohole uniformity. In order to account for these minor intensity variations, we reference the images of Au-NHA sensors before and after the bioassay with NPs.

Next, we perform the sandwich bioassay by first functionalizing the Au-NHA chips using a non-contact micro-dispenser with 2D arrays of capture molecules through gold-thiol surface chemistry. Then, the chips are successively incubated with the analyte dilutions and a suspension of Au-NPs conjugated to receptor molecules. See Materials and Methods section for details. After the sandwich assay, the Au-NHA chips are rinsed, dried and imaged again (Figure 4.3B). The images of the corresponding microarray regions before and after capturing the target analyte and NPs are aligned and subtracted using a custom-made Matlab function. The two images are first matched by referencing

to identical microarray alignment marks, then scaled to the same average intensity range, corrected for background illumination gradients, subtracted and normalized. The alignment and subtraction of the images before and after yield highly accurate intensity heatmaps of NPs binding on Au-NHAs, represented as local intensity spikes (Figure 4.3C). Finally, the NPs are automatically identified and quantified from the spikes on the plasmonic heatmap with a fixed-value threshold. The optimal threshold depends on the imaging characteristics of the optical set-up, and was empirically found to be 5 % intensity change in our microscope system by mapping plasmonic images to high-resolution Scanning Electron Micrographs (SEM) for NP verification. The optimal threshold value was chosen to detect the maximum number of nanoparticles, while keeping a low rate of false positive signals.

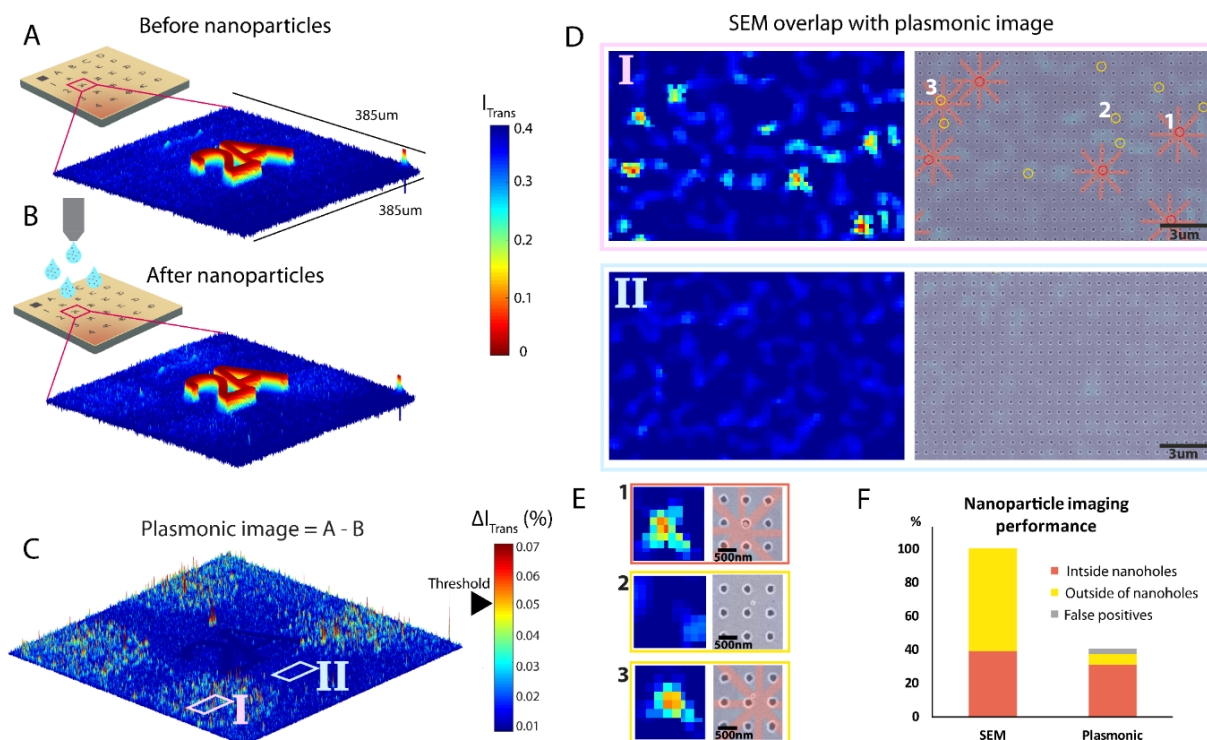


Figure 4.3. Bright-field plasmonic imaging of Au NPs and SEM validation. (A) Reference images of bare Au-NHAs with alignment microarray labels. (B) Au-NHAs

imaged after Au-NPs binding at the same microarray elements shown in (A). (C) The microarray field contains 2x2 arrays of sensing spots. Color-coded surface plot of transmission intensity spikes caused by NPs formed by computational alignment and subtraction of (B) from (A) produce an image heatmap. (D) Left: Computed plasmonic images of Au-NHA areas. Right: Plasmonic images overlapped with the SEMs of identical regions with NPs (I) and without NPs (II), zoomed out from (C). The NPs inside NHs are marked by red circles and NPs outside NHs with yellow circles. (E) Au-NPs inside nanoholes produce strong intensity changes (1) and can be detected. NPs far from NHs cannot be detected by plasmonic imaging (2). A fraction of NPs bound close to the NHs rim produces a sufficient intensity change to be identified by the plasmonic imaging (3). (F) In the experiments statistically 40 % of NPs are bound inside and 60 % outside of NHs (1000 NPs sample size, verified by SEM). Plasmonic imaging correctly identifies around 40 % of NPs, while false positive signals are 3 % (sample of 127 NPs).

4.3.3. SEM validation of plasmonic imaging

To quantitatively analyze the accuracy of our NP enhanced plasmonic imaging technique we matched plasmonic images to the SEMs of the microarray elements. Figure 4.3D shows two representative plasmonic heatmap parts and their corresponding SEM from NPs deposited microspots (I) and NP-free regions (II). The details on the test sample preparation used for the system characterization are provided in the Materials and Methods.

In agreement with the simulations, most of the detected NPs are bound inside the nanoholes, which are marked with red circles on the SEMs in Figure 4.3D (also shown in Figure 4.3E-1). Intensity peaks, recognised as NPs, are highlighted by red stars on the plasmonic images. A small fraction of NPs outside of nanoholes, close to the edges of the holes, could also be detected, supporting our numerical results regarding NP-NHA interactions through disruption of localized nanohole modes (Figure 4.3E-3). As

expected, the NPs that are bound far from the nanoholes were not detected (Figure 4.3E-2). After mapping over 1000 NPs on numerous SEM images, we found that 40 % of NPs bind inside nanoholes and 60 % over the gold surface as summarized in Figure 3F. From the plasmonic heatmaps, we are able to detect approximately 40 % of all nanoparticles, with a 3 % false positive signal rate based on data with a sample size of 127 plasmonic intensity peaks matched to SEM. In addition, our detection is robust against non-specifically binding agglomerates of NPs and large sedimenting contaminants, since they can be easily identified and discarded by the size and the shape of intensity spikes on the plasmonic imaging surface.

4.3.4. Sandwich assay protein detection

We first show the biosensing potential of our NP-enhanced plasmonic imaging method in a proof-of-principle detection of bBSA as depicted in Figure 4.4A. We start by acquiring the reference images on the chips that will be used for the bioassays. Next, the Au-NHAs were surface functionalized with PEG-thiol chemistry to prevent non-specific fouling and ensure optimal protein immobilization through EDC-NHS crosslinker. Then, microarrays of neutravidin (150 pl droplets spotted with 200 μm pitch) were formed using a non-contact micro-dispenser and the remaining areas were blocked with BSA to deactivate non-reacted crosslinker groups. The bBSA dilutions were spiked in 100 μl PBS 1x and incubated with the Au-NHA chips. Finally, a suspension of Au-NPs covalently tethered to streptavidin in PBS 1x with 1 % BSA was incubated. After rinsing with milliQ water and drying under N_2 stream, the second set of images was acquired. Further details on the bioassay procedure are given in the Materials and Methods section. To quantify bBSA, the image datasets were processed as described above. The local intensity spikes were counted over 100 x 100 μm^2 neutravidin spotted areas (see Figure 4.4B), and the results are correlated to the bBSA concentrations (Figure 4.4C). We experimentally show the successful detection of bBSA concentrations down to 10 pg/ml, which is equal to our estimated limit-of-

detection (LOD, computed by adding three times the standard deviation of control signal to the average of the control). These results show that our method reaches the sensitivity of fluorescence amplification techniques, while avoiding the signal amplification step, such as used in typical ELISA. To put into context, a concentration of 10 pg/ml of bBSA translates to 9×10^6 molecules in a 100 μl sample incubated on a sensor chip ($1 \times 1 \text{ cm}^2$). The ratio of a single sensing spot ($100 \times 100 \mu\text{m}^2$) to the entire sensor chip ($1 \times 1 \text{ cm}^2$), is roughly $1:10^4$, which, accounting for molecular diffusion limitation, results in a few hundred molecules reaching to a single sensing spot of $100 \times 100 \mu\text{m}^2$. Taking into account the diffusion limitation of nanoparticle tags and that 40 % of bound particles can be detected binding inside or close to the nanoholes, the 10 pg/ml concentration would result in approximately ~ 10 -100 NPs counts. This estimation is in agreement with our assay, where the 10 pg/ml LOD produced on average 50 nanoparticle counts per read-out spot. The above results indicate that our detection method ultimately operates near the actual diffusion limitation of the system. In this way, the extraction of intensity spikes from the plasmonic imaging heatmap allows us to digitally count the analytes with high sensitivity, contrary to conventional affinity sensors where the signals are averaged over sensor areas.

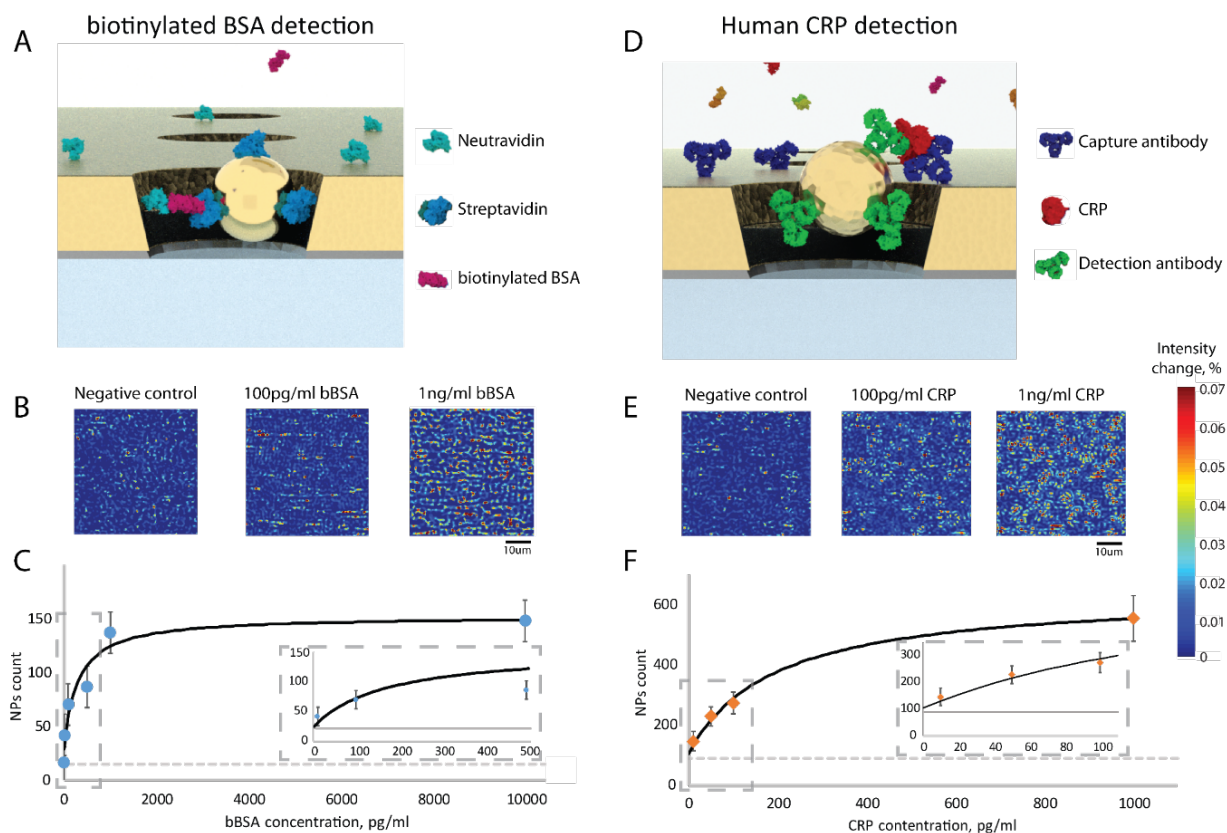


Figure 4.4. Nanoparticle enhanced digital protein detection. (A) Illustration of bBSA sandwich assay. (B) Different concentrations of bBSA are detected as different densities of NPs are seen on plasmonic heatmap images. (C) bSBA calibration curve (LOD = 10 pg/ml). (D) Human CRP sandwich assay. (E) Different concentrations of CRP can be visually distinguished on plasmonic imaging. (F) Human CRP calibration, (LOD = 27 pg/ml).

The flexibility of the developed method enables its use in a variety of bioanalytical applications, by using appropriate biofunctionalization procedures. In order to show the diagnostics potential of the platform, we detect human C-reactive protein (CRP). Human CRP is a blood biomarker, whose levels elevate during acute inflammatory

conditions, such as sepsis and coronary heart disease. Septic shock is caused by the response of body to infections and is one of the most pressing healthcare challenges worldwide with millions of patients diagnosed each year and over 20% of lethal incidence [185]. Therefore, the development of biosensors enabling timely and accurate detection of biomarkers such as CRP can have a profound impact on the effective disease management.

We use the proposed method in a single-step sandwich immunoassay to detect human CRP from bovine serum albumin (BSA) solution. Figure 4.4D illustrates the CRP detection and the details of the assay can be found in the Materials and Methods section.

We experimentally detect CRP concentrations down to 27 pg/ml, which is four orders of magnitude within clinically critical limits, thus opening the path for early-stage disease monitoring. As expected, the LOD for CRP is slightly higher than 10 pg/ml LOD in bBSA detection (Figure 4.4E,F), since the CRP assay was performed in media with high BSA concentration, which may screen antibody-antigen interactions. Additionally, the affinity between anti-CRP antibodies and CRP are normally lower than affinity between biotin and streptavidin or neutravidin.

Figure 4.4C,F presents the calibration curves of bBSA and CRP measurements. The non-specific nanoparticle adsorption, indicated with dashed grey lines, was the main limitation for the LOD in both assays. The control experiments were performed by incubating chips in samples containing no analyte (i.e. bBSA or CRP), while all other assay steps remained unchanged. In CRP measurements, the NP concentration was higher than in bBSA assay, which was reflected on higher specific NP counts, but also higher baseline signal from non-specific NP adsorption. Importantly, our current results are well comparable to the high performance of commercial ELISA kits, which can detect down 3-15 pg/ml of human CRP when performed in a fully equipped clinical laboratories by trained personnel [181].

Moreover, our technique can be used in real-time measurements in aqueous environment as well (Figure S4.9 video shows NPs binding to NHA in-flow), because the localized field disruption of Au-NHAs by Au-NPs is highly surface-confined and is also valid for the plasmonic resonances in wet medium.

Further development of the assay biochemistry and applications with serum or whole blood samples, as well as multiplexed biomarker detection will be essential to explore the full potential of our approach. An implementation of a simple optical reader, which essentially incorporates a narrow-band illumination source, an optical path sufficient for 1-2 μm spatial resolution and a CMOS sensor in conjunction with image processing algorithms, will be another critical step to adapt the technology for on-site diagnostic applications.

4.4. Conclusions

In conclusion, we present a NP-enhanced imaging-based plasmonic biosensing technique using large-area Au-NHA sensors. We show that by disrupting localized plasmon modes in Au-NHA surface with Au-NPs, our method produces plasmonic heatmaps that visualize single sub-wavelength Au-NPs under bright-field imaging. Consequently, by detecting individual Au-NP-labeled molecules we can digitally quantify the single analyte binding events on the imaging surface, enabling multiplexed detection of biomarkers at low concentrations, eminently at the level of current gold-standard laboratory methods, such as ELISA. At the same time, our technique avoids multi-step staining procedures and does not rely on advanced read-out set-ups, such as required in fluorescent techniques. We implemented the proposed method in sandwich immunoassay measurements of bBSA and human CRP, achieving clinically relevant detection limits of 10 and 27 pg/ml, respectively. Prominently, the large-area Au-NHA sensor chips are fabricated in a large-scale low-cost manufacturing, giving versatility

for high-throughput biosensing applications. Overall, our simple and scalable detection approach paired with robust sensor chips promises a flexible platform for highly sensitive multiplexed measurements in various settings, including for point-of-care applications.

4.5. Materials and Methods

4.5.1. Gold nanohole array fabrication

Gold nanohole arrays (Au-NHAs) were fabricated using high-throughput wafer-scale deep-UV lithography (DUVL) and ion beam etching techniques (Figure S 4.10). First, 4-inch fused silica wafers were cleaned with RCA solution (1:1:5 $\text{H}_2\text{O}_2:\text{NH}_4\text{OH}:\text{H}_2\text{O}$), rinsed with deionized water and dried under nitrogen stream. Cleaned wafers were coated with 10 nm of titanium (Ti) and 120 nm of gold (Au) in Alliance-Concept EVA 760 electron-gun evaporator. The NHAs of 600 nm period and 200 nm diameter were patterned using a 248 nm deep-UV stepper (ASML PAS 5500/300 DUV). The nanohole arrays were transferred into metal films with ion-beam etching (Oxford Instruments PlasmaLab 300 IBE) and the photoresist was stripped with oxygen plasma.

Microarray marks on Au-NHAs were formed with Ti to enable image recognition and alignment. The NHA wafers were coated with 1.3 μm AZ1512 positive photoresist and microarray patterns were exposed using Heidelberg MLA150 laser writer. After resist development, 50 nm Ti was evaporated using an electron gun evaporator. Next, the wafers were diced into 1x1 cm^2 chips. The resist was removed from chips by immersing in resist remover with sonication at 70°C for 2 hours. Finally, the chips were cleaned in oxygen plasma for 5 min at 500 W and RCA solution (1:1:5 $\text{H}_2\text{O}_2:\text{NH}_4\text{OH}:\text{H}_2\text{O}$ by volume) for 1 min to ensure uniformly clean gold surface.

4.5.2. Numerical simulations

To numerically investigate the local field effects on Au-NHAs created by the Au-NPs and the associated changes in the far-field spectrum, we used a commercially available finite-element frequency domain (FEFD) solver (CST microwave studio 2016, Materials and Methods Section). We simulated Au-NHAs of 200 nm diameter and 600 nm period in an Au / Ti (120 nm / 10 nm) thin film (optical parameters from Johnson and Christy) on a 500 nm thick SiO₂ substrate with refractive index (RI) = 1.46 and air background media (RI=1). The Ti layer not only serves for Au adhesion to the silica substrate in fabrication, but also suppresses undesired gold-substrate modes, ensuring sharp shape and good isolation of plasmonic resonant modes in Au-NHA transmission [141], [186]. The simulated unit cell contains 3x3 nanoholes with periodic boundary conditions. The unit cell size was chosen to correspond to the ~1.8 μ m diffraction limited spot resolved in our experiments. The illumination is set from top with normally incident TM mode. The electric field was monitored at 650 nm (461 THz).

4.5.3. Optical set-up

The microscope measurements were performed on an inverted Nikon Eclipse Ti-E system. A tungsten halogen lamp was used for illumination together with a narrow-band optical filter (Thorlabs) with 650 nm center wavelength and 10 nm full width at half maximum, matching the plasmonic resonance of Au-NHAs in dry. Optical path included a 20x and 0.3 NA objective lens and a 1.5x intermediate microscope magnification. Images were recorded using a Nikon Qi2 camera with 1 sec exposure and 1.2 digital gain.

4.5.4. Chemicals and biologicals

Ammonium hydroxide solution (ACS reagent, 28-30%), hydrogen peroxide (H₂O₂ 30%), N-hydroxysulfosuccinimide sodium salt (sulfo-NHS), N-(3-

dimethylamino propyl)-N'-ethylcarbodiimide hydrochloride (EDC), 2-(N-Morpholino)ethanesulfonic acid (MES), bovine serum albumin (BSA) lyophilized, biotinylated BSA (bBSA), neutravidin, phosphate buffered saline (PBS) and Tween® 20 were purchased from Sigma-Aldrich. Ethanol (EtOH), absolute was from Thermo Chemicals. Polyethylene-glycol (PEG) thiols terminated with hydroxyl (HS-C6-(EG)4-OH) and carboxyl (HS-C11-(EG)4-OCH₂-COOH) groups, were purchased from Prochimia. Human C-reactive protein (CRP) and anti-CRP monoclonal IgG antibodies PCR-196 and PCR-183, used as capture and recognition antibodies respectively, were provided by DIESSE Diagnostica Senese. Spherical gold nanoparticles of 100 nm diameter coated with streptavidin or with protein-G, supplied at optical density (OD) 3 in PBS with 20 % glycerol and 1% BSA, were purchased from Cytodiagnostics.*

*A 100nm diameter gold nanoparticles concentration of optical density (OD) 1 corresponds to 5.6E9 nanoparticles per 1 ml solution; the relation between OD and NP/ml units is linear.

4.5.5. Au-NHA functionalization

After cleaning in oxygen plasma and RCA, Au-NHA chips were immersed and incubated overnight in 1mM PEG-thiol solution in anhydrous ethanol with OH:COOH terminated PEG mixed in 5:1 ratio. After incubation, chips were gently rinsed with fresh ethanol and milliQ water, then dried under N₂ stream. The chips were activated in 70 mg/ml EDC and 20 mg/ml s-NHS mixture in 0.1 M MES buffer for 20 minutes. Next, the chips were rinsed in milliQ water and dried under N₂ stream. Monoclonal anti-CRP IgG196 or neutravidin were immediately spotted on the activated Au-NHAs using Sciencion S3 piezoelectric non-contact microdispenser. The spotting solution contained either neutravidin or anti-CRP IgG at 200 µg/ml in PBS 1x with 0.5% glycerol. The average droplet volume was 160 pl and the contact area of the formed spot was approximately 100 µm in diameter. The spotted chips were incubated overnight in a

humid atmosphere at 4°C and then blocked with BSA 1 % solution in PBS to passivate the non-reacted EDC-activated groups. Functionalized chips were used in measurements on the same day.

4.5.6. Biotin-BSA sandwich assay

Au-NHA chips spotted with neutravidin and blocked with BSA were briefly rinsed in PBS and immersed in 100 µl of biotin-BSA calibration dilutions prepared in PBS 1x and incubated for 1 hour. Next, each chip was rinsed in PBS 1x with BSA 1% and 0.05% Tween 20 for 20 minutes. After a brief immersion in PBS 1x with BSA 1 %, the chips were incubated for 1 hour in Streptavidin-conjugated gold nanoparticles diluted to OD 0.1 in PBS 1x BSA 1 %. After incubation, the chips were rinsed in milliQ water for 5 mins and dried under gentle N₂ stream.

4.5.7. Au nanoparticle conjugation to anti-CRP antibodies

40 µl of 100 nm gold nanoparticles conjugated to protein G at OD 3 concentration were mixed with 1 µl of 2.1 mg/ml anti-CRP PCR183 antibody by gentle pipetting and incubated overnight at 4°C. Next day, the nanoparticle-antibody solution was diluted in 1 ml of PBS with 1% BSA and centrifuged at 200 g until a nice pellet was formed. After removing the supernatant, the pellet was resuspended in 1 ml of PBS 1x with 1% BSA. Centrifugation and resuspension steps were performed 4 times to remove unbound antibodies from NPs suspension. After the final centrifugation and supernatant removal, the NPs were resuspended in 40 µl of PBS 1x with 1% BSA. The conjugated nanoparticles were used for measurements on the same day.

4.5.8. CRP sandwich assay

Au-NHA chips spotted with anti-CRP IgG 196 and blocked with BSA were briefly rinsed in PBS and immersed in 100 µl of CRP calibration dilutions prepared by

spiking CRP in PBS 1x with 1 % BSA. After 1 hour incubation, chips were rinsed in PBS 1x with BSA 1 % and 0.05 % Tween for 20 min with gentle agitation on a gyro-rocker. After brief immersion in PBS 1x with BSA 1 %, the chips were incubated for 1 hour in IgG183-coated Au-NPs diluted to OD 0.2 in PBS 1x BSA 1 %. After incubation, chips were rinsed in milliQ water for 5 min and dried under gentle N₂ stream.

Acknowledgements

We would like to thank *Center of MicroNano Technology* at *École Polytechnique Fédérale de Lausanne* for providing support on the nanofabrication; *Diesse diagnostic senese SPA* for providing human C-reactive protein (CRP) and anti-CRP monoclonal IgG antibodies. We acknowledge the support of the *École Polytechnique Fédérale de Lausanne* and the *European Union's Horizon 2020 research and innovation program* under grant agreement no. 644956 (*RAIS project*).

4.6. Supplementary Figures

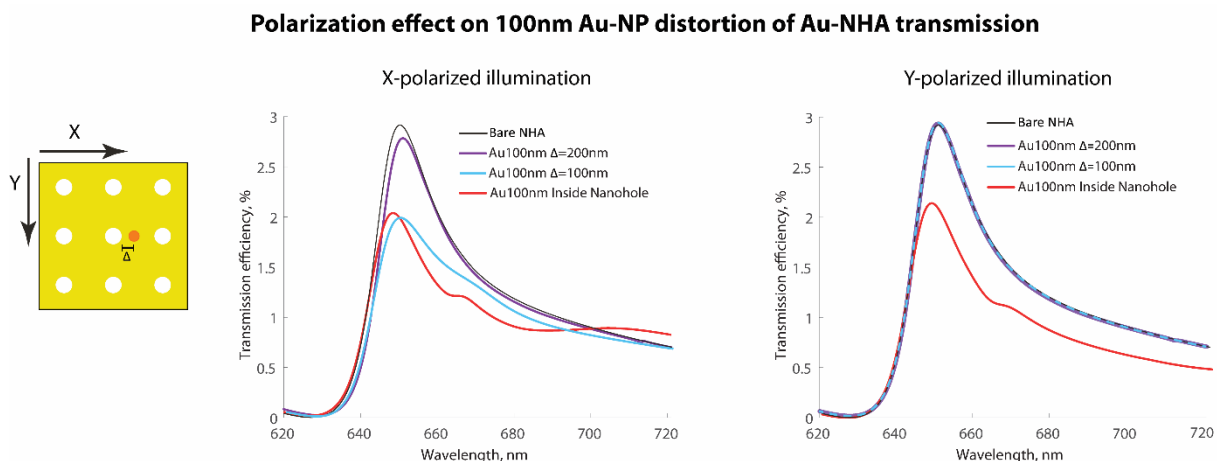


Figure S4.1. Polarization effect on transmission suppression produced by a 100 nm Au NP on Au-NHA transmission. NP bound inside a NH affects localized modes in all directions (X-polarized and Y-polarized). NP that is on the surface close to the NH rim efficiently suppresses transmission of light polarized in one direction (X-polarized), but has no effect in the orthogonal direction.

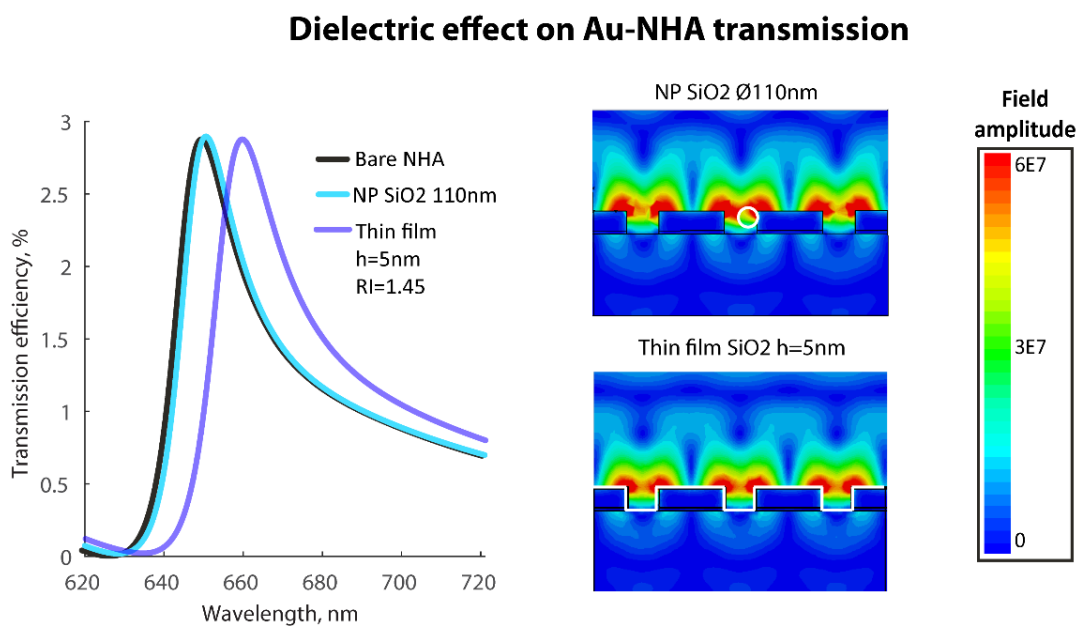


Figure S4.2. Dielectric NP and thin-film effect on Au-NHA transmission. SiO₂ nanoparticle has very little effect on Au-NHA transmission, causing small effective refractive changes, but does not disrupt the formation of localized plasmonic nanohole modes. SiO₂ thin film of 5 nm height causes spectral shift of Au-NHA transmission resonance peak due to refractive index changes.

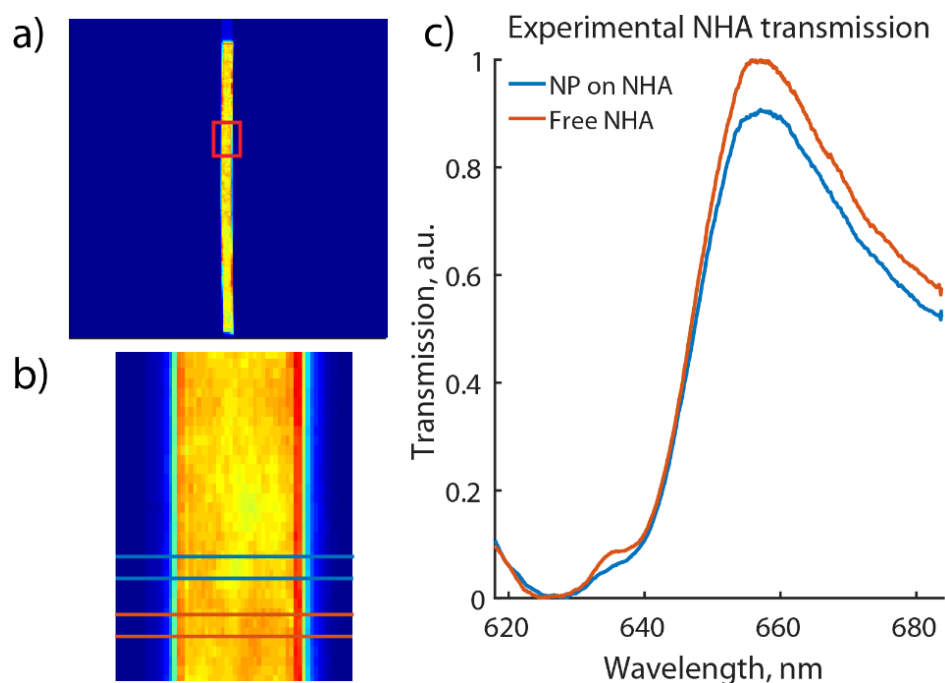


Figure S4.3. Experimental NHA transmission spectra and transmission suppression due to Au-NP binding measured in dry ($RI = 1$) with an imaging spectrometer using 20x magnification. a) Image of a Au-NHA area with Au-NPs acquired through an open slit (slit width = 100 μm). b) Zoom-in of an image area with and without NP. c) Spectral transmission of Au-NHA areas in b) acquired with a closed slit (slit width = 15 μm) over area with NP (blue) and NP-free area (red). In agreement with numerical simulations and imaging results, the binding of NP on NHA decreases the amplitude of EOT peak.

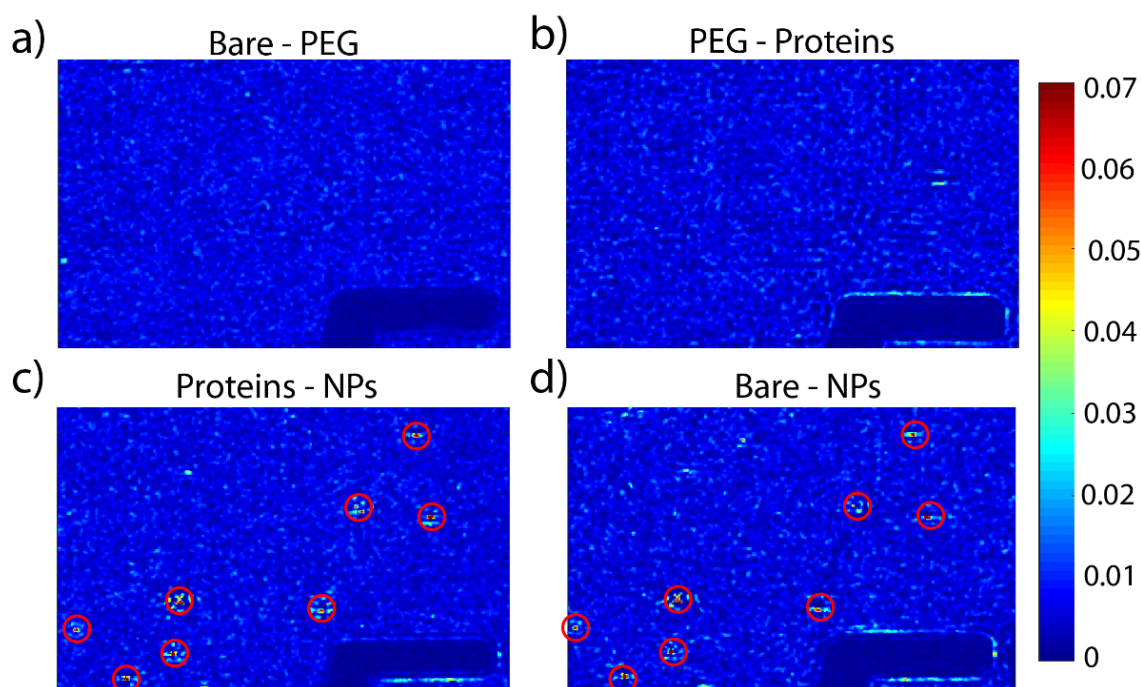
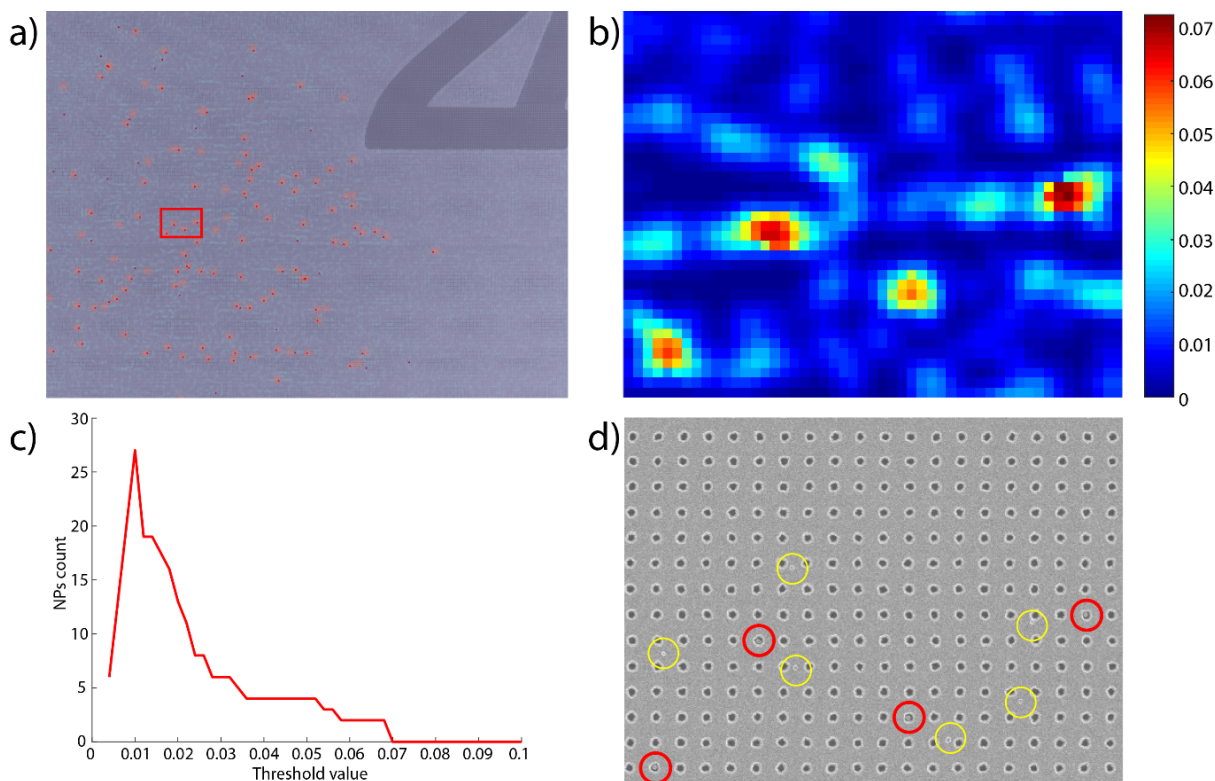


Figure S4.4. Comparison of plasmonic heatmaps corresponding to different stages of bioassay. Plasmonic images were acquired and subtracted at different stages of bioassay to show and compare the effect of biofunctionalization and NPs binding. NPs cause significantly higher contrast changes compared to biomolecules, and can be easily identified irrespective of the stage at which reference images are obtained. Plasmonic spikes identified as NPs are highlighted with red circles. a) Plasmonic heatmap obtained by subtracting image of PEG functionalized NHA from bare Au NHA. b) Heatmap obtained by subtracting NHA covered with Abs and incubated in cell culture media supplemented with 10% serum from image of NHA functionalized with PEG. c) Heatmap obtained by subtracting NHA with bound NPs from NHA with proteins. d) Heatmap obtained by subtracting NHA with bound NPs from bare Au NHA. NPs cause local intensity decrease in transmission, resulting in “bright” spots on plasmonic heatmaps.



large areas of the image have contrast values above 1.5 %, and as a result are recognized by algorithm as few large spikes.

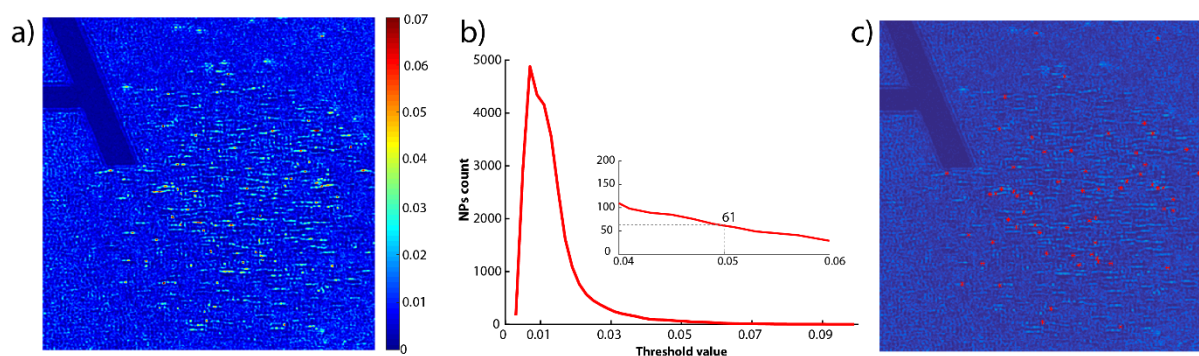


Figure S4.6. Influence of the threshold value for classification of plasmonic spikes on the NPs count over large plasmonic image area. a) Part of plasmonic image showing a single biosensing area with NPs. b) NPs count plotted as a function of threshold value. The slope of NPs count function around 5 % threshold value is small, meaning that NPs count function does not change a lot around the 5 % threshold. c) Plasmonic image with spikes classified as NPs highlighted with red stars.

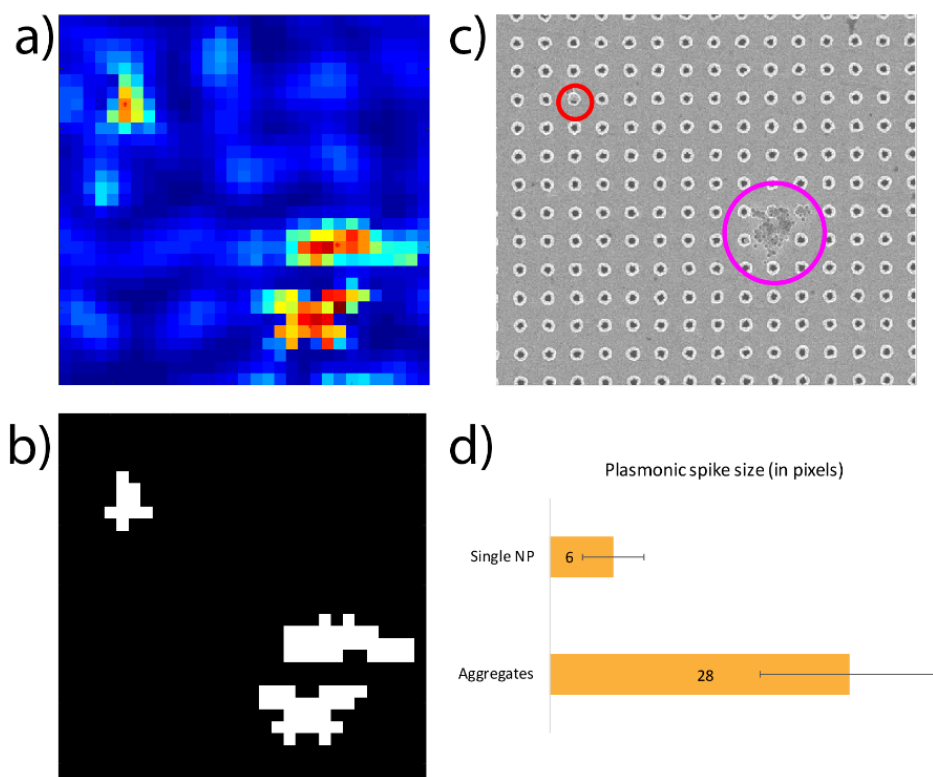


Figure S4.7. Comparison of plasmonic responses from single nanoparticles and sedimenting nanoparticle aggregates. a) Plasmonic image of an area containing a single gold NP and an aggregated NP sediment. b) Identified and isolated plasmonic spikes are shown in white. c) SEM image of identical area as shown in a). Single NP is highlighted by red circle, and NPs aggregate by magenta circle. d) Comparison of an average plasmonic size (in pixels) caused by single NPs (sample size $n = 16$) and size corresponding to NP aggregate (sample size $n = 8$).

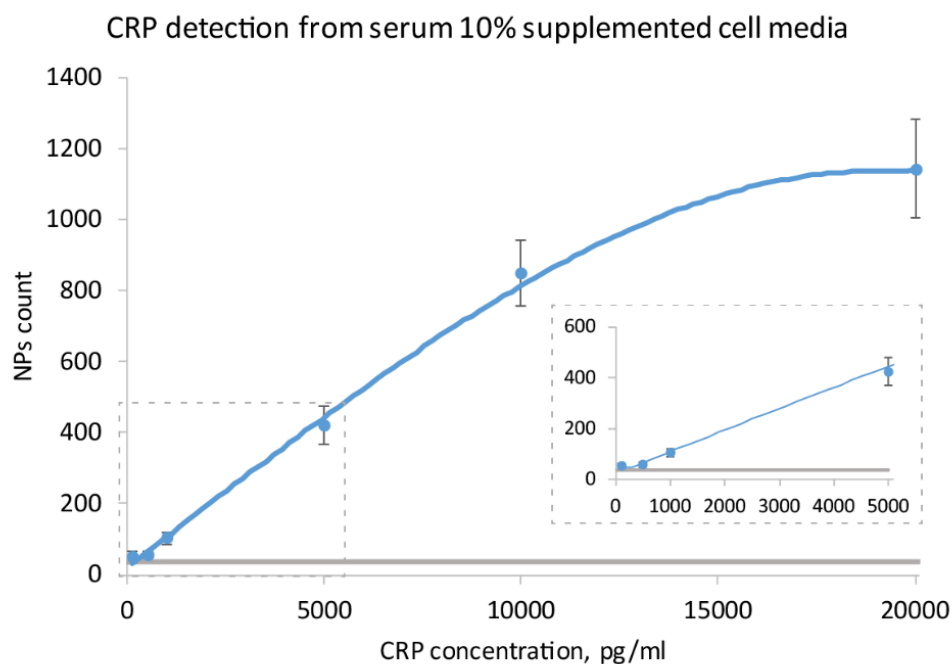


Figure S4.8. Detection of human CRP spiked in supplemented cell culture media with 10% horse serum. We confidently detect down to 100 pg/ml of human CRP with the calculated limit of detection being 69 pg/ml. The linear dynamic region spans from ~500 pg/ml to ~10ng/ml of CRP. The sensitivity is lower compared to 27 pg/ml detection limit from buffer, but is well within clinically relevant values and is comparable with performance of commercial ELISA kits from complex media.

Supporting Video File available at

https://pubs.acs.org/doi/suppl/10.1021/acsnano.8b00519/suppl_file/nn8b00519_si_001.mpg

Figure S4.9. Real-time imaging of 100nm Au-NPs binding in-flow to Au-NHA sensors (100 x 300 μm^2). Two different areas are shown under narrow-band illumination. The illumination is performed at 850nm, which corresponds to the EOT peak of Au-NHAs in aqueous medium (RI=1.33). Au-NHA was functionalized with biotinylated thiols and streptavidin-conjugated NPs were introduced in-flow using a microfluidic PDMS chip assembled over Au-NHA chip. Because the Au-NHA plasmon modes are highly confined at the sensor chip interface, the bulk background during NPs injection does not affect the imaging of surface binding events.

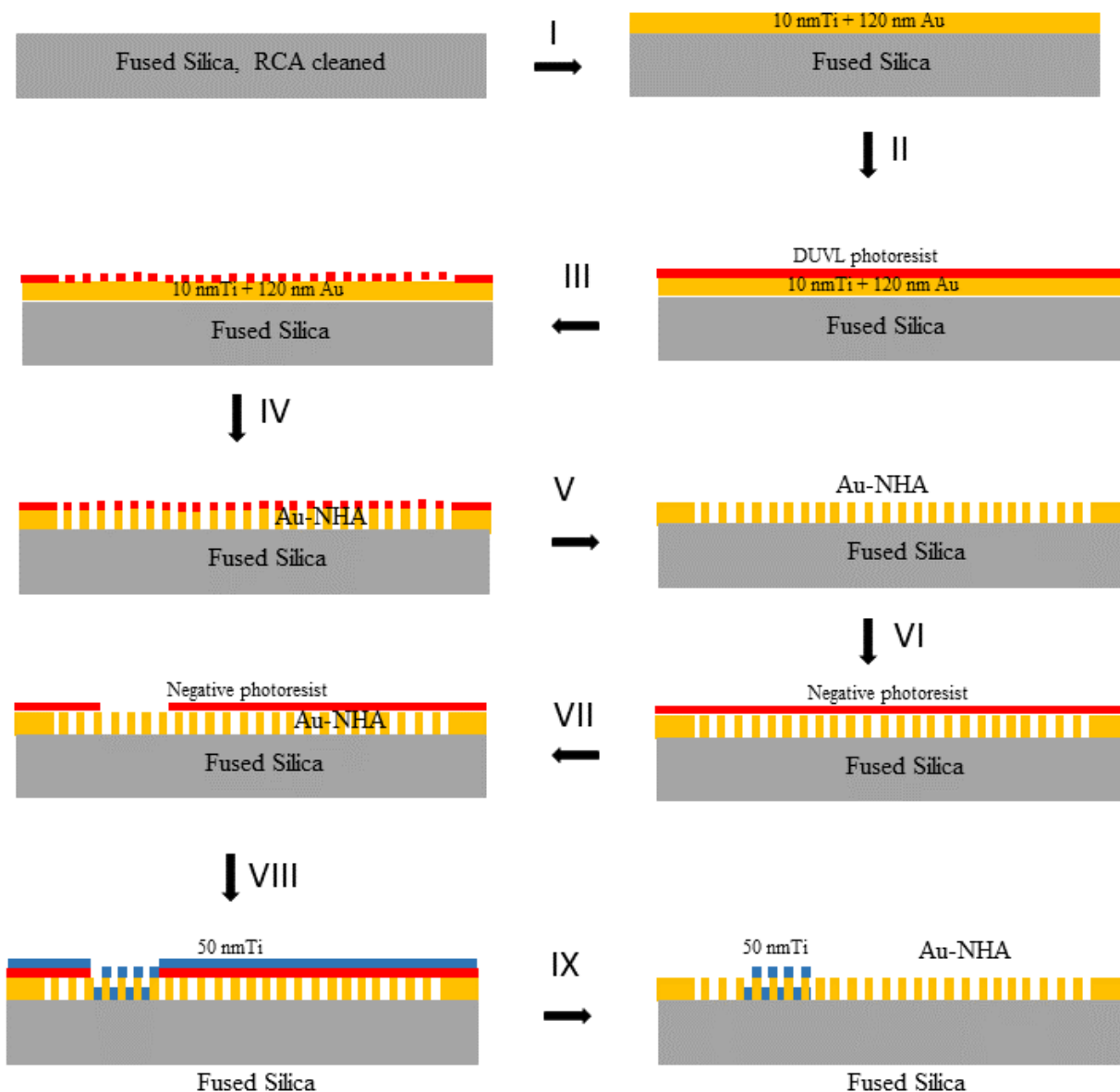


Figure S 4.10 Main fabrication steps of wafer-scale gold nanohole array sensors. The process begins with RCA cleaned fused silica wafers. First, a Ti adhesion layer and Au film are evaporated (I). Next, large-area Au-NHAs are fabricated using DUVL process and ion beam etching (II-V). Then, microarray labels are patterned on Au-NHA sensors by direct laser writing on negative photoresist, and deposition of 50 nm Ti layer (VI-VIII). Finally, photoresist is removed with solvent, microwave stripping, and RCA cleaning (IX) .

Chapter 5

Rapid and Digital Detection of Inflammatory Biomarkers Enabled by a Novel Portable Nanoplasmonic Imager

Alexander Belushkin, Filiz Yesilkoy, Juan Jose González-López, Juan Carlos Ruiz-Rodríguez, Ricard Ferrer, Anna Fàbrega, and Hatice Altug

A. Belushkin, Dr. F. Yesilkoy, Prof. H. Altug

Institute of BioEngineering, École Polytechnique Fédérale de Lausanne, CH-1015, Lausanne, Switzerland, Email: hatice.altug@epfl.ch

Dr. J.J González-López, Dr. A. Fàbrega

Department of Clinical Microbiology, Hospital Universitari Vall d'Hebron, Vall d'Hebron Institut de Recerca, Universitat Autònoma de Barcelona and REIPI, 08035 Barcelona, Spain, Email: anna.fabrega@vhir.org

MD PhD J. C. Ruiz-Rodríguez, Dr. R. Ferrer

Intensive Care Department, Vall d'Hebron University Hospital. Shock, Organ Dysfunction and Resuscitation Research Group, Vall d'Hebron Institut de Recerca, 08035 Barcelona, Spain

Post-print version of the article published in Small (volume 16, issue 3, p1906108):

<https://onlinelibrary.wiley.com/doi/full/10.1002/sml.201906108>

Copyright the Authors. Published by WILEY-VCH Verlag GmbH & Co. KGaA, Weinheim. Reproduced with permission.

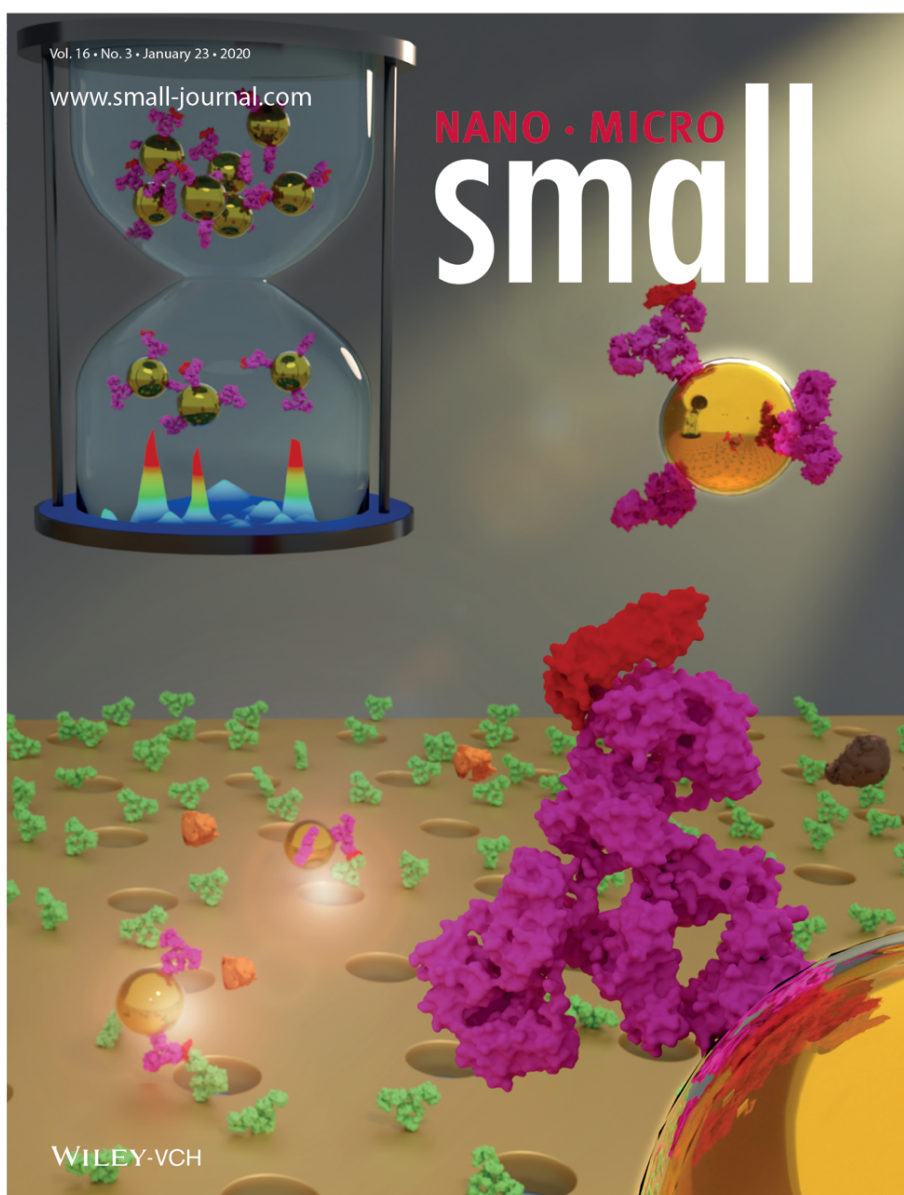
My contribution: Conceiving the study, developing the portable device, designing and conducting experiments, data analysis, and manuscript drafting.

5.1. Abstract

New point-of-care diagnostic devices are urgently needed for rapid and accurate diagnosis, particularly in the management of life-threatening infections and sepsis, where immediate treatment is key. Sepsis is a critical condition caused by systemic response to infection, with chances of survival drastically decreasing every hour. A novel portable biosensor based on nanoparticle-enhanced digital plasmonic imaging is reported for rapid and sensitive detection of two sepsis-related inflammatory biomarkers, procalcitonin (PCT) and C-reactive protein (CRP) directly from blood serum. The device achieves outstanding limit-of-detection of 21.3 pg mL^{-1} for PCT and 36 pg mL^{-1} for CRP, and dynamic range of at least 3 orders of magnitude. The portable device is deployed at Vall d'Hebron University Hospital in Spain, and tested with a wide range of patient samples with sepsis, non-infectious systemic inflammatory response syndrome (SIRS), and healthy subjects. The results are validated against ultimate clinical diagnosis and currently used immunoassays, and show that our device provides accurate and robust performance equivalent to gold-standard laboratory tests. Importantly, the plasmonic imager can enable identification of PCT levels typical of sepsis and SIRS patients in under 15 min. The compact and low-cost device is a promising solution for assisting rapid and accurate on-site sepsis diagnosis.

Keywords:

nanoplasmonics | gold nanoparticles | imaging biosensors | point-of-care diagnostics | sepsis |



5.2. Introduction

Sepsis is a life-threatening condition where the body's own response to an infection progressively leads to organ system dysfunction, failure and finally death [187]. Although the ongoing advancements in modern medicine have increased the survival rates of organ recipients and patients with serious illnesses, such as cancer and HIV, the occurrence of sepsis has been increasing globally, imposing a significant challenge [188]. Moreover, the emergence of drug-resistant pathogens is contributing significantly to the global sepsis threat [189]. Current reports indicate that sepsis causes mortality reaching up to 50% and affects more than 30 million people every year worldwide [188]. In the United States alone, \$24 billion is spent every year for the management of sepsis, making it the most expensive condition to treat [190]. Sepsis progresses extremely rapidly and is considered a medical emergency. In fact, sepsis progresses so fast that every hour of delay in diagnosis and initiating appropriate treatment increases the mortality by 7.6% [191]. Therefore, development of point-of-care devices enabling early and accurate diagnosis of sepsis at different clinical settings is an urgent need as they can allow timely intervention and lower the mortality rate [192]–[194].

However, sepsis diagnosis is not easy, especially in the early stages, or when sepsis presents with an atypical clinical picture. Early stages of sepsis usually present stealth symptoms with significant patient-to-patient heterogeneity, leading to potential delays from the onset of sepsis until the most appropriate treatment starts [195], [196]. The dysregulated host response to infection, which is typically present in sepsis patients, is primarily supported by an inflammatory process, which is termed SIRS, for systemic inflammatory response syndrome. However, it is challenging to discriminate whether the biological insult leading to SIRS is an infectious process or not, an essential criteria for the antimicrobial treatment to be worthy and effective [187]. Traditionally, for the microbiological diagnosis of sepsis, blood-culture based pathogen investigation is performed, which typically takes 4-5 days [195]. The current recommendation is to

administer broad-spectrum antibiotics as soon as possible, ideally in the first hour after sepsis recognition, before a definitive microbiological diagnosis is made based on the pathogen identification tests [197]. This approach leads to overuse of antibiotics, which worsens the global health challenge of antibiotic resistant bacteria development, because neither all SIRS patients have an underlying infectious process, nor all infections are caused by bacterial pathogens. In contrast, a new clinical trend in sepsis management relies on blood testing to monitor patient's systemic response for rapid patient stratification. These tests, which quantify circulating biomarkers, such as the two most universal sepsis-related biomarkers procalcitonin (PCT) and C-reactive protein (CRP), help diagnose sepsis timely and reduce over-prescription of antibiotics. Although these inflammatory biomarkers alone cannot be the sole basis for accurate sepsis diagnosis, their blood levels provide valuable quantitative information to triage patients based on their anomalous response allowing for personalized treatment [198]–[204]. The current gold standard clinical tools to test blood circulating proteins are largely based on complex and lengthy immunoassays, such as enzyme linked immunosorbent, immunoturbidimetric (ITA) and chemiluminescent (CLIA) immunoassays, which require fully equipped clinical laboratories. However, having rapid access to the patient's systemic response, using portable, low-cost, and easy-to-use devices that can rapidly detect biomarkers in a simple manner from small sample volumes can drastically improve sepsis care at different clinical settings such as emergency care units, ambulances, and outpatient health centers.

Currently, active ongoing efforts are being undertaken both in the biomedical industry and basic research to find new diagnostic solutions and develop point-of-care devices to rapidly diagnose sepsis on-site in a cost-effective way. For instance, a compact device proposed by Samsung (LABGEO IB10) operates by detecting PCT with a centrifugal microfluidic disk. Another recent technology that is being investigated by Abionic for sepsis detection combines nano-fluidic channels with centrifugal disk. Although nano-sized channels can improve the sensitivity they are prone to clogging. Moreover, these

technologies employ mechanically moving parts that can compromise device robustness over time. So far, no portable system has received FDA approval for measuring biomarkers that effectively predict sepsis at the point-of-care. Research efforts have been made to develop devices for sepsis biomarkers detection based on optical schemes, including plasmonics and fluorescence. Surface plasmon resonance (SPR) and surface-enhanced Raman scattering (SERS) sensors were reported, however they could not achieve clinically relevant sensitivity [205], [206]. Fluorescent schemes have been implemented to detect sepsis markers, however they either rely on expensive and bulky optical set-ups, such as total internal reflection (TIRF) microscopy [207], or do not meet clinical sensitivity [208], [209]. Promising recent approaches use microfluidic extraction of cells from small amount of patient blood to quantify expression of CD64 biomarker, however they employ sophisticated design and control of microfluidic chip [210], [211]. Alternatively, a sensitive system based on magnetic beads and fluorescent enzymatic amplification has been proposed. The system provides a low limit of detection for measuring a sepsis-related biomarker IL-3 but at the expense of multiple assay steps and 1 hour long detection time [212].

Here, we report a portable digital nanoparticle-enhanced plasmonic imager for rapid detection of inflammatory biomarkers (DENIS). The unique nanoplasmonic imaging mechanism is based on gold nanoparticle (Au-NP) binding to plasmonic gold nanohole array (Au-NHA) [213], which enables quantification of individual molecule binding on the sensor surface in complex media. The bioassay is performed in a single step without signal amplification or washing procedures, and the plasmonic detection is robust against variations in optical properties of samples. Importantly, the imager is made of low-cost off-the-shelf optical components, and its small size enables deployment and operation in on-site clinical settings. Moreover, the sensor chips are produced in a scalable cost-effective manufacturing and the bioassay reagents can be stored stably over weeks. We first show the application of DENIS for highly sensitive, quantitative and robust detection of PCT and CRP biomarkers. The system enables ultra-high

detection sensitivities with limit-of-detection (LOD) down to 21 pg mL^{-1} and 36 pg mL^{-1} for PCT and CRP, respectively, and a wide dynamic range of at least 3 orders of magnitude. We evaluate the performance of DENIS in clinical settings by testing the samples from sepsis, non-infectious SIRS, and healthy subjects provided by Vall d'Hebron Sepsis Bank. We benchmarked our results to the clinically validated assays and the diagnoses of patients and in agreement, we observed that rapid and quantitative detection of PCT and CRP from blood serum of the selected 34 patient cohort assisted in discrimination of healthy and sick groups. Moreover, PCT detection with DENIS show performance equivalent to gold standard clinical assays in non-infectious SIRS and sepsis patients. Finally, DENIS can perform rapid detection by recording video of the plasmonic sensor and analyzing the signals in real time. The time-resolved results revealed that we can identify samples with high (sepsis) and medium (non-infectious SIRS) PCT levels in 5 and 10 min, respectively, reducing the test time to under 15 min.

5.3. Results and Discussion

5.3.1. Detection mechanism

The DENIS detection mechanism is based on a large-area Au-NHA device supporting SPR and localized surface plasmon (LSP) modes [106], [214]–[216]. Au-NHAs exhibit extraordinary optical transmission (EOT) at its resonance wavelength, controlled by the period and geometry of the nanoholes, when illuminated in a collinear optical path [144]. This plasmonic resonance is locally distorted upon the binding of single Au-NPs (100 nm diameter). These distortions result in local suppression in the EOT, which enables detection of single NP-labelled molecules [213]. Although the NPs are subwavelength in size, their plasmonic interaction with the Au-NHA allows for high-contrast imaging of surface-bound NPs in a simple bright field optical reader over large field of view directly inside complex samples. The imaged data is not affected by the

bulk sample background because the resonance transmission through Au-NHAs is strictly dependent on the surface localized field with ~ 100 nm decay length. Moreover, the contrast generated by a single particle is significantly above the noise level induced by the camera and the sample, therefore individual molecules binding can be robustly quantified in a digital way directly in complex media (Figure S5.1, Supporting Information). In contrast, more conventional affinity sensors average the read-out over sensor areas, and require a certain density of analyte binding to reach a sufficient signal to be detected over the system noise, such as background fluctuations or reader noise. The digitized detection of individual particles with DENIS enables highly sensitive quantification of low analyte concentrations at the diffusion limit, and statistical assessment of the signal [213]. Importantly, single NPs can be distinguished on plasmonic images from NPs aggregates and sediment by the size and the shape of the plasmonic image spikes [213].

5.3.2. Plasmonic microarray sensors

We use the detection technique to quantify PCT and CRP biomarkers from human serum samples. In the presence of the biomarker in the sample, antibody-conjugated Au-NPs bind to the Au-NHA surface functionalized with complementary antibodies (Figure 5.1a) and can be detected using a portable reader (Figure 5.1b). Individual Au-NPs bound inside or close to the nanoholes (Figure 5.1c) create strong local intensity contrast (Figure 5.1d), which corresponds to digital detection of single analyte molecules.

To enable microarray based multiplexed biosensing, capture antibodies are bioprinted on the sensor surface using a high-throughput, non-contact, low-volume liquid dispenser as shown in Figure 5.1e. The Au-NHA sensors are manufactured using a low-cost wafer-scale deep UV lithography and ion beam etching (Figure 5.1f). The nanofabrication process enables production of over 50 highly uniformly nanostructured

chips (1 cm x 1 cm) per 4-inch wafer and 8 wafers per batch with negligible variation in optical properties [182]. This robustness in the manufacturing of nanostructured sensors is critical to enable the transfer of the technology to a clinical diagnostic tool. We post-patterned the fabricated chips with an array of Quick Response (QR) codes (Figure 5.1g, Figure S5.2, Supporting Information). In addition to tagging individual chips and microarray locations on the chips, QR codes encode the information about the fabrication batch parameters and the wafer enabling a registry record of the manufactured sensors.

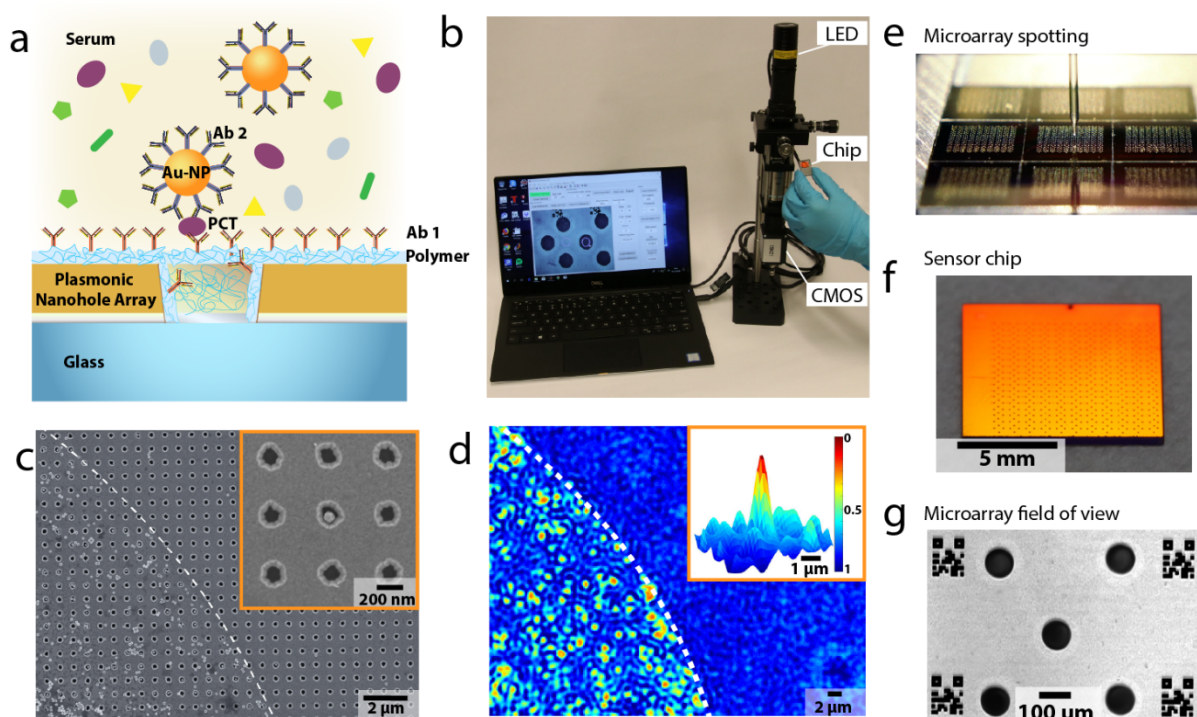


Figure 5.1. Portable digital nanoparticle-enhanced plasmonic imager for biomarkers detection (DENIS). (a) PCT and CRP, which are blood-circulating protein biomarkers secreted by the host body in response to systemic inflammation, are detected using DENIS. A single-step bioassay directly in human serum enables rapid molecular results, critical for the early diagnosis of sepsis, by detecting individual nanoparticles (NPs) binding to gold plasmonic nanohole arrays (Au-NHA). (b) A prototype DENIS reader

developed for highly sensitive and multiplexed detection of biomarkers. The device uses a CMOS camera and a narrow-band LED source to record the transmitted images from a nanoplasmonic chip. (c) SEM image of a Au-NHA area after a bioassay showing the bound NPs. Inset shows a single nanoparticle bound inside a nanohole. (d) Plasmonic image of a Au-NHA area with bound nanoparticles. The binding of Au-NPs on Au-NHAs causes local transmission suppression through distortion of plasmonic excitations in the Au-NHA, and can be digitally detected using far-field imaging. The inset shows a normalized intensity contrast induced by a single nanoparticle trapped in a nanohole. (e) To enable microarray based biosensing, capture antibodies are immobilized on the Au-NHA sensor surface using non-contact ultra-low volume robotic liquid dispenser. The image shows 9 sensor chips with spotted microarrays under dispensing nozzle. (f) Photograph of a Au-NHA plasmonic chip. The sensors are fabricated using wafer-scale DUVL lithography. (g) Image of a plasmonic microarray field of view with antibody spots, and labelled with QR codes.

5.3.3. Portable optical reader

The nanoplasmonic imager is made of off-the-shelf optical components and comprises a narrowband light emitting diode (LED) source, spectrally matching the EOT wavelength of Au-NHAs, a custom-built aluminium holder for the nanoplasmonic chip, an objective, and a CMOS camera. The collimated LED light is transmitted through the sample chamber and modulated by the Au-NHA sensor. The sensor images are acquired by a 50x objective and CMOS sensor with 4104 x 3006 pixels and 3.45 μm pixel size. Each image shows a 900 μm x 700 μm field of view (FOV) with ~ 1.2 μm resolution (Figure 5.1g). The reader weight is below 1 kg and the dimensions are 10 x 10 x 35 cm. Such compactness means it is easily transportable and can be deployed in most on-site settings.

The control of the camera, image acquisition, and data processing are performed on a portable laptop PC using custom Matlab functions. In brief, images are recorded with custom auto-exposure to ensure optimal intensity profile, corrected for source illumination, and the NPs binding is quantified over the sensing spots by computing the percentage of dark pixels using a cut-off threshold. QR tags from the images can be automatically recognized by custom Matlab function to register individual FOVs. For end-point measurements, signals from at least five microarray areas from each sensor chip are recorder for statistical significance. In the case of time-resolved measurements, images of a single FOV are recorded with 30 sec intervals, and the signals are extracted from at least three microarray spots to estimate mean and standard deviation. In order to control for non-specific NPs binding and background fluctuations, in each measurement the signals from BSA blocked background are subtracted from the signals of Ab microarray spots.

5.3.4. Bioassay

Our simple and rapid bioassay is performed in a single-step, where antibody functionalized Au-NP (Ab-NP) suspension is mixed directly with blood serum and then injected into the measurement chamber (Figure 5.2). We prepare large batches of Ab-NPs with optical density OD=20 and store them in Phosphate Buffer Saline (PBS 1X) buffer with Bovine Serum Albumin (1% w/v) and Tween20 (0.05 % w/v). The Ab-NP suspension is stable at 4°C for at least 5 weeks, over which the tests were performed. The sensor chips are first uniformly functionalized with copoly-DMA-MAPS-NAS-fluorinated polymer (MCP-2F), containing activated amine reactive NHS-ester groups, to ensure stable antibody immobilization. Moreover, the fluorocarbon polymer helps prevent non-specific NP binding, and fouling by serum proteins [217]. To form antibody microarrays, we spot antibodies specific to the biomarkers as well as mouse isotype immunoglobulin-G (IgG) for non-specific negative control both at 200 µg mL⁻¹. Each microarray spot of ~150 µm diameter, is formed by a single 400 pL droplet dispensed

with 400 μm period. Importantly, the use of microarray printer not only enables functionalization of large number of chips, but also minimizes the amount of antibodies used, which are one of the most expensive components of the assay. The uniform antibody immobilization on the sensor surface is ensured by adding trehalose (0.5% w/v) and Tween20 (0.01% w/v) in the PBS 1X spotting buffer. The sensor chips with IgG microarrays are blocked with BSA (1% w/v) to minimize the non-specific binding. A capillarity-based disposable microfluidic platform is sealed on the sensor chips using a silicone spacer [120]. The antibody immobilized chips can be stored at 4⁰C stably for at least 5 weeks (Figure S5.6, Supporting Information). To increase the performance of our assay, we optimized a stabilizing buffer, which consists of PBST (1X, 0.05% w/v) and NaOH (50 mM) in 3:1 ratio. To perform the bioassay, 20 μL of serum is mixed with 4 μL of Ab-NP suspension and 16 μL of stabilizing buffer, and the mixture is loaded into the measurement chamber with a pipet. The loaded cartridge is either inserted into the reader for time-resolved data acquisition or measured after an incubation period.

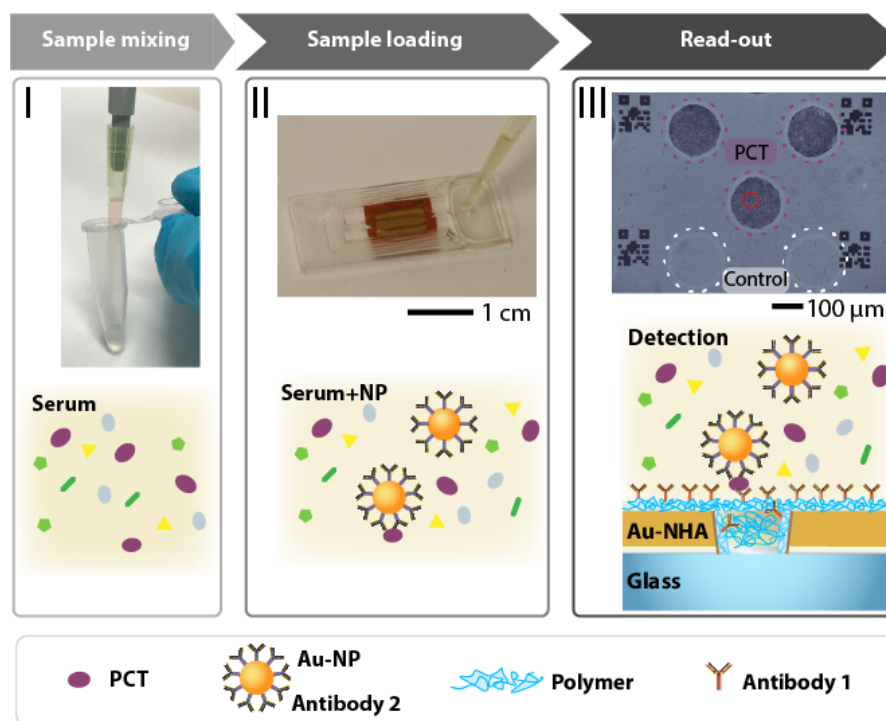


Figure 5.2. Detection and quantification of PCT and CRP using DENIS. A serum sample (I) is mixed with Au-NPs functionalized with antibodies against PCT or CRP (Ab-NPs). Ab-NPs bind to the antigen in serum (II). Sample with Ab-NPs is injected on Au-NHA sensor chip functionalized with polymer and spots of complementary aPCT or aCRP antibodies as well as non-specific mouse IgG as negative control. Ab-NPs bind on the Au-NHA chip functionalized with complementary antibody spots in a sandwich assay in the presence of the antigen (III).

To characterize the performance of DENIS system, calibration titration curves were obtained by spiking known amounts of PCT and CRP biomarkers in reference samples (Figure 5.3). Each data point represents mean value and standard deviation from five measurements collected from different microarray areas. The LOD values were estimated by measuring the mean signal from blank samples and adding three times the standard deviation. Our detection method achieves LOD of 21 pg mL^{-1} and 36 pg mL^{-1} for PCT and CRP, respectively. Moreover, the PCT detection dynamic range of DENIS

is three orders of magnitude (i.e. from ~ 21 to $>10^4$ pg mL^{-1}). The clinical serum levels of PCT usually range from tens of pg mL^{-1} for healthy individuals to few hundreds pg mL^{-1} for SIRS patients free of bacterial infection, and above ~ 1 ng mL^{-1} in sepsis patients [218]. Therefore, our method covers the full relevant diagnostic range. The clinical serum levels for CRP range from few $\mu\text{g mL}^{-1}$ for healthy individuals to hundreds $\mu\text{g mL}^{-1}$ for septic patients [218], which are significantly higher than the values for PCT. To measure them with the same assay, we diluted serum for CRP measurements in order to comply with the dynamic range of the device, which covers from 36 to 10^5 pg mL^{-1} . Importantly, the sensitivity and dynamic range enabled by DENIS are similar to the performance of gold standard lab techniques, without the need for time-consuming amplification and washing steps or bulky readout equipment.

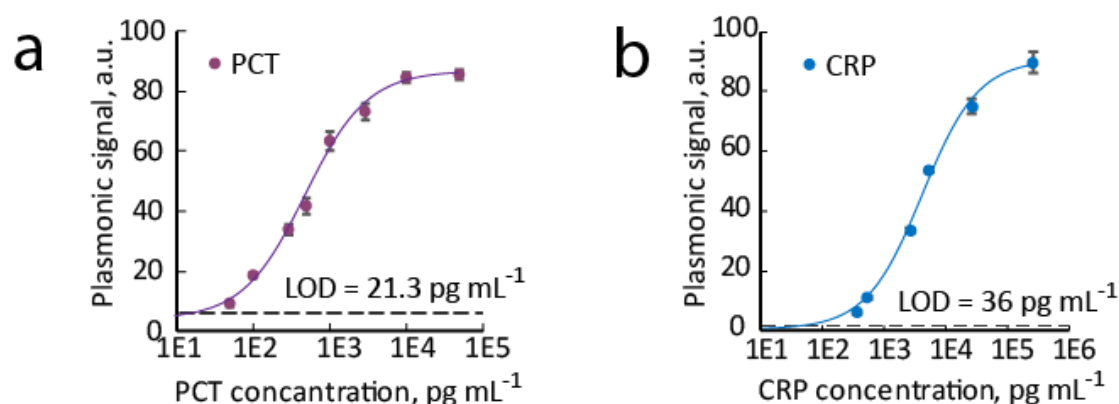


Figure 5.3. Determining the detection sensitivity for PCT and CRP biomarkers with the DENIS system. The calibration curves were obtained by titrating a known concentration of (a) PCT or (b) CRP and measuring the associated signal.

5.3.5. Clinical tests of the DENIS system

We deployed the DENIS system at the Vall d'Hebron University Hospital and tested with clinical samples previously collected from patients with sepsis, non-infectious SIRS and healthy individuals (previous informed consent agreement). Even though the

new sepsis definitions prefer to avoid the term SIRS, this clinical condition is still worthy when defining the appropriate study groups with research purposes [187]. We obtained and measured on the DENIS platform samples, previously anonymized, from 34 individuals, including 18 patients with sepsis, 11 with non-infectious SIRS, and 5 healthy donors (Table S5.1, Supporting Information). The detection of PCT and CRP levels in the patients serum was performed as described above using only 20 μ l of sample for each measurement. The measurements were done in a blind manner, where neither the patient status nor the biomarker concentrations were disclosed during the testing in order to eliminate bias. After the completion of the clinical tests, the results collected from DENIS assay were compared with the routine clinical determinations. Specifically, CRP and PCT detection were performed using ITA and CLIA, respectively, and bacterial infection was determined with blood culture. The example images of single PCT spots obtained by DENIS system directly in serum from the three patient groups are presented in Figure 5.4a.

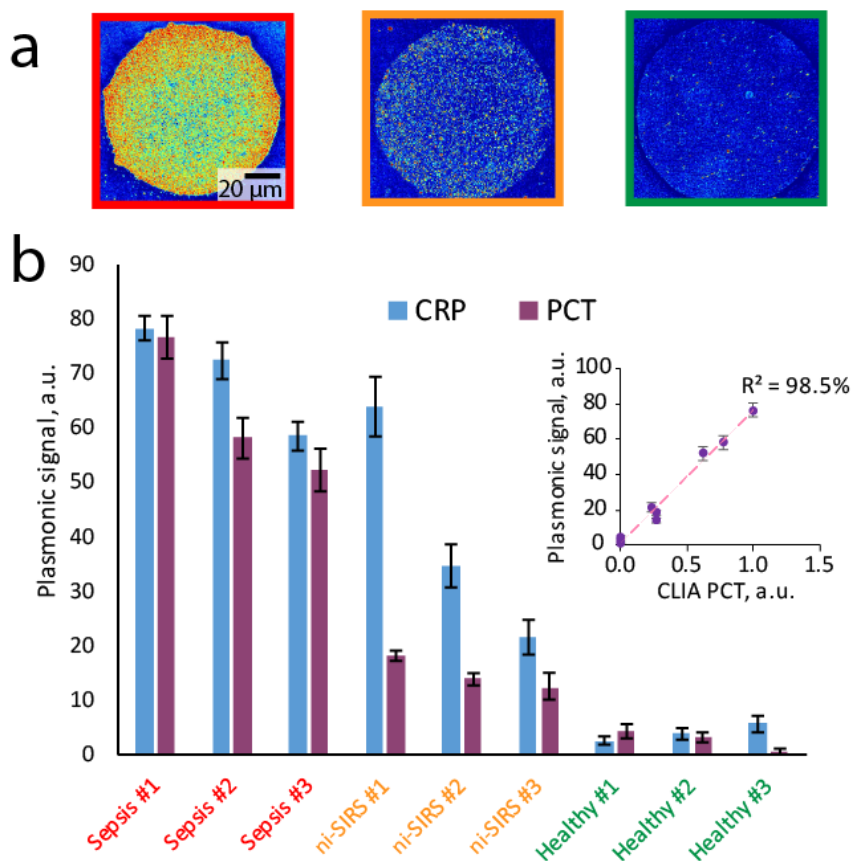


Figure 5.4. (a) Different concentration of PCT in serum results in different density of particle binding. From left to right: representative microspots imaged from clinical samples associated to a sepsis patient, a non-infectious SIRS patient, and a healthy donor are shown. (b) Quantification of PCT and CRP biomarkers using DENIS in the serum of typical representative patients with sepsis, non-infectious SIRS and healthy controls. Error bars represent standard deviation between signals of five spots measured for each sample. Inset shows correlation between DENIS and CLIA measurements of PCT levels for the typical patients.

Samples from septic patients contain high levels of PCT or CRP, and result in dense binding of particles on antibody microspots of the Au-NHA sensor, while non-infectious SIRS samples produce images with sparsely bound NPs, and healthy samples

present negligible NP binding on the sensing areas. Figure 5.4b shows CRP and PCT values measured from nine representative individuals from the three groups. Each data point represents the mean and STD from at least 5 different spots. We observed consistent results correlating the PCT readouts from DENIS to the CLIA measurements in the clinical lab (inset Figure 5.4b). In every sample measured, we controlled for non-specific interactions between Ab-NPs and the Au-NHA surface by recording signals from mouse IgG spots and BSA blocked areas (Figure 5.5). Notably, we observed no significant signals from these control measurements on every chip tested, therefore no washing steps were needed.

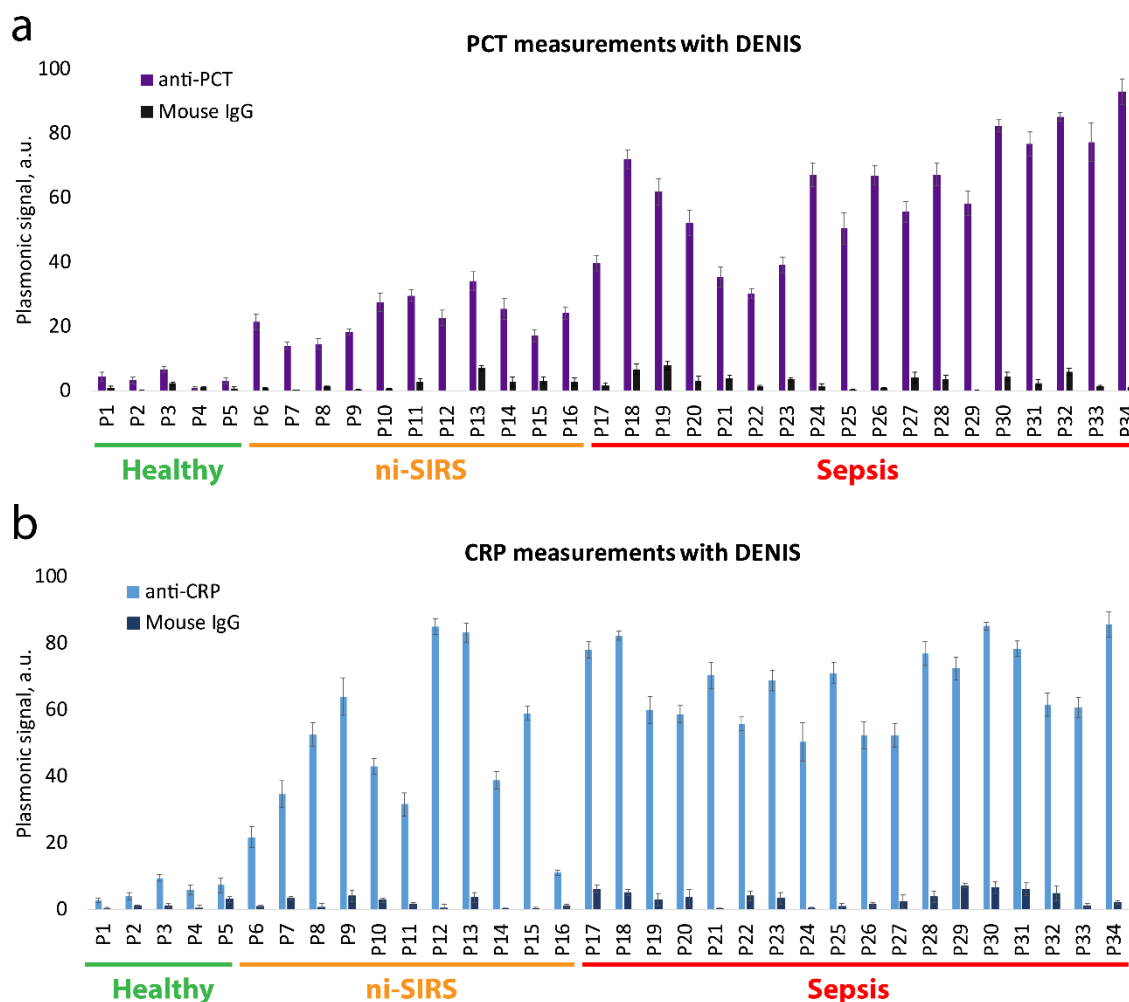


Figure 5.5. Quantification of plasmonic imaging signals for (a) PCT and (b) CRP, as well as from non-specific mouse isotype control antibody spots, for every patient. The two biomarkers were measured for 34 subjects, including 18 sepsis patients, 11 non-infectious SIRS (ni-SIRS) patients, and 5 healthy controls. The signal from mouse antibodies was small for all patients, indicating little non-specific interactions between Ab-NPs and Au-NHA sensor. Signals plotted as difference between signal from Ab spots and BSA background. For each point, at least five different antibody spots were measured to estimate the mean and the standard deviation of the signal.

To validate the performance of the DENIS platform, we mapped the PCT and CRP detection results of 34 individuals to the measurements with CLIA and ITA, based on the clinical diagnosis (see Figure 5.6a,b and Figure S5.3, Supporting Information). In the sampled group, the measured levels of PCT and CRP using both DENIS and clinical assays were significantly elevated in non-infectious SIRS group compared to healthy subjects ($P_{\text{PCT DENIS}} < 1.7\text{E-}5$, $P_{\text{CRP DENIS}} < 1.7\text{E-}3$, unpaired t-test), and in sepsis group compared to non-infectious SIRS ($P_{\text{PCT DENIS}} < 2.3\text{E-}7$, $P_{\text{CRP DENIS}} < 4.9\text{E-}3$, unpaired t-test). However, CRP was reported in multiple sources to be a general inflammatory marker that is not well discriminative of the stage or the source of inflammatory host response [218], [219]. Therefore, in order to compare the performance of DENIS to clinically validated assays in assisting the discrimination between sepsis, non-infectious SIRS, and healthy groups, we constructed receiver operating characteristic (ROC) curves using PCT measurements with both techniques as a predictor (Figure 5.6c,d). We also calculated the corresponding area under the curve (AUC). ROC curves are an established metric to analyse diagnostic ability of a test to discriminate the true state of subjects, and to compare two alternative diagnostic tests when each is performed on the same subject [220]. DENIS measurements of PCT provided equivalent performance to CLIA in discriminating between the three patient groups. With both methods, we observed 100 % sensitivity and specificity in classifying between healthy and sick subjects, moreover PCT was a good indicator of host response in sepsis compared to non-infectious SIRS, with $\text{AUC}=0.995$, Sensitivity = 0.944, and Specificity = 1. Although the patient cohort of 34 subjects is not large enough to reflect the general population statistics, these findings are in agreement with the literature, where PCT levels in blood were shown to be a useful indicator to assist in discrimination of non-infectious SIRS from sepsis patients [218], [219]. Importantly, the results of the DENIS assay showed robust performance, even though the patients serum samples presented significant visual differences in the color and consistency (Figure S5.4, Supporting Information).

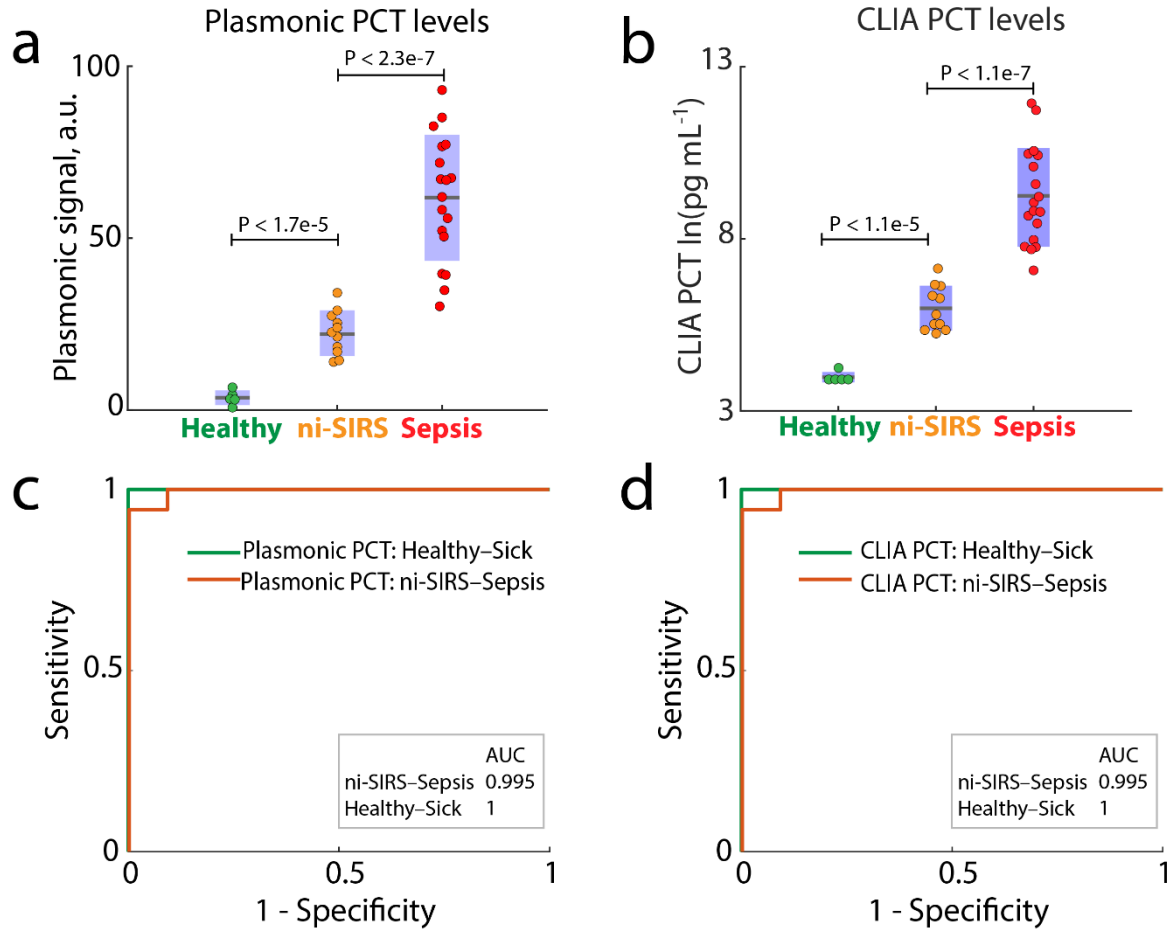


Figure 5.6. PCT measurements using DENIS to assist diagnosis. Samples from 34 clinically diagnosed individuals, including 18 sepsis patients, 11 non-infectious SIRS patients, and 5 healthy controls, were tested. Box and whiskers plot with scattered data points for sepsis, non-infectious SIRS and healthy samples are shown for (a) plasmonic DENIS and (b) clinical CLIA measurements. Each data point represents an individual patient. PCT serum levels were significantly higher for non-infectious SIRS group compared to healthy ($P < 1.7e-5$ and $P < 1.1e-5$ with DENIS and CLIA, respectively), and for sepsis compared to non-infectious SIRS group ($P < 2.3e-7$ and $P < 1.1e-7$ with DENIS and CLIA, respectively). Receiver-operation characteristic curves were

constructed for PCT measurements with DENIS (c) and CLIA (d). The performance of DENIS was equivalent to CLIA. For both methods, AUC is 1 to discriminate healthy from sick patients. PCT levels also provided good classification between non-infectious SIRS and sepsis patients, with AUC= 0.995, Sensitivity = 0.944, and Specificity = 1 for both methods.

5.3.6. Rapid biomarker detection.

Rapid turnaround time is an essential characteristic of a sepsis diagnostic device, as sepsis is a time-dependent emergency with a severe disease progression within hours. We show the diagnostic use of DENIS with minimal time-to-result enabled by time-resolved measurements. The system can record real-time video of the sensor (Figure S5.5, Supporting Information), from which NP binding signals are extracted and analysed in real-time. In Figure 5.7, we present time resolved PCT detection signals from sera of representative sepsis patients, non-infectious SIRS patients, and healthy individuals. Each plot shows mean signal from three PCT sensing spots and its 95% confidence interval in the shaded area. To establish the background signal and its variation, we plot averaged signal from three BSA blocked areas and compute the running time averaged 95% confidence interval. We consider a reliable detection when the PCT signal's 95% lower confidence interval exceeds the background's upper confidence interval. We characterized PCT cut-off detection times for high (sepsis), medium (non-infectious SIRS) and low (healthy) PCT concentration groups and observed that we detect sepsis levels in less than 5 min and non-infectious SIRS levels in around 10 min, while PCT signal from healthy individuals did not significantly exceed background over 2 h. These results show that PCT detection can be performed in under 15 min, including sample mixing, injection and read-out, which is particularly important in intensive care units.

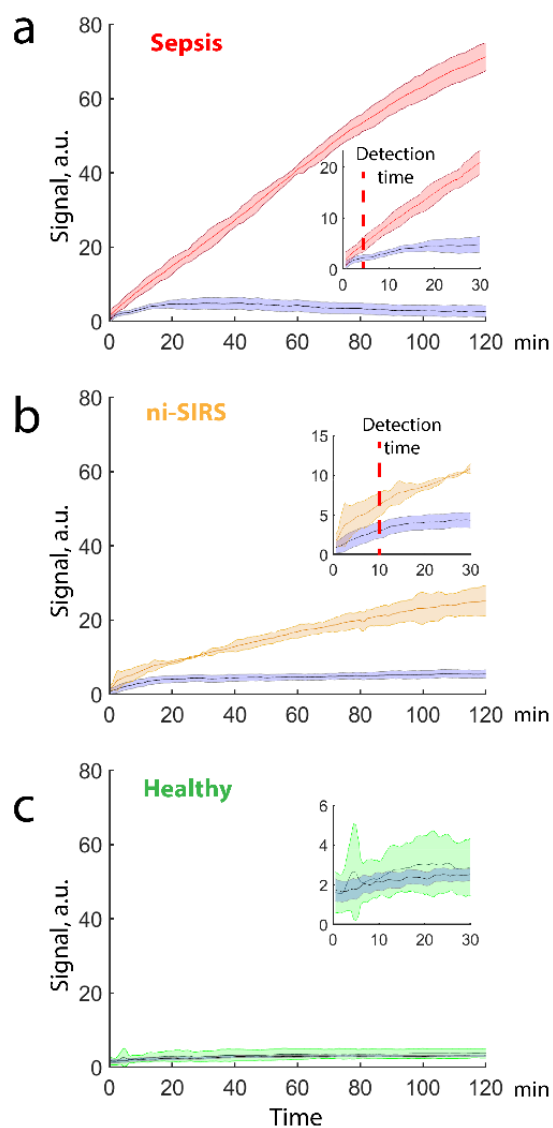


Figure 5.7. Time resolved PCT detection using DENIS. Real-time measurements of selected subjects: (a) high PCT content (sepsis patient, $[PCT] = 24.26 \text{ ng mL}^{-1}$), (b) medium PCT content (non-infectious SIRS patient, $[PCT] = 0.79 \text{ ng mL}^{-1}$) and (c) low PCT content (healthy control subject, $[PCT] < 50 \text{ pg mL}^{-1}$). Error bars from the PCT signal represent 95% confidence interval extracted from data collected from three different aPCT antibody microspots from a single image frame. The background signals are collected from three off-the spot BSA blocked areas. The blue shaded intervals

indicate dynamic time averaged 95% confidence interval for background signal. Insets show the first 30 min time period. The detection time is defined as the cut-off point when the PCT signal's 95% lower confidence interval exceeds the background's upper confidence interval. The detection time is estimated to be less than 5 min for sepsis and 10 min for non-infectious SIRS.

5.3.7. Discussion

DENIS device proved to be particularly suitable for on-site operation due to its portability, inexpensive off-the-shelf optical components, and because it does not involve any moving parts or complex microfluidic elements prone to clogging. Importantly, the sensor chips and bioassay reagents can be stored in the fridge stably over weeks and unlike previously reported optical detection schemes [207]–[209] do not require fluorescent tags that can be expensive, unstable, and difficult to produce. The simple and rapid bioassay enables highly sensitive and robust detection of PCT and CRP, covering the full clinically relevant ranges. The high sensitivity of the assay is enabled by the unique plasmonic mechanism that works by detecting individual molecules on the Au-NHA surface through imaging of single Au-NPs, without the need for complex signal amplification procedures. The system achieved 21.3 pg mL⁻¹ LOD sensitivity for PCT and 36 pg mL⁻¹ LOD for CRP, and a dynamic range of at least 3 orders of magnitude, which is well within the clinical biomarker levels.

DENIS was validated with measurements of PCT and CRP biomarkers from sera of 34 individuals, including 18 sepsis patients, 11 non-infectious SIRS patients, and 5 healthy controls, and was shown to provide consistent and robust performance at the level of gold-standard immunoassays. Both PCT and CRP levels were significantly elevated in the sick groups compared to healthy subjects. In the sampled group DENIS measurements of PCT levels showed performance equivalent to clinically validated assay in assisting classification between sepsis and non-infectious SIRS patients, with

94.4% Sensitivity and 100% Specificity. These results show that DENIS platform can be effectively deployed to help rapidly triage patients between non-infectious SIRS and sepsis groups. The detection is robust against background noise, nonspecific adsorption of proteins, and variations in optical properties of the serum, enabling reliable detection. In combination with small sample volume used (20 μ l), this makes DENIS suitable for frequent biomarker testing, such as required during treatment response monitoring.

The sensor chips were fabricated in a robust wafer-scale cost-effective process using DUVL lithography. The functionalization of sensors was performed in a scalable way with microarray bioprinter that uses minimal amounts of antibodies. In combination with easy-to-use bioassay and a compact optical reader, this makes the DENIS technology suitable for the development of a clinical diagnostic device. Owing to the high sensitivity, rapid time-to-result, compactness and cost-efficiency, DENIS is expected to be employed in hospitals as well as small clinic and physician's office settings, where the access to large and costly laboratory testing equipment is limited, therefore assisting timely diagnosis and reducing antibiotic prescription.

We envision several ways in which the current DENIS system could be improved. First, the imaging read-out enables scaling up the test for multiplexed measurements [221]. Sepsis manifests in a complex system of pathophysiological responses, spanning multiple organs. Creating a sepsis marker panel and expanding DENIS to multiplexed detection of relevant biomarkers with comparable dynamic ranges, such as presepsin, MR-pro-adrenomedullin (proADM), pancreatic stone protein (PSP), and interleukin 6 (IL-6) from no more than few μ l of sample could provide more robust characterization of the patient's host response and potentially predict survival [199], [211], [222], [223]. Importantly, the detection principle is not limited to proteins and can be extended to small peptides, DNA, or RNA, as long as a pair of complementary recognition elements is available. The development of the bioassay to operate with whole blood would deliver even faster time-to-result by eliminating serum extraction step and better position the test for the use in resource-limited settings. Further reducing the costs of the imager and

scaling up the production of Au-NHA sensors would push the per-test costs even lower and open the path to potential market entry. Finally, the development of a fully integrated easy-to-use software interface will facilitate introduction of the device to clinical professionals and help validate the technology on large sets of clinical samples.

5.4. Conclusion

Our study reports a portable digital nanoparticle-enhanced plasmonic imager that enables rapid detection of two inflammatory sepsis-related biomarkers, PCT and CRP. The unique nanoplasmonic mechanism through imaging of single Au-NPs binding on the Au-NHAs enables highly sensitive and rapid biomarker detection directly in blood serum. The compact nanoplasmonic reader, built of inexpensive components, weighs less than 1 kg. The portable device was deployed in hospital settings, where it was shown to provide equivalent performance to gold-standard laboratory assays using a wide range of samples from patients with sepsis, non-infectious SIRS, and healthy donors. Moreover, identification of PCT levels typical for sepsis, SIRS, and healthy subjects can be performed in under 15 min, which is significantly faster than laboratory immunoassays. Therefore, DENIS platform promises to become a powerful tool in managing acute inflammatory conditions at the point-of-care in an affordable way, improving the quality of health care for more people.

5.5. Experimental Methods

5.5.1. Au-NHA sensor fabrication:

Plasmonic gold nanohole arrays (Au-NHAs) were produced using wafer-scale low-cost deep-UV lithography (DUVL) process and ion beam etching. Fused silica wafers with

4 in. diameter were used as substrate. The wafers were cleaned with RCA solution (1:1:5 H₂O₂:NH₄OH:H₂O by volume) for 15 min, rinsed with deionized water for 5 min, and dried under nitrogen stream. Next, the cleaned wafers were coated with 10 nm of titanium (Ti) and 120 nm of gold (Au) using Alliance-Concept EVA 760 electron-gun evaporator. The NHAs with 200 nm diameter and 600 nm period were patterned over whole wafers using a 248 nm deep-UV stepper (ASML PAS 5500/300 DUV). The exposed wafers were treated with ion-beam etching (Oxford Instruments PlasmaLab 300 IBE), to transfer the nanohole arrays into metal films. The photoresist was stripped using oxygen plasma.

To label the Au-NHA sensors, QR codes were formed with 50 nm Ti film. The NHA wafers were coated with 1.3 μ m thick lift-off positive photoresist (AZ1512) using Süss ACS200 Gen3 coater, and the QR microarray patterns were exposed using Heidelberg Instruments MLA150 Maskless Aligner. The resist was developed, and 50 nm Ti film was evaporated using an electron gun evaporator. Wafers covered with photoresists and Ti were diced into 1 x 1 cm² sensor chips, and the photoresist was removed from chips by immersing in resist remover with sonication at 70 °C overnight. The final chip cleaning was performed with oxygen plasma for 5 min at 500 W and 1 min immersion in RCA solution (1:1:5 H₂O₂:NH₄OH:H₂O) to ensure uniformly clean Au surface.

5.5.2. Chemicals and Biologicals:

Ammonium hydroxide solution (ACS reagent, 28–30%), hydrogen peroxide (H₂O₂ 30%), bovine serum albumin (BSA) lyophilized, phosphate buffered saline (PBS), Tween20, and D-(+)-Trehalose dihydrate were purchased from Sigma-Aldrich. MCP-2F (copoly-DMA-MAPS-NAS-fluorinated) polymer was bought from Lucidant. Ethanol (EtOH) absolute was from Thermo Chemicals. Pierce protease inhibitor (PI) tablets, recombinant human PCT and anti-PCT (aPCT) monoclonal antibodies QNO5 and CALC, used for spotting on Au-NHA and NP conjugation, respectively, were

provided by ThermoFisher (BRAHMS). Anti human C-reactive protein (aCRP) monoclonal IgG antibodies PCR-196 and PCR-183, used as capture and recognition antibodies, respectively, were provided by DIESSE Diagnostica Senese. Au-NP conjugation kit with lyophilised spherical Au-NPs of 100 nm diameter coated with PEG (10 kDa) and activated with EDC-NHS, were purchased from Cytodiagnostics.

5.5.3. Au-NHA functionalization:

Au-NHA chips were coated with MCP-2F (copoly-DMA-MAPS-NAS-fluorinated) polymer (Lucidant) to yield stable and reproducible functionalization with Ab microarray spots and prevent the sensors from non-specific fouling by serum and NPs. The polymer contains activated NHS-ester groups that enable covalent immobilization of molecules through amino groups. The MCP-2F polymer stock was diluted with coating solution from Lucidant, and the Au-NHA chips were immersed in the solution for 30 min at room temperature. Next, the Au-NHA sensors were washed in large volumes of mQ water and dried under nitrogen stream. The sensors were placed in a vacuum oven at 80 °C for 15 min (< 2 mm Hg) to dry the polymer and ensure stable adhesion to the Au surface. Polymer-functionalized chips were immediately spotted with Ab microarrays, because NHS-ester groups of the polymer degrade in the presence of air humidity.

The Ab microarrays were formed on the sensors by spotting Ab solutions on polymer coated Au-NHA surface using non-contact piezoelectric ultra-low volume dispensing system (sciFLEXARRAYER S3, Scienion). Spotting solutions containing Ab specific against PCT, or CRP, or mouse isotype control IgG, all at 200 $\mu\text{g mL}^{-1}$ were prepared in PBS 1x with Trehalose (0.5% w/v) and Tween20 (0.01% w/v), to ensure uniform Ab distribution over each spot and stabilize Abs during sensor storage. Microarray spots of 400 pl were dispensed with a period of 400 μm inside a humid chamber. The humidity control was set at dew point (65% relative humidity) to prevent evaporation. The sensor

chips with IgG microarrays were blocked with BSA (1% w/v) to inactivate non-reacted EDC-NHS groups and minimize the non-specific binding. The sensor chips were stored until use at 4°C for up to 4 weeks.

5.5.4. Au-NP functionalization:

Au-NPs of 100 nm diameter coated with 10 kDa PEG and activated with EDC-NHS were functionalized with aPCT or aCRP antibodies according to the following protocol. Antibodies were diluted in protein re-suspension buffer (Cytodiagnostics) to 500 µg mL⁻¹ concentration. The antibody solution (40 µl) was mixed with reaction buffer (50 µl, Cytodiagnostics), and added to the vial of lyophilized Au-NPs. The Au-NP mixture with Abs was incubated at room temperature for 4 h with a mild mixing using Eppendorf ThermoMixer at 700 rpm. After incubation, 10 µl of quencher solution (Cytodiagnostics) was added to stop the reaction. The Au-NPs suspension was centrifuged at 150 rcf for 30 min to wash the NPs from non-reacted Abs. The supernatant was removed and NPs were resuspended in 1 mL of PBS 1x with 1% w/v BSA and 0.05% w/v Tween20. Centrifugation and resuspension steps were repeated 3 times. At the final resuspension step, Au-NPs pellet was diluted in a 100 µl of PBS 1x with 1% w/v BSA and 0.05% w/v Tween20 to obtain Au-NP stock solution with optical density OD=20 (measured at 572 nm), or 7.7E+10 NP mL⁻¹. The Ab-NPs solution was stored at 4°C for up to 4 weeks. Before performing bioassay, Ab-NPs were vortexed at 800 rpm for 30 seconds to resuspend the NPs.

5.5.5. Biobank samples:

Samples and data from the patients used in this study were provided by the Sepsis Bank of Vall d'Hebron University Hospital Biobank (PT17/0015/0047), integrated in the Spanish National Biobanks Network. Samples were processed following standard operating procedures with the appropriate approval of the Clinical Research Ethics

Committee (approval reference number PR(AG)11/2016). Sample selection was done to ensure a wide range of concentrations to be measured with DENIS, from low PCT and CRP values associated with healthy individuals, to medium levels usually observed in non-infectious SIRS patients and increasing values that are characteristic of sepsis and septic shock patients. It should be noted that sepsis is a complex syndrome and patient groups could have overlapping biomarker levels. For each patient the samples were collected at a single time-point. For sepsis patients samples were collected at the time sepsis was diagnosed. For non-infectious SIRS patients, samples were collected in the immediate postoperative period. The samples were stored in 500 μ l aliquots at -80°C in cryovials. Samples were handled on ice and protected from light.

5.5.6. Serum bioassays:

The bioassays were performed by mixing patient serum with the Ab-NP conjugates (aPCT or aCRP) and a stabilizing buffer and injecting the mixture into the sensor measurement chamber. A 20 μ l aliquot of serum sample was mixed with 16 μ l of buffer and 4 μ l of aPCT Ab-NP stock by gentle pipetting and inserted onto the measurement chamber. In the case of CRP measurements, the patient serum was first diluted in PBS 1 x with bovine serum albumin 7%. The serum dilution was done in 2 steps, first 100 times and then 500 times, to minimize the error, reaching the final dilution of 50'000 times. Then a 20 μ l aliquot of the diluted serum was mixed with 16 μ l of measurement buffer and 4 μ l of anti-CRP Ab-NPs by gentle pipetting and inserted to the sensor chamber. Sensor chamber was formed by placing a capillarity-based disposable microfluidic cartridge (Microtec) on the Au-NHA sensor chip using a silicone spacer for sealing. The loaded sensor was either immediately inserted into the portable reader for real-time measurements or incubated at room temperature, and end-point read-outs were taken at the end of the incubation period (2 h).

The stabilizing buffer was optimized to ensure optimal bioassay performance and prevent NPs aggregation during the measurements. The buffer consists of 0.05% PBST 1x and 50 mM NaOH mixed in 3:1 volume ratio.

5.5.7. Calibration measurements:

In order to perform calibration measurements of the PCT bioassay, known concentrations of recombinant human PCT (50 pg mL⁻¹, 100 pg mL⁻¹, 300 pg mL⁻¹, 500 pg mL⁻¹, 1 ng mL⁻¹, 3 ng mL⁻¹, 10 ng mL⁻¹, and 50 ng mL⁻¹) were spiked in 7% BSA PBS 1x with protease inhibitors (1 tablet per 50 mL of buffer). Next, the calibration samples, as well as a blank negative control containing BSA 7% in PBS 1x and PI without PCT, were measured identically to the serum bioassays. A 20 µL aliquot of calibration sample was mixed with 16 µL of measurement buffer and 4 µL of Ab-NP, incubated over 2 h and measured with the portable reader to obtain the corresponding signals. For each calibration sample, at least five different antibody sensing spots were measured to compute the mean and the standard deviation of the signal.

To obtain calibration curve for CRP, we used serial dilutions of a real human sample with a known CRP concentration characterized by an immunoturbidimetric test (266.9 µg mL⁻¹). The sample was diluted in BSA 7% PBS 1x at dilution ratios of 1:750*10³, 1:500*10³, 1:100*10³, 1:50*10³, 1:10*10³, and 1:10³ times, and the measurements were performed identically to PCT. Calibration curves for PCT and CRP were fitted to the measured points, according to the following equation:

$$y = d + \frac{a-d}{1+(\frac{x}{c})^b} \quad \text{Equation 5.1}$$

Where **a** is a theoretical response at zero concentration, **b** is a slope factor, **c** is a concentration inflection point, and **d** is a theoretical response at saturation.

5.5.8. Optical reader:

The nanoplasmonic imager is made of off-the-shelf optical components and effectively comprises a portable bright-field imaging microscope. A narrowband light emitting diode (LED) source (Thorlabs M660L4) in combination with a bandpass filter with 660 nm center wavelength and 10 nm full-width-at-half-maximum (Thorlabs) is used for narrow-band illumination at the wavelength of Au-NHA EOT peak. The light from the LED is collimated with an aspherical condenser lens (Thorlabs). A custom Al holder for the sensor chamber was fabricated to accommodate the sensor inside the reader. The light is transmitted through the sample chamber, modulated by Au-NHA sensor, and the imaging is performed using a 50x objective (Nikon) and a black-and-white CMOS camera (IDS B-UI-3200SE-M-GL). The CMOS camera has 4104 x 3006 pixels with 3.45 μm pixel size. The system enables imaging of $\sim 900 \mu\text{m} \times 700 \mu\text{m}$ field-of-view (FOV) area with an $\sim 1.5 \mu\text{m}$ resolution (diffraction-limited spot). The reader dimensions are 10 x 10 x 35 cm and the weight is less than 1 kg.

5.5.9. Image processing:

Image acquisition and processing was performed using custom Matlab functions and a graphical user interface from a laptop connected to the CMOS camera. Images from Au-NHA sensors were recorder using custom auto-exposure function to ensure similar intensity profiles across all images, and so that image histogram is always covered by the dynamic range of the CMOS. The images were normalized by the background illumination to exclude the source variations. To extract the NP signal, image areas were analyzed using a fixed intensity threshold to quantify bound NPs. The percentage number of pixels in an area darker than the threshold was used for quantification. The intensity threshold was optimized by matching plasmonic images to scanning electron micrographs of identical Au-NHA areas to maximize the number of detected NPs, while minimizing false-positive signals [213]. Importantly, Au-NP aggregates can be

identified and filtered out from the signal, as described previously [213]. A custom Matlab function was used to recognize QR codes from the images and extract encoded information. For the end-point measurements at least five different FOV were acquired and analyzed from each sensor chip for statistical significance. In order to control for non-specific NPs binding and background fluctuations, signal from each measured spot was corrected by subtracting the signal from adjacent BSA blocked background area. During time-resolved measurements, the images of a single FOV were recorded with 30 seconds interval. Each field of view had at least three antibody spots, which enabled to assess the mean and standard deviation of the signal from each frame. In order to evaluate detection cut-off times signal from three PCT sensing spots and its 95% confidence interval ($\pm 1.96 \cdot \delta$) were estimated at each time point. To establish the background signal and its variation, we plot average from three BSA blocked areas at each time point and compute running time averaged 95% confidence interval. The time averaged standard deviation at every time point T was computed to incorporate variances of background signals of all individual previous frames t_i :

$$\delta_T = \sqrt{\frac{\sum_{i=0}^n \delta_{t_i}^2}{n}} \quad \text{Equation 5.2}$$

We considered a reliable detection when the PCT signal's 95% lower confidence interval exceeds the background's upper confidence interval.

Acknowledgments

We would like to thank *Center of MicroNano Technology at École Polytechnique Fédérale de Lausanne* and *University of California Santa Barbara Nanofabrication Facility* for providing support with chip manufacturing. *Diesse diagnostic senese SPA* for providing human C-reactive protein (CRP) and anti-CRP monoclonal IgG

antibodies; BRAHMS ThermoFisher for providing recombinant human procalcitonin (PCT) and anti-PCT monoclonal antibodies. We acknowledge the support of the *École Polytechnique Fédérale de Lausanne* and the European Union's Horizon 2020 research and innovation program under grant agreement no. 644956 (RAIS project). The VHIR-HUVH is supported by Plan Nacional de I+D+i 2013- 2016 and Instituto de Salud Carlos III, Subdirección General de Redes y Centros de Investigación Cooperativa, Ministerio de Economía, Industria y Competitividad, Spanish Network for Research in Infectious Diseases (REIPI RD16/0016/0003) - cofinanced by European Development Regional Fund "A way to achieve Europe", Operative program Intelligent Growth 2014

Author Contributions

Author contributions: A.B. and F.Y. contributed equally to this work. A.B., F.Y. and H.A. conceived the study. A.B. and F.Y. developed the DENIS device and designed the experiments. A.F., J.G., J.R. and R.F. coordinated collection of human samples and clinical data and assisted with interpretation of results. A.B. and F.Y. conducted experiments and analysed the data. A.B., F.Y. and H.A. wrote the manuscript with review from all other authors.

5.6. Supporting Information

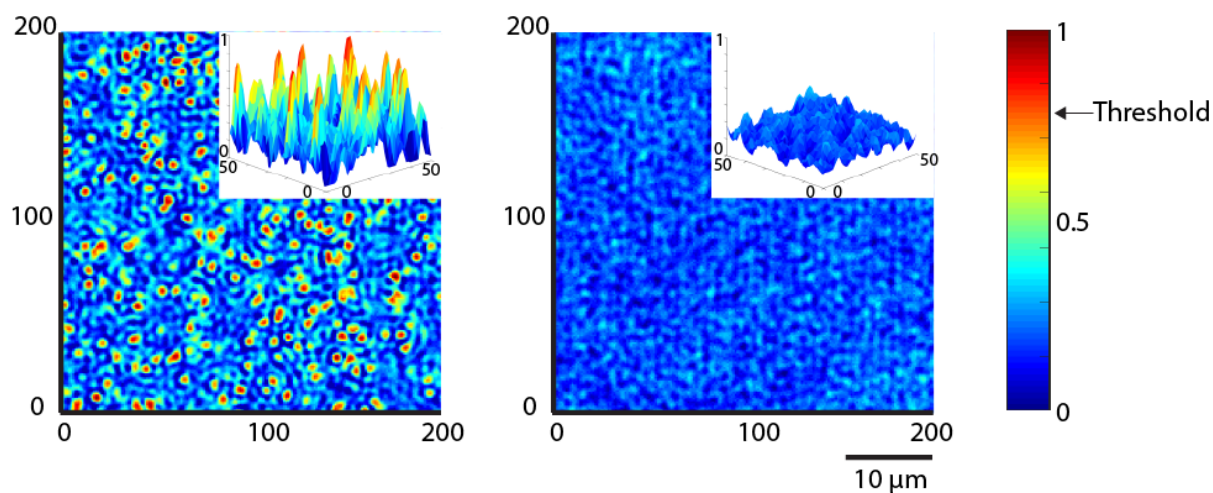
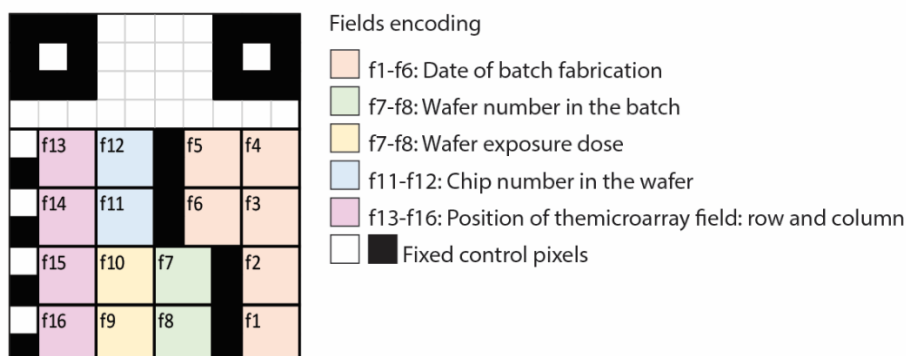
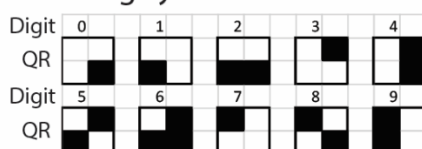


Figure S5.1. Processing of plasmonic images from Au-NHA with and without bound Au-NPs inside serum sample with Au-NPs, a) and b), respectively. An intensity threshold to identify Au-NPs was determined from the mapping of plasmonic images to scanning electron micrographs of the same Au-NHA areas. Notably, the intensity change caused by the binding of individual Au-NPs is several times higher than the changes caused by instrumental and background noise from the media.

a) QR coding



b) Encoding system



c) Example QR code

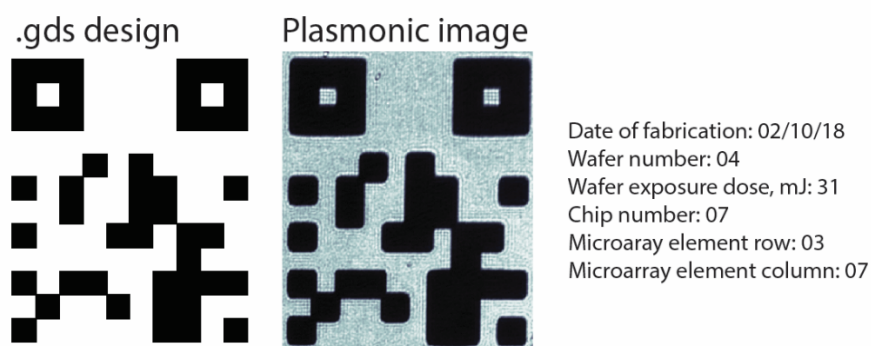


Figure S5.2. Quick response (QR) codes enable unique encoding of individual sensor chips and microarray locations on the chips. a) Scheme of QR code design. Each QR code is 100 x 120 μm in size and is composed of 10 by 12 pixels, each pixel 10 x 10 μm . Every pixel in the QR code can be either patterned with Ti (dark, 1), or free of Ti (bright, 0). Each QR code is unique and carries information (illustrated in colored fields) about the date of the wafer batch fabrication, identification number of the wafer in the batch, wafer exposure dose in the deep-UV lithography process, identification number of the chip in the wafer, and the position of the microarray field on the chip (row and

column). Pixels depicted in black and white are fixed on each QR and form a pattern for control and alignment for automatic machine vision recognition using a custom Matlab script. An array of 10 by 14 of unique QR codes is patterned on each sensor chip with horizontal period of 750 μm and vertical period of 450 μm . The generation of QR codes is performed using custom Matlab script that creates wafer-scale design in .gds format for the patterning of 65 chips per wafer and 140 QR codes per chip. b) System to encode numerical digits in the fields of QR code. c) An example QR code patterned on one of the sensor chips with decoded QR information.

	Sepsis, n = 18	ni-SIRS, n = 11	Healthy, n = 5
Gender (F or M)	13 M, 5 F	5 M, 6 F	3 M, 2 F
Age, years (SD)	58.9 (13.5) (28 - 81)	62.7 (18.2) (35-84)	46.4 (18) (18-65)
Cause	7 Respiratory infection 4 Urinary infection 7 Abdominal infection	9 Cardiac surgery 2 Lung transplant	---
Survival	14 Survived 4 Deceased	11 Survived	5 Survived
APACHE II, mean points (SD)	22.7 (7.5)	14.6 (3.4)	
SOFA, mean points (SD)	7.5 (3)	4.9 (2.3)	
Lactates, mmol L ⁻¹ , mean (SD)	3.8 (2.5)	1.5 (0.7)	
Leukocytes, x10E9 L ⁻¹ , median (25th & 75th percentiles)	9'365 (643-16'740)	13'000 (12'045-22'640)	
Platelets, x10E9 L ⁻¹ , median (25th & 75th percentiles)	141'500 (31'250-279'750)	137'000 (98'500-212'500)	
INR, mean (SD)	1.7 (1.1)	1.17 (0.1)	
Vasoactive Support, %	50	27.3	
Mechanical Ventilation, %	33.3	100	
ICU admission, %	61.1	100	
Hospital Mortality, %	22.2	0	

Table S5.1. Summary of the septic, non-infectious SIRS (ni-SIRS), and healthy subject groups.

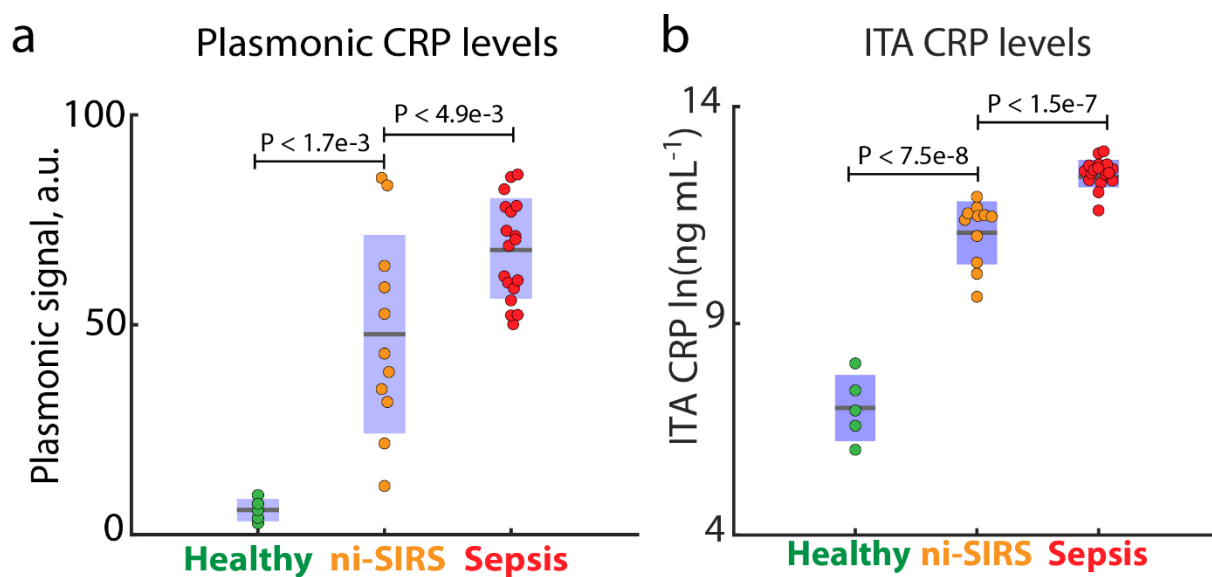


Figure S5.3. CRP levels measured for the 34 patients using a) DENIS and b) validated immunoassay in clinical lab. ni-SIRS stands for non-infectious SIRS.



Figure S5.4. Photograph of 25 clinical serum samples used in the measurements with DENIS at Vall d'Hebron University Hospital Biobank thawing on ice. The DENIS system was robust against the significant differences in color and consistency of the serum samples.

Supporting Video File is available at
<https://onlinelibrary.wiley.com/action/downloadSupplement?doi=10.1002%2Fsmll.201906108&file=smll201906108-sup-0002-VideoS1.mp4>

Figure S5.5. Real-time video obtained by DENIS system during real-time PCT measurements of a septic patient sample ($[PCT] = 24.26 \text{ ng mL}^{-1}$).

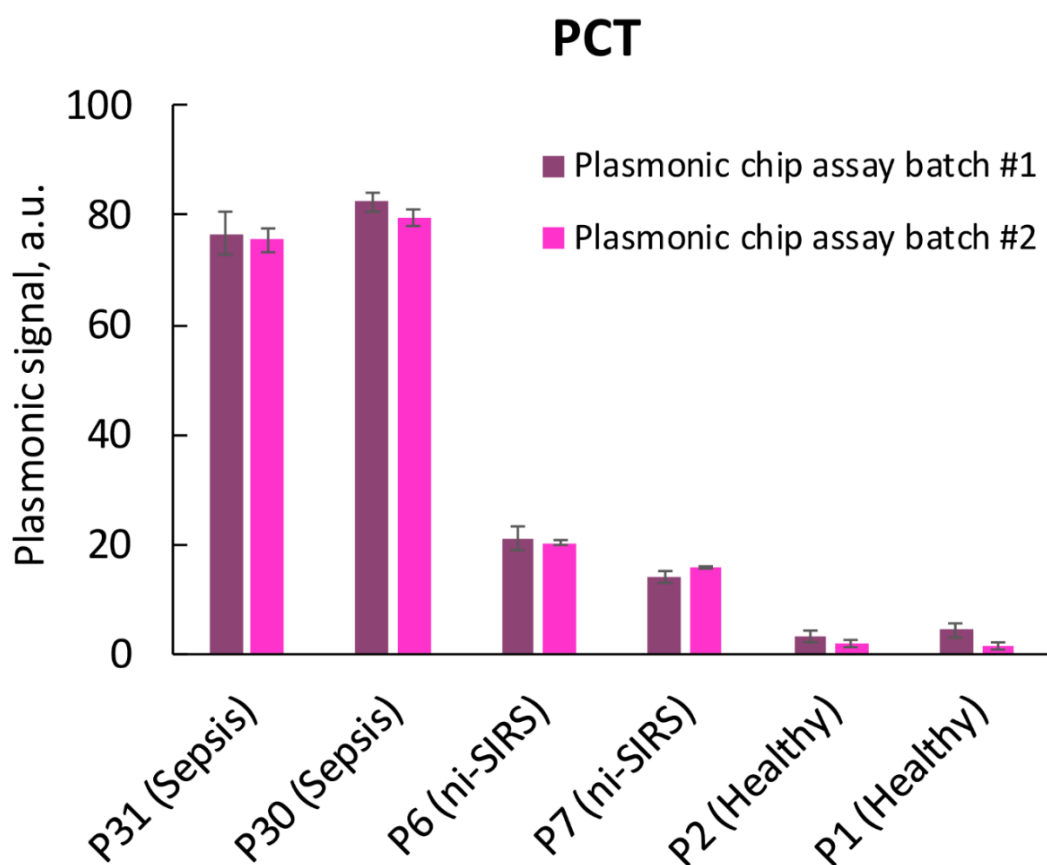


Figure S5.6. Reproducibility of the DENIS platform for detecting PCT. Technical replicates of PCT measurements with DENIS were performed in two sets of independent experiments for six different patients. Before the measurements, the plasmonic sensors and the assay reagents were stored in the fridge at 4°C for 1 week and 5 weeks in batch #1 and batch #2, respectively. ni-SIRS stands for non-infectious SIRS.

Chapter 6

Conclusions and outlook

State-of-the-art biosensors and analytical tools that are used in modern healthcare are costly, bulky, and require long detection times, sophisticated infrastructure and trained personnel. These factors limit their application in medical diagnostics and particularly to manage rapidly progressing fatal diseases, such as acute inflammation and sepsis, which require immediate intervention. The results of this thesis advance the development of nanoplasmonic sensors and their diagnostic applications by introducing a new sensing mechanism enabled by the interactions between gold nanohole arrays and gold nanoparticles and showcasing its application at the point-of-care to assist the diagnosis of inflammatory diseases including sepsis and SIRS.

This chapter summarizes the main achievements of this thesis, listing the main scientific, technological, and bioanalytical results, and briefly outlines directions for the future developments of this work.

6.1. Main achievements

In the first original contribution, a novel plasmonic sensing technique was introduced that allows imaging of single sub-wavelength Au NPs on large-area Au-NHAs in a bright-field imaging set-up, enabling the detection of individual molecule binding in complex samples. In the second original contribution, the novel plasmonic sensor technology was integrated into a portable point-of-care device and validated for the detection of sepsis-related biomarkers with patient blood serum samples. Overall, this

PhD work led to multiple peer-reviewed journal papers and conference publications and also a patent application.

6.1.1. Nanoparticle enhanced plasmonic biosensor

A novel imaging-based plasmonic biosensor based on Au-NHAs enhanced by Au NPs for ultra-sensitive detection of disease proteins with limits of detection up to four orders of magnitude below the clinical levels was introduced.

- The interactions between Au-NHAs and NPs were numerically characterized with FDTD simulations and the main principles behind the mechanism were described.
- Unlike conventional plasmonic sensing approaches that rely on transduction of biomolecular bindings through spectral shifts of plasmonic resonances, the novel method exploits intensity modulations caused by individual NPs on Au-NHAs. Therefore, the technology overcomes classical plasmonic detection limits imposed by refractive index sensitivity.
- The method utilizes a simple bright-field imaging set-up and allows digital imaging of single sub-wavelength gold nanoparticles (NPs) on large-area gold nanohole arrays (Au-NHAs) in a microarray format.
- The sensor generates image heatmaps of high contrast spikes corresponding to single NPs and enables precise visualization and quantification of the individual nanoparticle-labeled molecules.
- Using a single-step sandwich immunoassay, this novel biosensing approach enables the detection of biotinylated bovine serum albumin (bBSA, 67 kDa) and human C-reactive protein (CRP, 100 kDa), a well-established biomarker in clinical diagnosis and management of acute inflammatory diseases. The approach shows remarkable limit-of-detection with values down to 10 pg/ml for bBSA and 27 pg/ml for CRP.

6.1.2. Rapid and digital detection of inflammatory biomarkers

A novel portable optical biosensor to assist sepsis diagnosis was developed and validated in a hospital based on nanoparticle-enhanced digital plasmonic imaging technique.

- A portable imager (less than 1kg) was designed and built from low-cost off-the-shelf optical components.
- A single-step plasmonic bioassay was implemented that enabled highly sensitive and rapid detection of two sepsis-related biomarkers PCT and CRP directly from blood serum. The test does not require washing or amplification, is easy-to-use in resource-limited settings, and delivers reproducible performance after weeks of storage. The device has outstanding detection sensitivities directly from blood serum with limit-of-detection (LOD) down to 21 pg/mL and 36 pg/mL for PCT and CRP, respectively, and a wide dynamic range of at least 3 orders of magnitude, remarkably compatible with diagnostic levels.
- The portable reader was deployed at Vall d'Hebron University Hospital in Spain and its performance was evaluated in clinical settings by testing the samples from 18 sepsis, 11 non-infectious SIRS, and 5 healthy subjects.
- The results obtained with nanoplasmonic biosensor were directly benchmarked against ultimate clinical diagnosis and currently used immunoassays and showed that the novel device provided accurate and robust performance equivalent to gold-standard laboratory tests.
- Real-time image signal processing showed that identification of biomarker levels can be performed in under 15 minutes on-site, providing critical advantage compared to laboratory testing.

The POC plasmonic biosensor introduced in this thesis promises to provide a rapid and accurate tool to assist the diagnosis and management of acute inflammatory diseases.

6.1.3. Scientific output

The publications based on the outcomes of and contributions from this PhD work are listed below:

Journal publications

1. Belushkin, A., Yesilkoy, F., González-López, J.J., Ruiz-Rodríguez, J.C., Ferrer, R., Fàbrega, A. and Altug, H., 2020. Rapid and Digital Detection of Inflammatory Biomarkers Enabled by a Novel Portable Nanoplasmonic Imager. *Small*, p.1906108.
2. Belushkin, A., Yesilkoy, F. and Altug, H., 2018. Nanoparticle-enhanced plasmonic biosensor for digital biomarker detection in a microarray. *ACS nano*, 12(5), pp.4453-4461.
3. Yesilkoy, F., Terborg, R.A., Pello, J., Belushkin, A.A., Jahani, Y., Pruneri, V. and Altug, H., 2018. Phase-sensitive plasmonic biosensor using a portable and large field-of-view interferometric microarray imager. *Light: Science & Applications*, 7(2), p.17152.
4. Dey, P., Fabri-Faja, N., Calvo-Lozano, O., Terborg, R.A., Belushkin, A., Yesilkoy, F., Fàbrega, A., Ruiz-Rodriguez, J.C., Ferrer, R., González-López, J.J. and Estévez, M.C., 2018. Label-free bacteria quantification in blood plasma by a bioprinted microarray based interferometric point-of-care device. *ACS sensors*, 4(1), pp.52-60.
5. Li, X., Soler, M., Özdemir, C.I., Belushkin, A., Yesilköy, F. and Altug, H., 2017. Plasmonic nanohole array biosensor for label-free and real-time analysis of live cell secretion. *Lab on a chip*, 17(13), pp.2208-2217.
6. Soler, M., Belushkin, A., Cavallini, A., Kebbi-Beghdadi, C., Greub, G. and Altug, H., 2017. Multiplexed nano- plasmonic biosensor for one-step simultaneous detection of *Chlamydia trachomatis* and *Neisseria gonorrhoeae* in urine. *Biosensors and Bioelectronics*, 94, pp.560-567.

Patent

- A. Belushkin, F. Yesilköy, H. Altug Yanik. Patent application “Plasmonic biosensor” (2019) No. PCT/IB2019/052475. Pub. No.: WO/2019/186416.

Conference proceedings

1. Belushkin et. al, ‘Nanoplasmonic imaging biosensor for digital detection of disease biomarkers’, 5th Healthcare & Life Science & Entrepreneurship workshop 2020, Accepted for Talk
2. A. Belushkin et. al, ‘Nanoplasmonic imaging biosensor for digital detection of disease biomarkers’, SPIE Photonics West, SPIE BiOS, 2020, Talk
3. A. Belushkin et. al, ‘Nanoparticle Enhanced Plasmonic Biosensor for Digital Biomarker Detection in a Microarray’, Single-Molecule Sensors and NanoSystems International Conference 2019, Talk
4. A. Belushkin, ‘Nanoparticle-Enhanced Plasmonic Biosensor for Digital Biomarker Detection in a Microarray’, EDM Research Day 2018, Talk
5. A. Belushkin et. al ‘Real-time hydrodynamically enhanced plasmonic biosensor based on CCD imaging’, International Congress on Analytical Nanoscience and Nanotechnology 2017, Poster
6. A. Belushkin et. al ‘Enhancing the sensitivity of high-throughput plasmonic biosensors with microfluidics’, MicroTAS 2016, 1200-1202, Poster

6.2. Outlook

The development of this work opens a number of directions in which the current technology can be improved. Two of them are briefly outlined below. Specifically, further sensitivity enhancement and more rapid detection of low biomarker levels would open the path towards diagnostic applications that are currently impossible with existing POC technologies. For example, detection of 1-20 pg/ml of troponin in blood can predict myocardial infarction hours before the onset of ischemic symptoms [18].

6.2.1. Increased measurement sensitivity and reduced time-to-result with active microfluidic flow

To fully benefit from the performance of surface based sensing, the delivery of the target molecules to the sensor surface is crucial. Microfluidic platforms, integrated on the sensor chips, operate in laminar flow regime where molecular transport from the solution to the surface is limited by diffusion [224]. Therefore, the ultimate lower limit of detection (LOD) of a surface-based biosensors can be tuned by the microfluidic platform design, enhancing analyte delivery [225]. Here, the example of IgG binding to protein AG was used to demonstrate the correspondence of experimental in-situ results with theoretical and numerical estimations for different microfluidic channel designs (Figure 6.1). We estimated the diffusion range for each microfluidic system and calculated the total flux into this effective surface volume using numerical simulation tools (COMSOL) (Figure 6.2). Biosensing experiments with a series of IgG dilutions were performed to obtain calibration data plots for each microchannel. We experimentally show that scaling of channel height has greater effect on sensitivity, than width, in line with theoretical derivations, where flux to the sensor scales with channel Height^{-2/3} and Width^{-1/3} (Equation 6.1).

$$F \sim C_{A,0} \left(\frac{6D^2Q}{LH^2W} \right)^{1/3} \quad \text{Equation 6.1}$$

Where $C_{A,0}$ is bulk analyte concentration, D analyte diffusivity, Q volumetric flow rate, L , H and W – channel length, height and width, respectively.

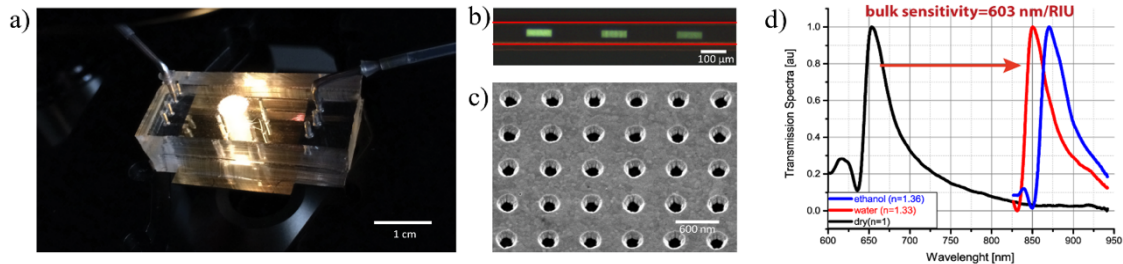


Figure 6.1 a) Plasmonic biosensing platform: NHA sensor chip integrated with microfluidics in an inverted microscope. b) Top view of 3 nanohole array sensors inside a microfluidic channel. c) SEM of gold nanohole array. d) Bulk refractive index sensitivity of NHA biosensor.

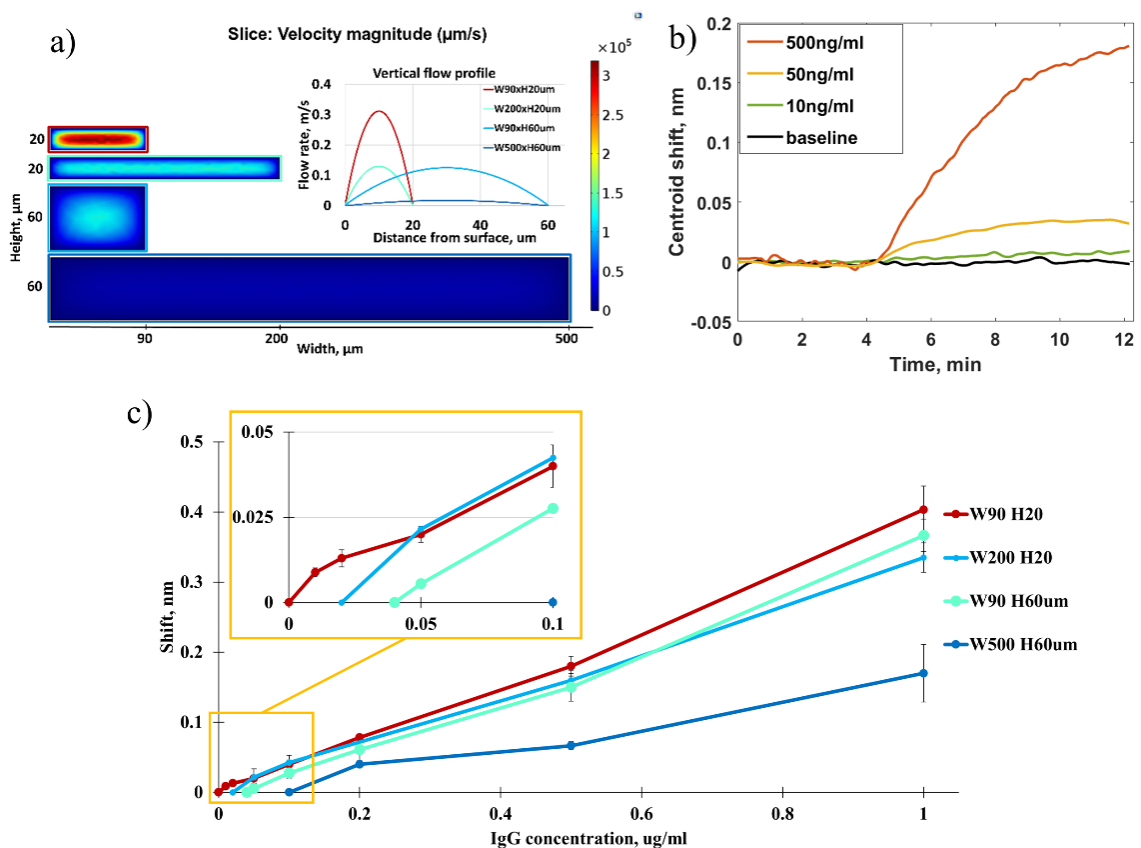


Figure 6.2 a) Flow velocity profiles for different microfluidic channels were simulated in COMSOL at a constant volumetric flow rate of 20 $\mu\text{l}/\text{min}$. b) The binding of IgG on protein AG-functionalized sensor results in local refractive index change that can be detected in real-time as a shift of transmission peak. c) IgG calibration curves show significant improvement of LOD with smaller microfluidic channel.

Overall, a 10-fold improvement of LOD was achieved by reducing channel cross-section. This work can be applied to the presented POC device to overcome limitation of NP diffusion. However, it will require incorporation of a microfluidic pump that will increase size, cost, and can compromise robustness of the POC sensor.

6.2.2. Increased measurement sensitivity and reduced time-to-result with electrohydrodynamic steering

Alternating-current electrohydrodynamic (AC-EHD) steering is a technique used to provide nanoshearing in laminar fluid flow and disrupt diffusion limited analyte transport to the sensor surface [226]. The application of electric field induces a force on the charges in the double layer of each electrode causing a net fluid flux in the direction of the broken symmetry (Figure 6.3).

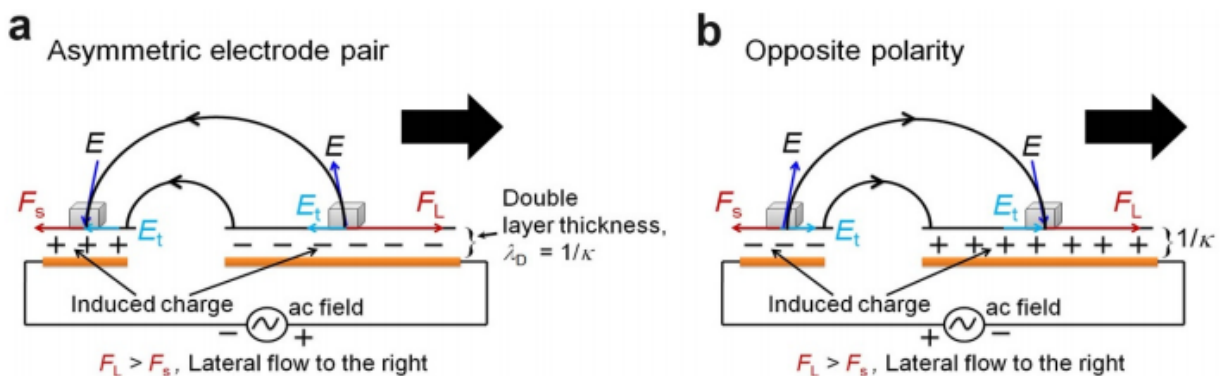


Figure 6.3 Illustration of mechanism behind AC-EHD induced fluid flow. Image reproduced from [227].

The technique was reported to enhance biosensing performance of surface based fluorescent and plasmonic sensors [227]–[229] and could be applied to Au-NHA - Au NP sensor by fabricating electrodes in the continuous Au-NHA film. However, introduction of gaps in the gold film causes light leakage in the transmission measurements through transparent glass substrate (Figure 6.4). This light will ultimately

obscure measurements of transmission through Au-NHA. For this reason, gaps between the electrodes will need to be blocked with a material that has high optical density and is electrically insulating at the same time.

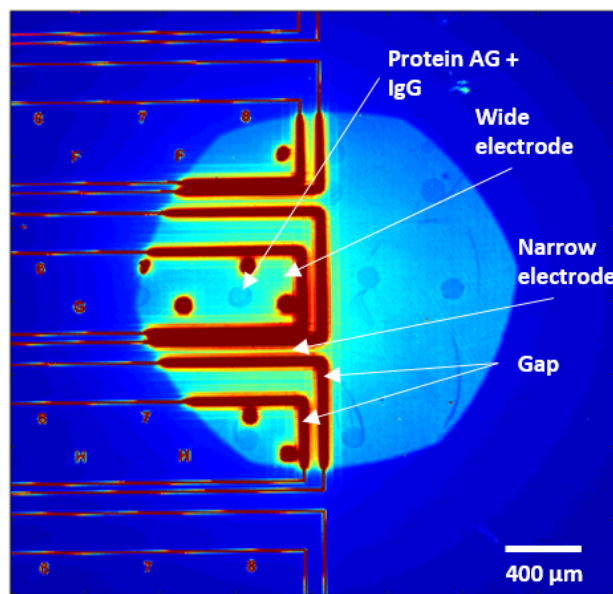


Figure 6.4 Plasmonic image of Au-NHA chip patterned with electrodes and functionalized with protein AG. Binding of IgG was performed over 1 h with applied AC current applied to the electrodes at 200 mV and 600 Hz. The wide electrode is 400 μm wide, narrow electrode is 100 μm wide, electrode separation is 50 μm and gap in gold film is 10 μm .

6.2.3. Technology transfer and development

The novel portable optical biosensor can be further advanced by improving the technology readiness level. In particular, the following steps will help transfer the technology to an industrial application:

- Lowering the cost of NHA fabrication, for example by scaling up the DUVL process to larger wafer substrates or implementing a different low-cost large-scale manufacturing technique, such as nanoimprint lithography.

- Development and fabrication of a disposable ready-to-use test cartridge integrated with NHA sensor by an industrial process, such as injection molding or 3D printing.
- Multiplexed detection of a panel of biomarkers to provide more detailed diagnostics (Figure 6.5).
- Improvement of the storage stability of the assay components and expanded testing of their shelf life.
- Further miniaturization and automatization of the optical reader using low-cost industrial components.
- Development and implementation of user-friendly software to control the device and perform measurements, which can be assisted by machine learning and machine vision algorithms.

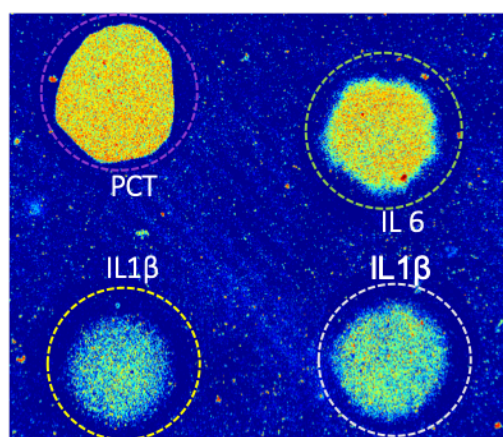


Figure 6.5 Plasmonic image of multiplexed detection of PCT (10 ng/ml), IL6 (1 ng/ml), and IL1 β (500 pg/ml).

References

- [1] “The European Medical Technology industry in figures 2018,” MedTech Europe. <https://www.medtecheurope.org/resource-library/the-european-medical-technology-industry-in-figures-2018/> (accessed Feb. 24, 2020).
- [2] C. for D. E. and Research, “Considerations for Use of Histopathology and Its Associated Methodologies to Support Biomarker Qualification Guidance for Industry,” U.S. Food and Drug Administration, Apr. 22, 2019. <http://www.fda.gov/regulatory-information/search-fda-guidance-documents/considerations-use-histopathology-and-its-associated-methodologies-support-biomarker-qualification> (accessed Feb. 24, 2020).
- [3] R. D. Cardiff, J. P. Gregg, J. W. Miller, D. E. Axelrod, and A. D. Borowsky, “Histopathology as a Predictive Biomarker: Strengths and Limitations,” *The Journal of Nutrition*, vol. 136, no. 10, pp. 2673S-2675S, Oct. 2006, doi: 10.1093/jn/136.10.2673S.
- [4] I. Dregely, D. Prezzi, C. Kelly-Morland, E. Roccia, R. Neji, and V. Goh, “Imaging biomarkers in oncology: Basics and application to MRI,” *Journal of Magnetic Resonance Imaging*, vol. 48, no. 1, pp. 13–26, 2018, doi: 10.1002/jmri.26058.
- [5] J. J. Smith, A. G. Sorensen, and J. H. Thrall, “Biomarkers in Imaging: Realizing Radiology’s Future1,” *Radiology*, Jun. 2003, doi: 10.1148/radiol.2273020518.
- [6] V. Kulasingam and E. P. Diamandis, “Strategies for discovering novel cancer biomarkers through utilization of emerging technologies,” *Nature clinical practice Oncology*, vol. 5, no. 10, pp. 588–599, 2008.
- [7] D. L. Nelson and M. M. Cox, *Lehninger principles of biochemistry*. 6., internat. ed. New York: Freeman, 2013.
- [8] E. A. Ponomarenko et al., “The Size of the Human Proteome: The Width and Depth,” *Int J Anal Chem*, vol. 2016, 2016, doi: 10.1155/2016/7436849.
- [9] L. M. Smith and N. L. Kelleher, “Proteoform: a single term describing protein complexity,” *Nature Methods*, vol. 10, no. 3, pp. 186–187, Mar. 2013, doi: 10.1038/nmeth.2369.
- [10] M. Neagu, C. Constantin, C. Tanase, and D. Boda, “Patented biomarker panels in early detection of cancer,” *Recent patents on biomarkers*, vol. 1, no. 1, pp. 10–24, 2011.

-
- [11] D. J. Brennan, D. P. O’connor, E. Rexhepaj, F. Ponten, and W. M. Gallagher, “Antibody-based proteomics: fast-tracking molecular diagnostics in oncology,” *Nature Reviews Cancer*, vol. 10, no. 9, pp. 605–617, 2010.
- [12] C. A. K. Borrebaeck, “Precision diagnostics: moving towards protein biomarker signatures of clinical utility in cancer,” *Nat Rev Cancer*, vol. 17, no. 3, pp. 199–204, Mar. 2017, doi: 10.1038/nrc.2016.153.
- [13] B. M. Biron, A. Ayala, and J. L. Lomas-Neira, “Biomarkers for Sepsis: What Is and What Might Be?,” *Biomark Insights*, vol. 10, no. Suppl 4, pp. 7–17, Sep. 2015, doi: 10.4137/BMI.S29519.
- [14] E. Boschetti, A. D’Amato, G. Candiano, and P. G. Righetti, “Protein biomarkers for early detection of diseases: The decisive contribution of combinatorial peptide ligand libraries,” *Journal of Proteomics*, vol. 188, pp. 1–14, Sep. 2018, doi: 10.1016/j.jprot.2017.08.009.
- [15] A. K. Füzéry, J. Levin, M. M. Chan, and D. W. Chan, “Translation of proteomic biomarkers into FDA approved cancer diagnostics: issues and challenges,” *Clinical proteomics*, vol. 10, no. 1, p. 13, 2013.
- [16] A. Kirwan, M. Utratna, M. O’Dwyer, L. Joshi, and M. Kilcoyne, “Glycosylation-Based Serum Biomarkers for Cancer Diagnostics and Prognostics,” *BioMed Research International*, vol. 2015, Oct. 2015, doi: 10.1155/2015/490531.
- [17] H.-G. Schneider and Q. T. Lam, “Procalcitonin for the clinical laboratory: a review,” *Pathology*, vol. 39, no. 4, pp. 383–390, 2007.
- [18] F. S. Apple, “High-sensitivity cardiac troponin for screening large populations of healthy people: is there risk?,” *Clinical chemistry*, vol. 57, no. 4, pp. 537–539, 2011.
- [19] G. C. Jickling and F. R. Sharp, “Blood Biomarkers of Ischemic Stroke,” *Neurotherapeutics*, vol. 8, no. 3, pp. 349–360, Jul. 2011, doi: 10.1007/s13311-011-0050-4.
- [20] T. Monbailliu, J. Goossens, and S. Hachimi-Idrissi, “Blood protein biomarkers as diagnostic tool for ischemic stroke: a systematic review,” *Biomarkers in Medicine*, vol. 11, no. 6, pp. 503–512, May 2017, doi: 10.2217/bmm-2016-0232.
- [21] K. R. McIntire, T. A. Waldmann, C. G. Moertel, and V. L. Go, “Serum alpha-fetoprotein in patients with neoplasms of the gastrointestinal tract.,” *Cancer research*, vol. 35, no. 4, pp. 991–996, 1975.
- [22] S. Maestranzi, R. Przemioslo, H. Mitchell, and R. A. Sherwood, “The effect of benign and malignant liver disease on the tumour markers CA19-9 and CEA,” *Annals of clinical biochemistry*, vol. 35, no. 1, pp. 99–103, 1998.

-
- [23] F. Weiland, K. Martin, M. K. Oehler, and P. Hoffmann, "Deciphering the Molecular Nature of Ovarian Cancer Biomarker CA125," *Int J Mol Sci*, vol. 13, no. 8, pp. 10568–10582, Aug. 2012, doi: 10.3390/ijms130810568.
- [24] S. M. Ali et al., "Serum HER-2/neu and relative resistance to trastuzumab-based therapy in patients with metastatic breast cancer," *Cancer: Interdisciplinary International Journal of the American Cancer Society*, vol. 113, no. 6, pp. 1294–1301, 2008.
- [25] B. S. H. Indrasena, "Use of thyroglobulin as a tumour marker," *World J Biol Chem*, vol. 8, no. 1, pp. 81–85, Feb. 2017, doi: 10.4331/wjbc.v8.i1.81.
- [26] K.-A. Lee et al., "Aptamer-based Sandwich Assay and its Clinical Outlooks for Detecting Lipocalin-2 in Hepatocellular Carcinoma (HCC)," *Scientific Reports*, vol. 5, no. 1, Art. no. 1, Jun. 2015, doi: 10.1038/srep10897.
- [27] W. Tang et al., "Des-gamma-carboxy prothrombin in cancer and non-cancer liver tissue of patients with hepatocellular carcinoma," *Int. J. Oncol.*, vol. 22, no. 5, pp. 969–975, May 2003.
- [28] G. Zhang, X. Sun, H. Lv, X. Yang, and X. Kang, "Serum amyloid A: A new potential serum marker correlated with the stage of breast cancer," *Oncol Lett*, vol. 3, no. 4, pp. 940–944, Apr. 2012, doi: 10.3892/ol.2012.584.
- [29] M. Montalbano et al., "Biology and function of glypican-3 as a candidate for early cancerous transformation of hepatocytes in hepatocellular carcinoma (Review)," *Oncology Reports*, vol. 37, no. 3, pp. 1291–1300, Mar. 2017, doi: 10.3892/or.2017.5387.
- [30] A. E. Prizment et al., "Circulating Beta-2 Microglobulin and Risk of Cancer: The Atherosclerosis Risk in Communities Study (ARIC)," *Cancer Epidemiol Biomarkers Prev*, vol. 25, no. 4, pp. 657–664, Apr. 2016, doi: 10.1158/1055-9965.EPI-15-0849.
- [31] S. Gkolfinopoulos, K. Tsapakidis, K. Papadimitriou, D. Papamichael, and P. Kountourakis, "Chromogranin A as a valid marker in oncology: Clinical application or false hopes?," *World J Methodol*, vol. 7, no. 1, pp. 9–15, Mar. 2017, doi: 10.5662/wjm.v7.i1.9.
- [32] R. Uusitalo-Seppälä et al., "Pentraxin 3 (PTX3) Is Associated with Severe Sepsis and Fatal Disease in Emergency Room Patients with Suspected Infection: A Prospective Cohort Study," *PLoS One*, vol. 8, no. 1, Jan. 2013, doi: 10.1371/journal.pone.0053661.
- [33] S. Pradhan et al., "The role of C-reactive protein as a diagnostic predictor of sepsis in a multidisciplinary Intensive Care Unit of a tertiary care center in Nepal," *Indian J Crit Care Med*, vol. 20, no. 7, pp. 417–420, Jul. 2016, doi: 10.4103/0972-5229.186226.

-
- [34] S. L. Salzberg, "Open questions: How many genes do we have?," *BMC Biol*, vol. 16, Aug. 2018, doi: 10.1186/s12915-018-0564-x.
- [35] M. Pertea and S. L. Salzberg, "Between a chicken and a grape: estimating the number of human genes," *Genome biology*, vol. 11, no. 5, p. 206, 2010.
- [36] T. A. Brown, *The Human Genome*. Wiley-Liss, 2002.
- [37] A. Annunziato, "DNA packaging: nucleosomes and chromatin," *Nature Education*, vol. 1, no. 1, p. 26, 2008.
- [38] J. A. Shaw and J. Stebbing, "Circulating free DNA in the management of breast cancer," *Ann Transl Med*, vol. 2, no. 1, Jan. 2014, doi: 10.3978/j.issn.2305-5839.2013.06.06.
- [39] L. Barault et al., "Discovery of methylated circulating DNA biomarkers for comprehensive non-invasive monitoring of treatment response in metastatic colorectal cancer," *Gut*, vol. 67, no. 11, pp. 1995–2005, 2018.
- [40] H. Schwarzenbach, D. S. B. Hoon, and K. Pantel, "Cell-free nucleic acids as biomarkers in cancer patients," *Nature Reviews Cancer*, vol. 11, no. 6, Art. no. 6, Jun. 2011, doi: 10.1038/nrc3066.
- [41] Z. Ma, M. Williams, Y. Y. Cheng, and W. K. Leung, "Roles of Methylated DNA Biomarkers in Patients with Colorectal Cancer," *Dis Markers*, vol. 2019, Mar. 2019, doi: 10.1155/2019/2673543.
- [42] E. D. Harris, "Biochemical facts behind the definition and properties of metabolites," Ebook, 1st edn. US Food and Drug Administration. Accessed November, 2014.
- [43] H. Tang and Y. Wang, "Metabonomics: a revolution in progress," *Sheng wu hua xue yu sheng wu wu li jin zhan*, vol. 33, no. 5, pp. 401–417, 2006.
- [44] P. K. Yeung, "Metabolomics and Biomarkers for Drug Discovery," *Metabolites*, vol. 8, no. 1, Jan. 2018, doi: 10.3390/metabo8010011.
- [45] M. Jacob, A. L. Lopata, M. Dasouki, and A. M. Abdel Rahman, "Metabolomics toward personalized medicine," *Mass spectrometry reviews*, vol. 38, no. 3, pp. 221–238, 2019.
- [46] X. Zhao, V. Modur, L. N. Carayannopoulos, and O. F. Laterza, "Biomarkers in pharmaceutical research," *Clinical chemistry*, vol. 61, no. 11, pp. 1343–1353, 2015.
- [47] S. M. Lee and W. S. An, "New clinical criteria for septic shock: serum lactate level as new emerging vital sign," *J Thorac Dis*, vol. 8, no. 7, pp. 1388–1390, Jul. 2016, doi: 10.21037/jtd.2016.05.55.

-
- [48] B. Yuan et al., “A plasma metabolite panel as biomarkers for early primary breast cancer detection,” *International Journal of Cancer*, vol. 144, no. 11, pp. 2833–2842, 2019, doi: 10.1002/ijc.31996.
- [49] M. Muthu and A. Nordström, “Current Status and Future Prospects of Clinically Exploiting Cancer-specific Metabolism—Why Is Tumor Metabolism Not More Extensively Translated into Clinical Targets and Biomarkers?,” *Int J Mol Sci*, vol. 20, no. 6, Mar. 2019, doi: 10.3390/ijms20061385.
- [50] H. Lv et al., “Metabolomics and Its Application in the Development of Discovering Biomarkers for Osteoporosis Research,” *International Journal of Molecular Sciences*, vol. 17, no. 12, p. 2018, Dec. 2016, doi: 10.3390/ijms17122018.
- [51] C. L. Albert and W. H. W. Tang, “Metabolic Biomarkers in Heart Failure,” *Heart Failure Clinics*, vol. 14, no. 1, pp. 109–118, Jan. 2018, doi: 10.1016/j.hfc.2017.08.011.
- [52] E. Boschetti, A. D’Amato, G. Candiano, and P. G. Righetti, “Protein biomarkers for early detection of diseases: The decisive contribution of combinatorial peptide ligand libraries,” *Journal of Proteomics*, vol. 188, pp. 1–14, Sep. 2018, doi: 10.1016/j.jpro.2017.08.009.
- [53] F. H. Stephenson, *Calculations for molecular biology and biotechnology*. Academic press, 2016.
- [54] O. H. Lowry, N. J. Rosebrough, A. L. Farr, and R. J. Randall, “Protein measurement with the Folin phenol reagent,” *J. Biol. Chem.*, vol. 193, no. 1, pp. 265–275, Nov. 1951.
- [55] R. I. Krohn, “The colorimetric detection and quantitation of total protein,” *Current protocols in cell biology*, vol. 52, no. 1, p. A-3H, 2011.
- [56] E. Engvall and P. Perlmann, “Enzyme-linked immunosorbent assay (ELISA),” *Protides of the biological fluids*, pp. 553–556, 1971.
- [57] S. Aydin, “A short history, principles, and types of ELISA, and our laboratory experience with peptide/protein analyses using ELISA,” *Peptides*, vol. 72, pp. 4–15, Oct. 2015, doi: 10.1016/j.peptides.2015.04.012.
- [58] L. Cinquanta, D. E. Fontana, and N. Bizzaro, “Chemiluminescent immunoassay technology: what does it change in autoantibody detection?,” *Auto Immun Highlights*, vol. 8, no. 1, Jun. 2017, doi: 10.1007/s13317-017-0097-2.
- [59] “Human ALDOC / Aldolase C Quant ELISA Kit | Sandwich CLIA | LSBio.” <https://www.lsbio.com/elisakits/human-aldoc-aldolase-c-elisa-kit-clia-ls-f29883/29883> (accessed Mar. 02, 2020).

-
- [60] Q. Liu, W. Feng, T. Yang, T. Yi, and F. Li, "Upconversion luminescence imaging of cells and small animals," *Nat Protoc*, vol. 8, no. 10, pp. 2033–2044, Oct. 2013, doi: 10.1038/nprot.2013.114.
- [61] A. M. Dupuy, S. Badiou, B. Descomps, and J. P. Cristol, "Immunoturbidimetric determination of C-reactive protein (CRP) and high-sensitivity CRP on heparin plasma. Comparison with serum determination," *Clin. Chem. Lab. Med.*, vol. 41, no. 7, pp. 948–949, Jul. 2003, doi: 10.1515/CCLM.2003.144.
- [62] "LIAPHEN vWF:Ag," Nodia. <https://www.nodia.be/site/liaphen-vwfag/> (accessed Feb. 25, 2020).
- [63] D. R. Thévenot, K. Toth, R. A. Durst, and G. S. Wilson, "Electrochemical biosensors: recommended definitions and classification! International Union of Pure and Applied Chemistry: Physical Chemistry Division, Commission I.7 (Biophysical Chemistry); Analytical Chemistry Division, Commission V.5 (Electroanalytical Chemistry).1," *Biosensors and Bioelectronics*, vol. 16, no. 1, pp. 121–131, Jan. 2001, doi: 10.1016/S0956-5663(01)00115-4.
- [64] D. Grieshaber, R. MacKenzie, J. Vörös, and E. Reimhult, "Electrochemical biosensors-sensor principles and architectures," *Sensors*, vol. 8, no. 3, pp. 1400–1458, 2008.
- [65] P. Estrela, J. L. Hammond, N. Formisano, P. Estrela, S. Carrara, and J. Tkac, "Electrochemical biosensors and nanobiosensors," *Essays Biochem*, vol. 60, no. 1, pp. 69–80, Jun. 2016, doi: 10.1042/EBC20150008.
- [66] L. El Harrad, I. Bourais, H. Mohammadi, and A. Amine, "Recent advances in electrochemical biosensors based on enzyme inhibition for clinical and pharmaceutical applications," *Sensors*, vol. 18, no. 1, p. 164, 2018.
- [67] C. Stagni et al., "CMOS DNA Sensor Array With Integrated A/D Conversion Based on Label-Free Capacitance Measurement," *IEEE Journal of Solid-State Circuits*, vol. 41, no. 12, pp. 2956–2964, Dec. 2006, doi: 10.1109/JSSC.2006.884867.
- [68] J. Wang, "Electrochemical Glucose Biosensors," *Chem. Rev.*, vol. 108, no. 2, pp. 814–825, Feb. 2008, doi: 10.1021/cr068123a.
- [69] S. A. Soper et al., "Point-of-care biosensor systems for cancer diagnostics/prognostics," *Biosensors and Bioelectronics*, vol. 21, no. 10, pp. 1932–1942, 2006.
- [70] A. Thomas, A. Ramírez, and A. Zehe, "Introduction to diabetes Nanotechnology tackles problems with noninvasive glucose monitoring," *European Pharmaceutical Review*, vol. 21, pp. 68–71, May 2016.

-
- [71] “Abbott Point of Care | i-STAT System & Piccolo Xpress.” https://www.pointofcare.abbott/us/en/home?utm_source=www.istat.com&utm_medium=email&utm_campaign=www.i-stat.com (accessed Feb. 27, 2020).
- [72] X. Zhang, H. Ju, and J. Wang, *Electrochemical sensors, biosensors and their biomedical applications*. Academic Press, 2011.
- [73] M. Sajid, A.-N. Kawde, and M. Daud, “Designs, formats and applications of lateral flow assay: A literature review,” *Journal of Saudi Chemical Society*, vol. 19, no. 6, pp. 689–705, Nov. 2015, doi: 10.1016/j.jscs.2014.09.001.
- [74] K. M. Koczula and A. Gallotta, “Lateral flow assays,” *Essays Biochem*, vol. 60, no. 1, pp. 111–120, Jun. 2016, doi: 10.1042/EBC20150012.
- [75] O. Miočević, C. R. Cole, M. J. Laughlin, R. L. Buck, P. D. Slowey, and E. A. Shirtcliff, “Quantitative Lateral Flow Assays for Salivary Biomarker Assessment: A Review,” *Front. Public Health*, vol. 5, 2017, doi: 10.3389/fpubh.2017.00133.
- [76] W. C. Mak, V. Beni, and A. P. F. Turner, “Lateral-flow technology: From visual to instrumental,” *TrAC Trends in Analytical Chemistry*, vol. 79, pp. 297–305, May 2016, doi: 10.1016/j.trac.2015.10.017.
- [77] S. H. Ang, M. Rambeli, T. M. Thevarajah, Y. B. Alias, and S. M. Khor, “Quantitative, single-step dual measurement of hemoglobin A1c and total hemoglobin in human whole blood using a gold sandwich immunochromatographic assay for personalized medicine,” *Biosensors and Bioelectronics*, vol. 78, pp. 187–193, Apr. 2016, doi: 10.1016/j.bios.2015.11.045.
- [78] I. Nakagiri et al., “Screening for human immunodeficiency virus using a newly developed fourth generation lateral flow immunochromatography assay,” *Journal of Virological Methods*, vol. 274, p. 113746, Dec. 2019, doi: 10.1016/j.jviromet.2019.113746.
- [79] T. C. Granade, S. Workman, S. K. Wells, A. N. Holder, S. M. Owen, and C.-P. Pau, “Rapid detection and differentiation of antibodies to HIV-1 and HIV-2 using multivalent antigens and magnetic immunochromatography testing,” *Clin. Vaccine Immunol.*, vol. 17, no. 6, pp. 1034–1039, 2010.
- [80] E. Nakku-Joloba et al., “Clinical Evaluation of Two Point-Of-Care Lateral Flow Tests for the Diagnosis of Syphilis,” *Sex Transm Dis*, vol. 43, no. 10, pp. 623–625, Oct. 2016, doi: 10.1097/OLQ.0000000000000498.
- [81] L. Liang et al., “Aptamer-based fluorescent and visual biosensor for multiplexed monitoring of cancer cells in microfluidic paper-based analytical devices,” *Sensors and Actuators B: Chemical*, vol. 229, pp. 347–354, 2016.

-
- [82] O. Strohmeier et al., “Centrifugal microfluidic platforms: advanced unit operations and applications,” *Chemical Society Reviews*, vol. 44, no. 17, pp. 6187–6229, 2015, doi: 10.1039/C4CS00371C.
- [83] S. Smith et al., “CD-Based Microfluidics for Primary Care in Extreme Point-of-Care Settings,” *Micromachines (Basel)*, vol. 7, no. 2, Jan. 2016, doi: 10.3390/mi7020022.
- [84] I. J. Michael, T.-H. Kim, V. Sunkara, and Y.-K. Cho, “Challenges and opportunities of centrifugal microfluidics for extreme point-of-care testing,” *Micromachines*, vol. 7, no. 2, p. 32, 2016.
- [85] M. Soler, C. S. Huertas, and L. M. Lechuga, “Label-free plasmonic biosensors for point-of-care diagnostics: a review,” *Expert Rev. Mol. Diagn.*, vol. 19, no. 1, pp. 71–81, Jan. 2019, doi: 10.1080/14737159.2019.1554435.
- [86] O. Tokel, F. Inci, and U. Demirci, “Advances in Plasmonic Technologies for Point of Care Applications,” *Chem Rev*, vol. 114, no. 11, pp. 5728–5752, Jun. 2014, doi: 10.1021/cr4000623.
- [87] K. Okamoto, *Fundamentals of Optical Waveguides*. Academic Press, 2006.
- [88] E. Chow, A. Grot, L. W. Mirkarimi, M. Sigalas, and G. Girolami, “Ultracompact biochemical sensor built with two-dimensional photonic crystal microcavity,” *Opt. Lett.*, OL, vol. 29, no. 10, pp. 1093–1095, May 2004, doi: 10.1364/OL.29.001093.
- [89] R. Ferrini et al., “Optical study of two-dimensional InP-based photonic crystals by internal light source technique,” *IEEE Journal of Quantum Electronics*, vol. 38, no. 7, pp. 786–799, Jul. 2002, doi: 10.1109/JQE.2002.1017588.
- [90] B. Špačková, P. Wrobel, M. Bocková, and J. Homola, “Optical Biosensors Based on Plasmonic Nanostructures: A Review,” *Proceedings of the IEEE*, vol. 104, no. 12, pp. 2380–2408, Dec. 2016, doi: 10.1109/JPROC.2016.2624340.
- [91] X. Fan, I. M. White, S. I. Shopova, H. Zhu, J. D. Suter, and Y. Sun, “Sensitive optical biosensors for unlabeled targets: A review,” *Analytica Chimica Acta*, vol. 620, no. 1, pp. 8–26, Jul. 2008, doi: 10.1016/j.aca.2008.05.022.
- [92] F. Vollmer and S. Arnold, “Whispering-gallery-mode biosensing: label-free detection down to single molecules,” *Nature Methods*, vol. 5, no. 7, Art. no. 7, Jul. 2008, doi: 10.1038/nmeth.1221.
- [93] K. V. Sreekanth et al., “Extreme sensitivity biosensing platform based on hyperbolic metamaterials,” *Nature materials*, vol. 15, no. 6, p. 621, 2016.

-
- [94] P. M. Kosaka et al., “Detection of cancer biomarkers in serum using a hybrid mechanical and optoplasmonic nanosensor,” *Nature Nanotech*, vol. 9, no. 12, pp. 1047–1053, Dec. 2014, doi: 10.1038/nnano.2014.250.
- [95] J. Park and J.-S. Yeo, “Colorimetric detection of microRNA miR-21 based on nanoplasmonic core–satellite assembly,” *Chemical Communications*, vol. 50, no. 11, pp. 1366–1368, 2014, doi: 10.1039/C3CC48154A.
- [96] J. Lee, J. Park, J.-Y. Lee, and J.-S. Yeo, “Contact Transfer Printing of Side Edge Prefunctionalized Nanoplasmonic Arrays for Flexible microRNA Biosensor,” *Advanced Science*, vol. 2, no. 9, p. 1500121, 2015, doi: 10.1002/advs.201500121.
- [97] F. Yesilkoy et al., “Ultrasensitive hyperspectral imaging and biodetection enabled by dielectric metasurfaces,” *Nat. Photonics*, vol. 13, no. 6, pp. 390–396, Jun. 2019, doi: 10.1038/s41566-019-0394-6.
- [98] H. Inan et al., “Photonic crystals: emerging biosensors and their promise for point-of-care applications,” *Chemical Society Reviews*, vol. 46, no. 2, pp. 366–388, 2017, doi: 10.1039/C6CS00206D.
- [99] C. Puente and I. López, “Plasmonic Ecomaterials,” in *Handbook of Ecomaterials*, L. M. T. Martínez, O. V. Kharissova, and B. I. Kharisov, Eds. Cham: Springer International Publishing, 2019, pp. 2561–2583.
- [100] R. W. Wood, “On a Remarkable Case of Uneven Distribution of Light in a Diffraction Grating Spectrum,” *Proc. Phys. Soc. London*, vol. 18, no. 1, pp. 269–275, Jun. 1902, doi: 10.1088/1478-7814/18/1/325.
- [101] Lord Rayleigh, “On the dynamical theory of gratings,” *Proceedings of the Royal Society of London. Series A, Containing Papers of a Mathematical and Physical Character*, vol. 79, no. 532, pp. 399–416, 1907.
- [102] E. Kretschmann and H. Raether, “Radiative decay of non radiative surface plasmons excited by light,” *Zeitschrift für Naturforschung A*, vol. 23, no. 12, pp. 2135–2136, 1968.
- [103] A. Otto, “Excitation of nonradiative surface plasma waves in silver by the method of frustrated total reflection,” *Zeitschrift für Physik A Hadrons and nuclei*, vol. 216, no. 4, pp. 398–410, 1968.
- [104] G. Kumar and P. K. Sarswat, “Interaction of Surface Plasmon Polaritons with Nanomaterials,” in *Reviews in Plasmonics 2015*, C. D. Geddes, Ed. Cham: Springer International Publishing, 2016, pp. 103–129.
- [105] J. Homola, “Electromagnetic Theory of Surface Plasmons,” in *Surface Plasmon Resonance Based Sensors*, J. Homola, Ed. Berlin, Heidelberg: Springer, 2006, pp. 3–44.

-
- [106] S. A. Maier, *Plasmonics: Fundamentals and Applications*. Springer Science & Business Media, 2007.
- [107] H. Neff, L. C. Oliveira, E. P. Rodrigues, C. Thirstrup, and A. M. N. Lima, “Enhanced Directed Radiative Surface Plasmon Emission from Periodically Corrugated Noble Metal Films,” *Plasmonics*, vol. 13, no. 6, pp. 2021–2027, Dec. 2018, doi: 10.1007/s11468-018-0718-2.
- [108] H. H. Nguyen, J. Park, S. Kang, and M. Kim, “Surface Plasmon Resonance: A Versatile Technique for Biosensor Applications,” *Sensors*, vol. 15, no. 5, pp. 10481–10510, May 2015, doi: 10.3390/s150510481.
- [109] A. J. Haes, D. A. Stuart, S. Nie, and R. P. Van Duyne, “Using Solution-Phase Nanoparticles, Surface-Confined Nanoparticle Arrays and Single Nanoparticles as Biological Sensing Platforms,” *Journal of Fluorescence*, vol. 14, no. 4, pp. 355–367, Jul. 2004, doi: 10.1023/B:JOFL.0000031817.35049.1f.
- [110] C. Chen and J. Wang, “Optical biosensors: an exhaustive and comprehensive review,” *Analyst*, vol. 145, no. 5, pp. 1605–1628, 2020, doi: 10.1039/C9AN01998G.
- [111] E. Luan, H. Shoman, D. M. Ratner, K. C. Cheung, and L. Chrostowski, “Silicon Photonic Biosensors Using Label-Free Detection,” *Sensors (Basel)*, vol. 18, no. 10, Oct. 2018, doi: 10.3390/s18103519.
- [112] A. B. Taylor and P. Zijlstra, “Single-Molecule Plasmon Sensing: Current Status and Future Prospects,” *ACS Sens.*, vol. 2, no. 8, pp. 1103–1122, Aug. 2017, doi: 10.1021/acssensors.7b00382.
- [113] J.-J. Greffet, “Introduction to Surface Plasmon Theory,” in *Plasmonics: From Basics to Advanced Topics*, S. Enoch and N. Bonod, Eds. Berlin, Heidelberg: Springer, 2012, pp. 105–148.
- [114] J. Zhao, X. Zhang, C. R. Yonzon, A. J. Haes, and R. P. Van Duyne, “Localized surface plasmon resonance biosensors,” *Nanomedicine*, vol. 1, no. 2, pp. 219–228, Aug. 2006, doi: 10.2217/17435889.1.2.219.
- [115] T. W. Ebbesen, H. J. Lezec, H. F. Ghaemi, T. Thio, and P. A. Wolff, “Extraordinary optical transmission through sub-wavelength hole arrays,” *Nature*, vol. 391, no. 6668, pp. 667–669, Feb. 1998, doi: 10.1038/35570.
- [116] H. A. Bethe, “Theory of diffraction by small holes,” *Physical review*, vol. 66, no. 7–8, p. 163, 1944.
- [117] C. Genet and T. W. Ebbesen, “Light in tiny holes,” *Nature*, vol. 445, no. 7123, pp. 39–46, Jan. 2007, doi: 10.1038/nature05350.

-
- [118] F. van Beijnum, C. R  tif, C. B. Smiet, H. Liu, P. Lalanne, and M. P. van Exter, “Quasi-cylindrical wave contribution in experiments on extraordinary optical transmission,” *Nature*, vol. 492, no. 7429, pp. 411–414, 2012.
- [119] H. Gao et al., “Rayleigh anomaly-surface plasmon polariton resonances in palladium and gold subwavelength hole arrays,” *Opt. Express*, OE, vol. 17, no. 4, pp. 2334–2340, Feb. 2009, doi: 10.1364/OE.17.002334.
- [120] F. Yesilkoy et al., “Phase-sensitive plasmonic biosensor using a portable and large field-of-view interferometric microarray imager,” *Light Sci Appl*, vol. 7, no. 2, pp. 17152–17152, Feb. 2018, doi: 10.1038/lsa.2017.152.
- [121] A. G. Brolo, R. Gordon, B. Leathem, and K. L. Kavanagh, “Surface Plasmon Sensor Based on the Enhanced Light Transmission through Arrays of Nanoholes in Gold Films,” *Langmuir*, vol. 20, no. 12, pp. 4813–4815, Jun. 2004, doi: 10.1021/la0493621.
- [122] A. E. Cetin et al., “Handheld high-throughput plasmonic biosensor using computational on-chip imaging,” *Light Sci Appl*, vol. 3, no. 1, pp. e122–e122, Jan. 2014, doi: 10.1038/lsa.2014.3.
- [123] Y. Eksio  lu, A. E. Cetin, and J. Petr   ek, “Optical response of plasmonic nanohole arrays: comparison of square and hexagonal lattices,” *Plasmonics*, vol. 11, no. 3, pp. 851–856, 2016.
- [124] A. Hajiaboli, M. Kahrizi, and V.-V. Truong, “Optical behaviour of thick gold and silver films with periodic circular nanohole arrays,” *J. Phys. D: Appl. Phys.*, vol. 45, no. 48, p. 485105, Dec. 2012, doi: 10.1088/0022-3727/45/48/485105.
- [125] A. E. Cetin and S. N. Topkaya, “Photonic crystal and plasmonic nanohole based label-free biodetection,” *Biosensors and Bioelectronics*, vol. 132, pp. 196–202, May 2019, doi: 10.1016/j.bios.2019.02.047.
- [126] H. Liu and P. Lalanne, “Microscopic theory of the extraordinary optical transmission,” *Nature*, vol. 452, no. 7188, pp. 728–731, Apr. 2008, doi: 10.1038/nature06762.
- [127] J. Braun, B. Gompf, G. Kobiela, and M. Dressel, “How Holes Can Obscure the View: Suppressed Transmission through an Ultrathin Metal Film by a Subwavelength Hole Array,” *Phys. Rev. Lett.*, vol. 103, no. 20, p. 203901, Nov. 2009, doi: 10.1103/PhysRevLett.103.203901.
- [128] H. Im et al., “Template-Stripped Smooth Ag Nanohole Arrays with Silica Shells for Surface Plasmon Resonance Biosensing,” *ACS Nano*, vol. 5, no. 8, pp. 6244–6253, Aug. 2011, doi: 10.1021/nn202013v.

-
- [129] J. Homola, "Surface Plasmon Resonance Sensors for Detection of Chemical and Biological Species," *Chem. Rev.*, vol. 108, no. 2, pp. 462–493, Feb. 2008, doi: 10.1021/cr068107d.
- [130] F. Mazzotta, T. W. Johnson, A. B. Dahlin, J. Shaver, S.-H. Oh, and F. Höök, "Influence of the Evanescent Field Decay Length on the Sensitivity of Plasmonic Nanodisks and Nanoholes," *ACS Photonics*, vol. 2, no. 2, pp. 256–262, Feb. 2015, doi: 10.1021/ph500360d.
- [131] P. Zheng, S. K. Cushing, S. Suri, and N. Wu, "Tailoring plasmonic properties of gold nanohole arrays for surface-enhanced Raman scattering," *Phys. Chem. Chem. Phys.*, vol. 17, no. 33, pp. 21211–21219, Aug. 2015, doi: 10.1039/C4CP05291A.
- [132] M.-C. Estevez, M. A. Otte, B. Sepulveda, and L. M. Lechuga, "Trends and challenges of refractometric nanoplasmonic biosensors: A review," *Analytica Chimica Acta*, vol. 806, pp. 55–73, Jan. 2014, doi: 10.1016/j.aca.2013.10.048.
- [133] E. Wijaya et al., "Surface plasmon resonance-based biosensors: From the development of different SPR structures to novel surface functionalization strategies," *Current Opinion in Solid State and Materials Science*, vol. 15, no. 5, pp. 208–224, Oct. 2011, doi: 10.1016/j.cossms.2011.05.001.
- [134] M. Soler, A. Belushkin, A. Cavallini, C. Kebbi-Beghdadi, G. Greub, and H. Altug, "Multiplexed nanoplasmonic biosensor for one-step simultaneous detection of *Chlamydia trachomatis* and *Neisseria gonorrhoeae* in urine," *Biosensors and Bioelectronics*, vol. 94, pp. 560–567, Aug. 2017, doi: 10.1016/j.bios.2017.03.047.
- [135] T. M. Squires, R. J. Messinger, and S. R. Manalis, "Making it stick: convection, reaction and diffusion in surface-based biosensors," *Nat Biotechnol*, vol. 26, no. 4, pp. 417–426, Apr. 2008, doi: 10.1038/nbt1388.
- [136] M. Couture, K. K. Ray, H.-P. Poirier-Richard, A. Crofton, and J.-F. Masson, "96-Well Plasmonic Sensing with Nanohole Arrays," *ACS Sens.*, vol. 1, no. 3, pp. 287–294, Mar. 2016, doi: 10.1021/acssensors.5b00280.
- [137] J. C. Sharpe, J. S. Mitchell, L. Lin, N. Sedoglavich, and R. J. Blaikie, "Gold Nanohole Array Substrates as Immunobiosensors," *Anal. Chem.*, vol. 80, no. 6, pp. 2244–2249, Mar. 2008, doi: 10.1021/ac702555r.
- [138] A. Lesuffleur, H. Im, N. C. Lindquist, and S.-H. Oh, "Periodic nanohole arrays with shape-enhanced plasmon resonance as real-time biosensors," *Appl. Phys. Lett.*, vol. 90, no. 24, p. 243110, Jun. 2007, doi: 10.1063/1.2747668.
- [139] H. Im et al., "Label-free detection and molecular profiling of exosomes with a nanoplasmonic sensor," *Nature biotechnology*, vol. 32, no. 5, pp. 490–495, 2014.

-
- [140] A. A. Yanik et al., “An optofluidic nanoplasmonic biosensor for direct detection of live viruses from biological media,” *Nano letters*, vol. 10, no. 12, pp. 4962–4969, 2010.
- [141] J. A. Jackman et al., “Plasmonic Nanohole Sensor for Capturing Single Virus-Like Particles toward Virucidal Drug Evaluation,” *Small*, vol. 12, no. 9, pp. 1159–1166, 2016.
- [142] M. Soler, A. Belushkin, A. Cavallini, C. Kebbi-Beghdadi, G. Greub, and H. Altug, “Multiplexed nanoplasmonic biosensor for one-step simultaneous detection of *Chlamydia trachomatis* and *Neisseria gonorrhoeae* in urine,” *Biosensors and Bioelectronics*, vol. 94, pp. 560–567, 2017.
- [143] X. Li, M. Soler, C. I. Özdemir, A. Belushkin, F. Yesilkoy, and H. Altug, “Plasmonic nanohole array biosensor for label-free and real-time analysis of live cell secretion,” *Lab on a Chip*, 2017.
- [144] N. C. Lindquist, A. Lesuffleur, H. Im, and S.-H. Oh, “Sub-micron resolution surface plasmon resonance imaging enabled by nanohole arrays with surrounding Bragg mirrors for enhanced sensitivity and isolation,” *Lab on a Chip*, vol. 9, no. 3, pp. 382–387, 2009, doi: 10.1039/B816735D.
- [145] A. F. Coskun, A. E. Cetin, B. C. Galarreta, D. A. Alvarez, H. Altug, and A. Ozcan, “Lensfree optofluidic plasmonic sensor for real-time and label-free monitoring of molecular binding events over a wide field-of-view,” *Scientific Reports*, vol. 4, p. 6789, Oct. 2014, doi: 10.1038/srep06789.
- [146] A. E. Cetin et al., “Handheld high-throughput plasmonic biosensor using computational on-chip imaging,” *Light: Science & Applications*, vol. 3, no. 1, p. e122, 2014.
- [147] Z. S. Ballard, D. Shir, A. Bhardwaj, S. Bazargan, S. Sathianathan, and A. Ozcan, “Computational Sensing Using Low-Cost and Mobile Plasmonic Readers Designed by Machine Learning,” *ACS nano*, vol. 11, no. 2, pp. 2266–2274, 2017.
- [148] A. De Leebeeck, L. K. S. Kumar, V. de Lange, D. Sinton, R. Gordon, and A. G. Brolo, “On-Chip Surface-Based Detection with Nanohole Arrays,” *Anal. Chem.*, vol. 79, no. 11, pp. 4094–4100, Jun. 2007, doi: 10.1021/ac070001a.
- [149] X. Fan, I. M. White, S. I. Shopova, H. Zhu, J. D. Suter, and Y. Sun, “Sensitive optical biosensors for unlabeled targets: A review,” *analytica chimica acta*, vol. 620, no. 1, pp. 8–26, 2008.
- [150] J. N. Anker, W. P. Hall, O. Lyandres, N. C. Shah, J. Zhao, and R. P. Van Duyne, “Biosensing with plasmonic nanosensors,” in *Nanoscience And Technology: A Collection of Reviews from Nature Journals*, World Scientific, 2010, pp. 308–319.

-
- [151] S. Zeng, D. Baillargeat, H.-P. Ho, and K.-T. Yong, "Nanomaterials enhanced surface plasmon resonance for biological and chemical sensing applications," *Chemical Society Reviews*, vol. 43, no. 10, pp. 3426–3452, 2014.
- [152] G. A. Lopez, M.-C. Estevez, M. Soler, and L. M. Lechuga, "Recent advances in nanoplasmonic biosensors: Applications and lab-on-a-chip integration," *Nanophotonics*, vol. 6, no. 1, pp. 123–136, 2017.
- [153] E. Di Fabrizio et al., "Roadmap on biosensing and photonics with advanced nano-optical methods," *Journal of Optics*, vol. 18, no. 6, p. 063003, 2016.
- [154] V. R. Dantham, S. Holler, V. Kolchenko, Z. Wan, and S. Arnold, "Taking whispering gallery-mode single virus detection and sizing to the limit," *Applied Physics Letters*, vol. 101, no. 4, p. 043704, 2012.
- [155] P. M. Kosaka et al., "Detection of cancer biomarkers in serum using a hybrid mechanical and optoplasmonic nanosensor.," *Nature nanotechnology*, vol. 9, no. 12, 2014.
- [156] D. M. Rissin et al., "Single-molecule enzyme-linked immunosorbent assay detects serum proteins at subfemtomolar concentrations," *Nature biotechnology*, vol. 28, no. 6, pp. 595–599, 2010.
- [157] R. M. Dickson, A. B. Cubitt, R. Y. Tsien, and W. E. Moerner, "On/off blinking and switching behaviour of single molecules of green fluorescent protein," *Nature*, vol. 388, no. 6640, pp. 355–358, 1997.
- [158] A. Jain et al., "Probing cellular protein complexes using single-molecule pull-down," *Nature*, vol. 473, no. 7348, pp. 484–488, 2011.
- [159] S. I. Bozhevolnyi, V. S. Volkov, E. Devaux, J.-Y. Laluet, and T. W. Ebbesen, "Channel plasmon subwavelength waveguide components including interferometers and ring resonators," *Nature*, vol. 440, no. 7083, pp. 508–511, 2006.
- [160] J. Su, A. F. Goldberg, and B. M. Stoltz, "Label-free detection of single nanoparticles and biological molecules using microtoroid optical resonators," *Light: Science & Applications*, vol. 5, no. 1, p. e16001, 2016.
- [161] M. D. Baaske, M. R. Foreman, and F. Vollmer, "Single-molecule nucleic acid interactions monitored on a label-free microcavity biosensor platform," *Nature nanotechnology*, vol. 9, no. 11, pp. 933–939, 2014.
- [162] D. R. Walt, *Optical methods for single molecule detection and analysis*. ACS Publications, 2012.

-
- [163] H. Raether, "Surface plasmons on smooth surfaces," in *Surface plasmons on smooth and rough surfaces and on gratings*, Springer, 1988, pp. 4–39.
- [164] Y. Shen et al., "Plasmonic gold mushroom arrays with refractive index sensing figures of merit approaching the theoretical limit," *Nature communications*, vol. 4, p. 2381, 2013.
- [165] P. Zijlstra, P. M. Paulo, and M. Orrit, "Optical detection of single non-absorbing molecules using the surface plasmon resonance of a gold nanorod," *Nature nanotechnology*, vol. 7, no. 6, pp. 379–382, 2012.
- [166] N. C. Lindquist, P. Nagpal, K. M. McPeak, D. J. Norris, and S.-H. Oh, "Engineering metallic nanostructures for plasmonics and nanophotonics," *Reports on Progress in Physics*, vol. 75, no. 3, p. 036501, 2012.
- [167] A. V. Kabashin et al., "Plasmonic nanorod metamaterials for biosensing," *Nature materials*, vol. 8, no. 11, pp. 867–871, 2009.
- [168] J. Homola, "Surface plasmon resonance sensors for detection of chemical and biological species," *Chemical reviews*, vol. 108, no. 2, pp. 462–493, 2008.
- [169] F. Mazzotta, T. W. Johnson, A. B. Dahlin, J. Shaver, S.-H. Oh, and F. Höök, "Influence of the evanescent field decay length on the sensitivity of plasmonic nanodisks and nanoholes," *Acs Photonics*, vol. 2, no. 2, pp. 256–262, 2015.
- [170] S. Unser, I. Bruzas, J. He, and L. Sagle, "Localized surface plasmon resonance biosensing: current challenges and approaches," *Sensors*, vol. 15, no. 7, pp. 15684–15716, 2015.
- [171] M. Najiminaini, F. Vasefi, B. Kaminska, and J. J. Carson, "Nanohole-array-based device for 2D snapshot multispectral imaging," *Scientific reports*, vol. 3, 2013.
- [172] T. W. Ebbesen, H. J. Lezec, H. F. Ghaemi, T. Thio, and P. A. Wolff, "Extraordinary optical transmission through sub-wavelength hole arrays," *Nature*, vol. 391, no. 6668, pp. 667–669, 1998.
- [173] M. Couture, K. K. Ray, H.-P. Poirier-Richard, A. Crofton, and J.-F. Masson, "96-Well Plasmonic Sensing with Nanohole Arrays," *ACS Sensors*, vol. 1, no. 3, pp. 287–294, Mar. 2016, doi: 10.1021/acssensors.5b00280.
- [174] J. C. Sharpe, J. S. Mitchell, L. Lin, N. Sedoglavich, and R. J. Blaikie, "Gold nanohole array substrates as immunobiosensors," *Analytical Chemistry*, vol. 80, no. 6, pp. 2244–2249, 2008.
- [175] S. Black, I. Kushner, and D. Samols, "C-reactive protein," *Journal of Biological Chemistry*, vol. 279, no. 47, pp. 48487–48490, 2004.

-
- [176] A. D. Pradhan, J. E. Manson, N. Rifai, J. E. Buring, and P. M. Ridker, "C-reactive protein, interleukin 6, and risk of developing type 2 diabetes mellitus," *Jama*, vol. 286, no. 3, pp. 327–334, 2001.
- [177] L. Simon, F. Gauvin, D. K. Amre, P. Saint-Louis, and J. Lacroix, "Serum procalcitonin and C-reactive protein levels as markers of bacterial infection: a systematic review and meta-analysis," *Clinical infectious diseases*, vol. 39, no. 2, pp. 206–217, 2004.
- [178] P. M. Ridker et al., "Rosuvastatin to prevent vascular events in men and women with elevated C-reactive protein," *New England Journal of Medicine*, vol. 359, no. 21, p. 2195, 2008.
- [179] P. M. Ridker et al., "C-reactive protein levels and outcomes after statin therapy," *New England Journal of Medicine*, vol. 352, no. 1, pp. 20–28, 2005.
- [180] T. B. Harris et al., "Associations of elevated interleukin-6 and C-reactive protein levels with mortality in the elderly," *The American journal of medicine*, vol. 106, no. 5, pp. 506–512, 1999.
- [181] R. Niu et al., "iTRAQ-Based Proteomics Reveals Novel Biomarkers for Idiopathic Pulmonary Fibrosis," *PloS one*, vol. 12, no. 1, p. e0170741, 2017.
- [182] F. Yesilkoy et al., "Phase-sensitive plasmonic biosensor using a portable and large field of view interferometric microarray imager," *Light: Science & Applications*, 2018, doi: doi: 10.1038.
- [183] R. W. Wood, "On a remarkable case of uneven distribution of light in a diffraction grating spectrum (from Philosophical Magazine 1902)," *SPIE MILESTONE SERIES MS*, vol. 83, pp. 287–287, 1993.
- [184] A. G. Brolo, R. Gordon, B. Leathem, and K. L. Kavanagh, "Surface plasmon sensor based on the enhanced light transmission through arrays of nanoholes in gold films," *Langmuir*, vol. 20, no. 12, pp. 4813–4815, 2004.
- [185] R. P. Dellinger et al., "Surviving Sepsis Campaign: international guidelines for management of severe sepsis and septic shock, 2012," *Intensive care medicine*, vol. 39, no. 2, pp. 165–228, 2013.
- [186] A. E. Cetin, D. Etezadi, B. C. Galarreta, M. P. Busson, Y. Eksioglu, and H. Altug, "Plasmonic nanohole arrays on a robust hybrid substrate for highly sensitive label-free biosensing," *ACS Photonics*, vol. 2, no. 8, pp. 1167–1174, 2015.
- [187] M. Singer et al., "The Third International Consensus Definitions for Sepsis and Septic Shock (Sepsis-3)," *JAMA*, vol. 315, no. 8, pp. 801–810, Feb. 2016, doi: 10.1001/jama.2016.0287.

-
- [188] C. Fleischmann et al., “Assessment of Global Incidence and Mortality of Hospital-treated Sepsis. Current Estimates and Limitations,” *Am J Respir Crit Care Med*, vol. 193, no. 3, pp. 259–272, Sep. 2015, doi: 10.1164/rccm.201504-0781OC.
- [189] C. Llor and L. Bjerrum, “Antimicrobial resistance: risk associated with antibiotic overuse and initiatives to reduce the problem,” *Therapeutic Advances in Drug Safety*, vol. 5, no. 6, pp. 229–241, Dec. 2014, doi: 10.1177/2042098614554919.
- [190] C. J. Paoli, M. A. Reynolds, M. Sinha, M. Gitlin, and E. Crouser, “Epidemiology and costs of sepsis in the United States—An analysis based on timing of diagnosis and severity Level,” *Critical care medicine*, vol. 46, no. 12, p. 1889, 2018.
- [191] A. Kumar et al., “Duration of hypotension before initiation of effective antimicrobial therapy is the critical determinant of survival in human septic shock*,” *Critical Care Medicine*, vol. 34, no. 6, p. 1589, Jun. 2006, doi: 10.1097/01.CCM.0000217961.75225.E9.
- [192] C. W. Seymour et al., “Time to Treatment and Mortality during Mandated Emergency Care for Sepsis,” *N Engl J Med*, vol. 376, no. 23, pp. 2235–2244, Jun. 2017, doi: 10.1056/NEJMoal703058.
- [193] R. Emanuel et al., “Early Goal-Directed Therapy in the Treatment of Severe Sepsis and Septic Shock,” *The New England Journal of Medicine*, p. 10, 2001.
- [194] J. A. Russell, “Management of Sepsis,” *The New England Journal of Medicine*, p. 15, 2006.
- [195] B. Reddy et al., “Point-of-care sensors for the management of sepsis,” *Nat Biomed Eng*, vol. 2, no. 9, pp. 640–648, Sep. 2018, doi: 10.1038/s41551-018-0288-9.
- [196] R. Ferrer et al., “Empiric Antibiotic Treatment Reduces Mortality in Severe Sepsis and Septic Shock From the First Hour: Results From a Guideline-Based Performance Improvement Program*,” *Critical Care Medicine*, vol. 42, no. 8, p. 1749, Aug. 2014, doi: 10.1097/CCM.0000000000000330.
- [197] M. M. Levy, L. E. Evans, and A. Rhodes, “The Surviving Sepsis Campaign Bundle: 2018 update,” *Intensive Care Med*, vol. 44, no. 6, pp. 925–928, Jun. 2018, doi: 10.1007/s00134-018-5085-0.
- [198] H. H. Liu, M. W. Zhang, J. B. Guo, J. Li, and L. Su, “Procalcitonin and C-reactive protein in early diagnosis of sepsis caused by either Gram-negative or Gram-positive bacteria,” *Ir J Med Sci*, vol. 186, no. 1, pp. 207–212, Feb. 2017, doi: 10.1007/s11845-016-1457-z.
- [199] C. Pierrakos and J.-L. Vincent, “Sepsis biomarkers: a review,” *Crit Care*, vol. 14, no. 1, p. R15, 2010, doi: 10.1186/cc8872.

-
- [200] L. Magrini et al., "Procalcitonin variations after Emergency Department admission are highly predictive of hospital mortality in patients with acute infectious diseases," p. 10.
- [201] K. L. Becker, R. Snider, and E. S. Nylen, "Procalcitonin in sepsis and systemic inflammation: a harmful biomarker and a therapeutic target," *Br. J. Pharmacol.*, vol. 159, no. 2, pp. 253–264, Jan. 2010, doi: 10.1111/j.1476-5381.2009.00433.x.
- [202] M. M. Shaikh, L. E. Hermans, and J. M. van Laar, "Is serum procalcitonin measurement a useful addition to a rheumatologist's repertoire? A review of its diagnostic role in systemic inflammatory diseases and joint infections," *Rheumatology*, vol. 54, no. 2, pp. 231–240, Feb. 2015, doi: 10.1093/rheumatology/keu416.
- [203] L. Chen et al., "Procalcitonin levels correlates with the pathogeny and severity of community acquired pneumonia: a meta-analysis," *Int J Clin Exp Med*, vol. 9, no. 7, pp. 13763–13772, 2016.
- [204] C. I. Michaelidis, R. K. Zimmerman, M. P. Nowalk, M. J. Fine, and K. J. Smith, "Cost-Effectiveness of Procalcitonin-Guided Antibiotic Therapy for Outpatient Management of Acute Respiratory Tract Infections in Adults," *J GEN INTERN MED*, vol. 29, no. 4, pp. 579–586, Apr. 2014, doi: 10.1007/s11606-013-2679-7.
- [205] G. Sener, E. Ozgur, A. Y. Rad, L. Uzun, R. Say, and A. Denizli, "Rapid real-time detection of procalcitonin using a microcontact imprinted surface plasmon resonance biosensor," *Analyst*, vol. 138, no. 21, pp. 6422–6428, Nov. 2013, doi: 10.1039/c3an00958k.
- [206] A. H. Nguyen, Y. Shin, and S. J. Sim, "Development of SERS substrate using phage-based magnetic template for triplex assay in sepsis diagnosis," *Biosensors and Bioelectronics*, vol. 85, pp. 522–528, Nov. 2016, doi: 10.1016/j.bios.2016.05.043.
- [207] D. Rascher et al., "Total internal reflection (TIRF)-based quantification of procalcitonin for sepsis diagnosis – A point-of-care testing application," *Biosensors and Bioelectronics*, vol. 59, pp. 251–258, Sep. 2014, doi: 10.1016/j.bios.2014.03.052.
- [208] S. Kumar, S. Tripathy, A. Jyoti, and S. G. Singh, "Recent advances in biosensors for diagnosis and detection of sepsis: A comprehensive review," *Biosensors and Bioelectronics*, vol. 124–125, pp. 205–215, Jan. 2019, doi: 10.1016/j.bios.2018.10.034.
- [209] F. Baldini et al., "A new procalcitonin optical immunosensor for POCT applications," *Anal Bioanal Chem*, vol. 393, no. 4, pp. 1183–1190, Feb. 2009, doi: 10.1007/s00216-008-2547-1.
- [210] U. Hassan et al., "A point-of-care microfluidic biochip for quantification of CD64 expression from whole blood for sepsis stratification," *Nat Commun*, vol. 8, no. 1, p. 15949, Aug. 2017, doi: 10.1038/ncomms15949.

-
- [211] Y. Zhou, Y. Zhang, A. Johnson, A. Venable, J. Griswold, and D. Pappas, "Detection of culture-negative sepsis in clinical blood samples using a microfluidic assay for combined CD64 and CD69 cell capture," *Analytica Chimica Acta*, vol. 1062, pp. 110–117, Jul. 2019, doi: 10.1016/j.aca.2019.02.039.
- [212] J. Min et al., "Integrated Biosensor for Rapid and Point-of-Care Sepsis Diagnosis," *ACS Nano*, vol. 12, no. 4, pp. 3378–3384, Apr. 2018, doi: 10.1021/acsnano.7b08965.
- [213] A. Belushkin, F. Yesilkoy, and H. Altug, "Nanoparticle-Enhanced Plasmonic Biosensor for Digital Biomarker Detection in a Microarray," *ACS Nano*, vol. 12, no. 5, pp. 4453–4461, May 2018, doi: 10.1021/acsnano.8b00519.
- [214] L. Guo, J. A. Jackman, H.-H. Yang, P. Chen, N.-J. Cho, and D.-H. Kim, "Strategies for enhancing the sensitivity of plasmonic nanosensors," *Nano Today*, vol. 10, no. 2, pp. 213–239, Apr. 2015, doi: 10.1016/j.nantod.2015.02.007.
- [215] H. Guner et al., "A smartphone based surface plasmon resonance imaging (SPRi) platform for on-site biodetection," *Sensors and Actuators B: Chemical*, vol. 239, pp. 571–577, Feb. 2017, doi: 10.1016/j.snb.2016.08.061.
- [216] T. Siegfried, Y. Ekinici, O. J. F. Martin, and H. Sigg, "Engineering metal adhesion layers that do not deteriorate plasmon resonances," *ACS Nano*, vol. 7, no. 3, pp. 2751–2757, Mar. 2013, doi: 10.1021/nn4002006.
- [217] A. M. Leclair, S. S. G. Ferguson, and F. Lagugné-Labarhet, "Surface patterning using plasma-deposited fluorocarbon thin films for single-cell positioning and neural circuit arrangement," *Biomaterials*, vol. 32, no. 5, pp. 1351–1360, Feb. 2011, doi: 10.1016/j.biomaterials.2010.10.051.
- [218] M. Meisner, K. Tschaikowsky, T. Palmaers, and J. Schmidt, "Comparison of procalcitonin (PCT) and C-reactive protein (CRP) plasma concentrations at different SOFA scores during the course of sepsis and MODS," *Critical Care*, vol. 3, no. 1, p. 45, Mar. 1999, doi: 10.1186/cc306.
- [219] I. A. Meynaar, W. Droog, M. Batstra, R. Vreede, and P. Herbrink, "In Critically Ill Patients, Serum Procalcitonin Is More Useful in Differentiating between Sepsis and SIRS than CRP, IL-6, or LBP," *Critical Care Research and Practice*, vol. 2011, pp. 1–6, 2011, doi: 10.1155/2011/594645.
- [220] K. Hajian-Tilaki, "Receiver Operating Characteristic (ROC) Curve Analysis for Medical Diagnostic Test Evaluation," *Caspian J Intern Med*, vol. 4, no. 2, pp. 627–635, 2013.
- [221] C. Jung et al., "Massively Parallel Biophysical Analysis of CRISPR-Cas Complexes on Next Generation Sequencing Chips," *Cell*, vol. 170, no. 1, pp. 35–47.e13, Jun. 2017, doi: 10.1016/j.cell.2017.05.044.

-
- [222] Q. Zou, W. Wen, and X. Zhang, "Presepsin as a novel sepsis biomarker," *World J Emerg Med*, vol. 5, no. 1, pp. 16–19, 2014, doi: 10.5847/wjem.j.issn.1920-8642.2014.01.002.
- [223] M. J. Llewelyn et al., "Sepsis biomarkers in unselected patients on admission to intensive or high-dependency care," *Crit Care*, vol. 17, no. 2, p. R60, 2013, doi: 10.1186/cc12588.
- [224] T. Gervais and K. F. Jensen, "Mass transport and surface reactions in microfluidic systems," *Chemical Engineering Science*, vol. 61, no. 4, pp. 1102–1121, Feb. 2006, doi: 10.1016/j.ces.2005.06.024.
- [225] N. Scott Lynn, H. Šípová, P. Adam, and J. Homola, "Enhancement of affinity-based biosensors: effect of sensing chamber geometry on sensitivity," *Lab on a Chip*, vol. 13, no. 7, pp. 1413–1421, 2013, doi: 10.1039/C2LC41184A.
- [226] A. B. D. Brown, C. G. Smith, and A. R. Rennie, "Pumping of water with ac electric fields applied to asymmetric pairs of microelectrodes," *Physical review E*, vol. 63, no. 1, p. 016305, 2000.
- [227] M. J. A. Shiddiky, R. Vaidyanathan, S. Rauf, Z. Tay, and M. Trau, "Molecular Nanoshearing: An Innovative Approach to Shear off Molecules with AC-Induced Nanoscopic Fluid Flow," *Sci Rep*, vol. 4, no. 1, pp. 1–7, Jan. 2014, doi: 10.1038/srep03716.
- [228] S. C.-H. Tsao et al., "Capture and On-chip analysis of Melanoma Cells Using Tunable Surface Shear forces," *Scientific Reports*, vol. 6, no. 1, Art. no. 1, Jan. 2016, doi: 10.1038/srep19709.
- [229] Y. Song et al., "AC Electroosmosis-Enhanced Nanoplasmafluidic Detection of Ultralow-Concentration Cytokine," *Nano Lett.*, vol. 17, no. 4, pp. 2374–2380, Apr. 2017, doi: 10.1021/acs.nanolett.6b05313.

Curriculum Vitae

Alexander Belushkin

+41 79 107 03 93

Av. de Florimont 22, 1006 Lausanne

alexander.belushkin@epfl.ch

EPFL STI IBI-STI BIOS BM 4130 Station 17 CH-1015 Lausanne

<https://www.linkedin.com/in/alexander-belushkin-99b55080/>

Langages: English (Fluent), Russian (Native), French (basic, B1) Russian

Academic

PhD Microsystems & Bioengineering

Bionanophotonic Systems Laboratory, EPFL

Sept 2015 - Aug 2020 expected graduation

Filed patent "Plasmonic biosensor"

EPFL Technology Transfer Office

Mar 2019 Lausanne, Switzerland

Research Intern

Russian Academy of Sciences

2011 - 2013 Moscow, Russia

- Published an article in a peer-reviewed journal at age 20
- Performed largest-to-date data analysis of structural context of proteolysis using machine-learning metrics

Education

M.S. Bioengineering

Ecole Polytechnique Federale de Lausanne

Sept 2013 - July 2015 GPA **5.67/6.00**

B.S. equivalent Bioengineering & Bioinformatics

Moscow State University

Sept 2010 - June 2013 GPA **4.97/5.00**

Selected publications

- A. Belushkin, et al. "Rapid and Digital Detection of Inflammatory Biomarkers Enabled by a Novel Portable Nanoplasmonic Imager." Small (2019)
- A. Belushkin, F. Yesilköy, and H. Altug. "Nanoparticle Enhanced Plasmonic Biosensor for Digital Biomarker Detection in a Microarray." ACS nano (2018)
- A. Belushkin, et al. "Sequence-derived structural features driving proteolytic processing." Proteomics (2013)

Technical skills

Coding, Modeling & Machine Learning

Matlab • Python • R
PI/SQL • CST • Comsol

Laboratory Research

Immunoassays
Optics & Photonics
Cleanroom nanofabrication

Teaching

- Guided team of 11 master students in an international SensUS competition, Business Translation Award, 2019
- Guided two master students' projects, 2019
- Optics laboratories, Master level, 2018
- Biomicroscopy I & II, Master level, 2015, 2017, 2018

Experience

Raised 100% funding for a start-up in 3 seed funds

EPFL Technology Transfer Office

2018 - ongoing Lausanne, Switzerland

Novel nanoplasmonic test to assist sepsis & SIRS diagnosis

- Invented and built a new point-of-care device, and tested in a Barcelona hospital with patient samples

Intern and Master Thesis

Qcloudlab SA: Modular point-of-care diagnostic test

Jan - June 2015 Lausanne, Switzerland

- Developed signal processing, surface chemistry, and microfluidics for plasmonic detection of bacteria

Intern

Merck Serono

July - Oct 2014 Lausanne, Switzerland

Merck Institute for Pharmacometrics

- Developed mixed population pharmacokinetic models for immunotherapy based on 2 novel mAbs
- The models were used in decision-making about clinical development of the immunotherapy

Extracurricular

President of ShARE EPFL

2016 - ongoing

International Consulting Student Think Tank

- Led the team through transition to a new program and grew student participation 200%, boosting retention, 2018-'19
- Learned and used consulting methodologies, prepared a presentation deck and presented a project with international ShARE team to C-suite members of a Fortune 500 manufacturing company, 2018
- Coordinated expansion of ShARE to Russia and creation of new chapter at HSE Moscow, 2019
- Built relationship with start-ups and incubators, managed ShARE teams with a start-up on pneumonia diagnostics, a food-and-drinks app, and a fuel cell start-up, 2017-'19
- Participated in BCG Consulting Club Contest Geneva, 2019
- Took 3rd place at EPFL Business Case Competition, 2019
- Managed fundraising while treasurer, 2016-'17

Hobbies

Playing tennis, graduated from tennis sports school


Mountain skiing on and off pistes

Open Water Diver license PADI

Publications

1. [Belushkin, A.](#), Yesilkoy, F., González-López, J.J., Ruiz-Rodríguez, J.C., Ferrer, R., Fàbrega, A. and Altug, H., 2019. Rapid and Digital Detection of Inflammatory Biomarkers Enabled by a Novel Portable Nanoplasmonic Imager. *Small*, p.1906108.
2. [Belushkin, A.](#), Yesilkoy, F. and Altug, H., 2018. Nanoparticle-enhanced plasmonic biosensor for digital biomarker detection in a microarray. *ACS nano*, 12(5), pp.4453-4461.
3. Yesilkoy, F., Terborg, R.A., Pello, J., [Belushkin, A.A.](#), Jahani, Y., Pruneri, V. and Altug, H., 2018. Phase-sensitive plasmonic biosensor using a portable and large field-of-view interferometric microarray imager. *Light: Science & Applications*, 7(2), p.17152.
4. Dey, P., Fabri-Faja, N., Calvo-Lozano, O., Terborg, R.A., [Belushkin, A.](#), Yesilkoy, F., Fàbrega, A., Ruiz-Rodríguez, J.C., Ferrer, R., González-López, J.J. and Estévez, M.C., 2018. Label-free bacteria quantification in blood plasma by a bioprinted microarray based interferometric point-of-care device. *ACS sensors*, 4(1), pp.52-60.
5. Li, X., Soler, M., Özdemir, C.I., [Belushkin, A.](#), Yesilköy, F. and Altug, H., 2017. Plasmonic nanohole array biosensor for label-free and real-time analysis of live cell secretion. *Lab on a chip*, 17(13), pp.2208-2217.
6. Soler, M., [Belushkin, A.](#), Cavallini, A., Kebbi-Beghdadi, C., Greub, G. and Altug, H., 2017. Multiplexed nanoplasmonic biosensor for one-step simultaneous detection of Chlamydia trachomatis and Neisseria gonorrhoeae in urine. *Biosensors and Bioelectronics*, 94, pp.560-567.
7. [Belushkin, A.A.](#), Vinogradov, D.V., Gelfand, M.S., Osterman, A.L., Cieplak, P. and Kazanov, M.D., 2014. Sequence-derived structural features driving proteolytic processing. *Proteomics*, 14(1), pp.42-50.

Patents

- A. Belushkin, F. Yesilköy, H. Altug Yanik. Patent application "Plasmonic biosensor" (2019) No. PCT/IB2019/052475. Pub. No.: WO/2019/186416. 

Conference proceedings

1. A. Belushkin et. al, 'Nanoplasmonic imaging biosensor for digital detection of disease biomarkers', 5th Healthcare & Life Science & Entrepreneurship workshop 2020, Accepted for Talk
2. A. Belushkin et. al, 'Nanoplasmonic imaging biosensor for digital detection of disease biomarkers', SPIE Photonics West, SPIE BiOS, 2020, Talk
3. A. Belushkin et. al, 'Nanoparticle Enhanced Plasmonic Biosensor for Digital Biomarker Detection in a Microarray', Single-Molecule Sensors and NanoSystems International Conference 2019, Talk
4. A. Belushkin, 'Nanoparticle-Enhanced Plasmonic Biosensor for Digital Biomarker Detection in a Microarray', EDMI Research Day 2018, Talk
5. A. Belushkin et. al 'Real-time hydrodynamically enhanced plasmonic biosensor based on CCD imaging', International Congress on Analytical Nanoscience and Nanotechnology 2017, Poster
6. A. Belushkin et. al 'Enhancing the sensitivity of high-throughput plasmonic biosensors with microfluidics', MicroTAS 2016, 1200-1202, Poster